SEARCH FOR A STANDARD MODEL HIGGS BOSON IN CMS VIA VECTOR BOSON FUSION IN THE $H \to WW \to \ell\nu\ell\nu$ CHANNEL AND OPTIMIZATION OF ENERGY RECONSTRUCTION IN CMS USING TEST BEAM 2006 DATA

A THESIS SUBMITTED TO
THE GRADUATE SCHOOL OF NATURAL AND APPLIED SCIENCES
OF
MIDDLE EAST TECHNICAL UNIVERSITY

BY

EFE YAZGAN

IN PARTIAL FULFILLMENT OF THE REQUIREMENTS

FOR

THE DEGREE OF DOCTOR OF PHILOSOPHY

IN

PHYSICS

JUNE 2007

Approval of the Graduate School of Natural and Applied Sciences.

Prof. Dr. Canan Özgen
Director

I certify that this thesis satisfies all the requirements as a thesis for the degree of Doctor of Philosophy.

Prof. Dr. Sinan Bilikmen
Head of Department

This is to certify that we have read this thesis and that in our opinion it is fully adequate, in scope and quality, as a thesis for the degree of Doctor of Philosophy.

Prof. Dr. Mehmet T. Zeyrek
Supervisor

Examining Committee Members

Prof. Dr. Nural Akchurin (Texas Tech Uni.,PHYS) _____

Prof. Dr. Mehmet T. Zeyrek (METU,PHYS) _____

Prof. Dr. Ali Ulvi Yılmazer (Ankara Uni.,PHYS) _____

Assoc. Prof. Ali Murat Güler (METU,PHYS) _____

Assoc. Prof. Altuğ Özpineci (METU,PHYS) _____

"I hereby declare that all information in this document has been obtained and presented in accordance with academic rules and ethical conduct. I also declare that, as required by these rules and conduct, I have fully cited and referenced all material and results that are not original to this work."

Name Surname: Efe Yazgan

Signature:

ABSTRACT

SEARCH FOR A STANDARD MODEL HIGGS BOSON IN CMS VIA VECTOR BOSON FUSION IN THE $H \rightarrow WW \rightarrow \ell\nu\ell\nu$ CHANNEL AND OPTIMIZATION OF ENERGY RECONSTRUCTION IN CMS USING TEST BEAM 2006 DATA

YAZGAN, EFE

Ph.D., Department of Physics

Supervisor: Prof. Dr. Mehmet T. Zeyrek

June 2007, 126 pages.

One of the goals of the LHC is to test the existence of the Higgs boson. This thesis presents a study of the potential to discover the Standard Model Higgs boson in the vector boson fusion (VBF) channel for the Higgs mass range 120-200 GeV/c^2. The decay of Higgs bosons into the WW^* final state with both W-bosons decaying leptonically is considered. The main backgrounds are $t\bar{t}+j$ and W^+W^-jj. This study, based on a full simulation of the CMS detector at the LHC, shows that a 5σ discovery can be done with an integrated luminosity of $12-72$ fb^{-1} for $130-200$ GeV/c^2 Higgs bosons. Due to the uncertainties in the backgrounds, it is important to measure the backgrounds from data. This study shows that the major background can be measured directly to 7% with 30 fb^{-1}. After discovering the Higgs boson, it will be crucial to probe its physical properties. A method to measure the Higgs boson mass using transverse mass template distributions is investigated in the VBF channel.

The performance of the combined CMS electromagnetic and hadronic calorimeters (EB+HB) was measured at the H2 test beam at the CERN SPS during 2006 with various particles in a large momentum range, 1-350 GeV/c. Another major contribution of this thesis is developing the method to optimize the energy reconstruction for the combined EB+HB system with which the corrected responses become 100% with 6% fluctuation and the stochastic resolution is improved from 111% to 94%.

Keywords: Higgs Boson, Vector Boson Fusion, CMS, HCAL, Simulation, Test Beam, Energy Reconstruction

ÖZ

CMS'TE VEKTÖR BOZON FÜZYONU İLE OLUŞAN STANDART MODEL HIGGS BOZONUNU $H \to WW \to \ell\nu\ell\nu$ KANALINDA ARAYIŞ VE 2006 TEST HÜZMESİ VERİSİ İLE CMS'TE ENERJİ KURULUMUNUN OPTİMİZASYONU

YAZGAN, EFE

Doktora , Fizik Bölümü

Tez Yöneticisi: Prof. Dr. Mehmet T. Zeyrek

Haziran 2007, 126 sayfa.

LHC'nin amaçlarından biri Higgs bozonunun varlığını sınamaktır. Bu tez Standart Model Higgs bozonunun vektör bozon kanalında (VBF) keşfedilme olasılığını 120-200 GeV/c^2 Higgs kütleleri icin sunar. Higgs bozonunun WW^* çiftine ve iki W-bozonunun da leptonik olarak bozunması durumu göz önüne alınmıştır. Bu kanal için başlıca arka planlar $t\bar{t}+j$ and W^+W^-jj'dır. CMS detektörünün tam simulasyonuna dayanan bu çalışma Higgs bozonunun 130-200 GeV/c^2 kütle aralığında 5σ güvenilirliğinde keşfinin 12-72 fb^{-1} parlaklığında yapılabileceği gösterilmiştir. Arka plandaki belirsizlikler, arka planın doğrudan deneyde ölçülmesini önemli kılmaktadır. Bu çalışma, arka planın %7 hassaslığıyla 30 fb^{-1}'la doğrudan ölçülebileceğini göstermiştir. Higgs bozonunun keşfinden sonra, Higgs bozonunun fiziksel özelliklerinin incelenmesi çok önemli olacaktır. Higgs bozon kütlesinin enine kütle kalıpları kullanılarak deney verileriyle öngörülmesi için bir yöntem VBF kanalı için öne sürülmüştür.

2006 yılında EB+HB detektör sisteminin performansı H2'de CERN SPS'de geniş bir momentum aralığında 1-350 GeV/c test hüzmeleriyle ölçülmüştür. Bu tezin diğer bir önemli katkısı, EB+HB birleşik sisteminin enerji kurulumu optimizasyon yönteminin geliştirilmesi olmuştur. Sunulan yöntemle enerji tepkileri %100'e %6 dalgalanmayla düzeltilmiş ve stokastik çözünürlük %111'den %94'e iyileştirilmiştir.

Anahtar Sözcükler: Higgs Bozonu, Vektör Bozon Füzyonu, CMS, HCAL, Simulasyon, Test Hüzmesi, Enerji Kurulumu

To Yasemin; to my father, mother and brother.

ACKNOWLEDGMENTS

First of all, I am most grateful to my supervisor Mehmet T. Zeyrek who has become more of a mentor and friend than a professor with the guidance, motivation and encouragement he provided me.

I would like to thank all the LHC Physics Center staff at Fermilab for their support. I am grateful to Muzaffer Atac and Jim Freeman without whom I would not have had the chance to work at the fruitful research atmosphere at Fermilab.

I am indebted to Shuichi Kunori who has been my *sensei*, teaching and guiding me through every step of the research leading to my thesis. His expertise, understanding and patience added considerably to my research experience at Fermilab.

This work would not have been possible without the assistance of my CMS colleagues. I would like to thank Dan Green for his insights on the energy reconstruction and qqH. Many thanks to Jordan Damgov without whom this study would have been much more difficult to do. I would like to thank Sasha Nikitenko for his valuable help and useful comments,and Yuri Gerstein for his assistance in electron identification and selection. I also acknowledge Marek Zielinsky, Nick Hadley, Philippe Bloch, Albert DeRoeck Micheal Schmidt, Mayda Velasco and Walter Giele for all their help. I am grateful to Sung-Won Lee for his encouragement during test beam analyses and the fruitful test beam meetings. I am also thankful to Weimin Wu, Rick Vidal, Stefan Piperov, Jordan Damgov and Taylan Yetkin for their friendship, help and cheerful discussions on physics and

everything else. I would like to thank Patrick Gartrund for his technical support.

Special thanks to Rick Vidal for his valuable comments and suggestions on the manuscript.

I would like to thank all the members of the METU High Energy Physics Group, especially Sezen Sekmen for her constant friendship, encouragement and humor.

I am grateful to the High Energy Physics Group at Texas Tech, namely, Nural Akchurin, Richard Wigmans, Sung-Won Lee, Igor Volobouev, Alan Sill for their valuable comments, criticism and encouragement.

I also would like to thank my friends O. Barış Malcıoğlu and Emre S. Taşcı for all their help and friendship.

I would like to honor the memories of the great physicists and teachers Michail Rekalo and Ordal Demokan who inspired me.

I am indebted to my mother and brother for all their support and encouragement, and to my father who was always happy to see me curious about the Universe. Last but not least, I would like to thank my beloved wife and best friend Yasemin for her love and encouragement.

TABLE OF CONTENTS

ABSTRACT iv

ÖZ vi

DEDICATION viii

ACKNOWLEDGMENTS viii

TABLE OF CONTENTS xi

LIST OF TABLES xiv

LIST OF FIGURES xv

1 INTRODUCTION 1

2 THE STANDARD MODEL HIGGS BOSON 5

2.0.1 Fermion Masses and Couplings 10

2.0.2 Experimental and Theoretical Limits on the Higgs Boson 13

2.0.3 Standard Model Higgs Boson Searches at the LHC 22

2.0.3.1 Higgs Boson Production at the LHC 22

2.0.3.2 Higgs Boson Decays 26

2.0.3.3 Search Strategies for the Higgs Boson at the LHC 27

3 THE EXPERIMENT 33

3.1 Large Hadron Collider (LHC) 33

3.2 The CMS Experiment 40

3.2.1 The CMS Magnet - Superconducting Solenoid 41
3.2.2 Muon System 41
3.2.3 Electromagnetic Calorimeter (ECAL) 47
3.2.4 Hadron Calorimeter (HCAL) 49
3.2.5 The Tracker 53
3.2.6 Triggers 55

4 OPTIMIZATION OF ENERGY RECONSTRUCTION IN CMS USING TEST BEAM 2006 DATA 57
4.1 Introduction 57
4.2 Test Beam Setup, Beam Clean-up and Particle Identification 57
4.3 Energy Reconstruction and Detector Performance 60
4.4 Optimization of Energy Reconstruction 63
4.5 Results 68

5 SEARCH FOR A STANDARD MODEL HIGGS BOSON IN CMS VIA VECTOR BOSON FUSION IN THE $H \rightarrow WW \rightarrow l\nu l\nu$ CHANNEL 73
5.1 Introduction 73
5.2 Event Generation 76
5.3 Detector Simulation and Event Reconstruction 77
5.3.1 Trigger 78
5.3.2 Lepton Reconstruction and Identification . . . 78
5.3.2.1 Muons 79
5.3.2.2 Electrons 80
5.3.3 Jet and Missing E_T Reconstruction and Correction 82
5.4 Event Selection 85
5.4.1 Forward Jet Tagging 85
5.4.2 Central Jet Veto 85
5.4.3 Lepton Kinematics 87

5.4.4 Further Kinematic Requirements 90
5.4.5 Additional Cuts 92
5.5 Results 100
5.5.1 Background Estimation from the Data 112
5.5.2 Sensitivity to the Higgs Mass 115

6 CONCLUSION 118

REFERENCES 120

LIST OF TABLES

2.1 Three families in the Standard Model 12

3.1 Some of the LHC parameters relevant for CMS and ATLAS [40] 36

5.1 Production cross section for the signal(qqH) and the main backgrounds 77

5.2 Summary of accepted cross sections, in fb. A series of assumed Higgs boson masses is shown, as well as the backgrounds for the "low-mass" and "high-mass" cuts. 103

5.3 Significance of an excess as a function of Higgs mass, for three assumed integrated luminosities. The last column shows the minimum luminosity required for a 5σ excess. 103

5.4 Accepted signal (for m_H=120,160 GeV) and major background cross sections in fb for the $H \to WW \to ee\nu\nu$ final state. 106

5.5 Accepted signal (for m_H=120,160 GeV) and major background cross sections in fb for the $H \to WW \to e\mu\nu\nu$ final state. 107

5.6 Accepted signal (for m_H=120,160 GeV) and major background cross sections in fb for the $H \to WW \to \mu\mu\nu\nu$ final state. 108

5.7 Accepted signal (for m_H=120 GeV and for ttj) cross-sections in fb for the $H \to WW \to e\mu\nu\nu$ with looser forward jet tagging, di-jet mass cut, and central jet veto. The production of Higgs is via vector boson fusion. 109

LIST OF FIGURES

2.1 The Higgs potential [5]. 9

2.2 WW scattering with the exchange of a Higgs boson. The perturbative unitarity breaks down if $m_H \geq 1$ TeV. 13

2.3 Higgs boson theoretical mass limits. The light-shaded areas are the forbidden zones. The upper limit is determined from the requirement of consistency of the electroweak theory up to the Λ scale. The lower limit is determined from the condition of absolute vacuum stability. The solid areas show the uncertainties in the bounds [19]. 14

2.4 Solid line shows the observed and the dashed line the expected values for the test statistics parameter -2lnQ. Dark region represents 1σ and the light region represents 2σ around the mean. [35]. 15

2.5 Higgs production for the dominant channels for Tevatron Run II. The center of mass energy is 2 TeV [14]. 17

2.6 Search for the Higgs boson in $H \rightarrow WW* \rightarrow ll'(l, l' = e, \mu)$ decays with 950 pb^{-1} in D0 in Run II [34, 35]. 17

2.7 Tevatron run II preliminary upper limits by CDF and D0 experiments for the SM Higgs boson production. The upper curves represent the experimental limits at the 95% confidence levels and the curves in the lower part are the Standard Model predictions [35, 36]. 18

2.8 $\Delta\chi^2$ determined from a fit to electroweak precision measurements *vs* the Higgs boson mass. Solid line shows the fit. The band around the fit curve shows the uncertainty induced by the higher order corrections. The excluded region is determined from the direct searches at LEP corresponding to 95% CL [31]. 19

2.9 SM Higgs mass as a function of top mass [35]. 21

2.10 m_W *vs* m_t. The SM prediction for different Higgs masses are also shown [35]. 21

2.11 Feynman diagrams for the dominant Higgs production mechanisms at the LHC. 22

2.12 Higgs production for the dominant channels for the LHC where $\sqrt{s} = 14$ TeV [14]. 23

2.13 A typical VBF event with the forward/backward jets and the two leptons in the central region. 25

2.14 Branching ratios for the standard model Higgs boson *vs* mass [12] 27

2.15 The statistical significance for an integrated luminosity of 30 fb^{-1} of Higgs boson reach for CMS (top) and the needed integrated luminosity to achieve a 5σ discovery (bottom) [59]. 31

2.16 The statistical significance for an integrated luminosity of 30 fb^{-1} of Higgs boson reach for ATLAS [39]. 32

3.1 Structure and experiments of the LHC [40]. 35

3.2 Proton-(anti)proton cross sections at Tevatron and LHC as a function of center of mass energy [13]. 39

3.3 Schematic view of CMS. 42

3.4 The CMS Experiment 43

3.5 Layout of the muon system [48]. 45

3.6 Layout of the ECAL detector [51] 48

3.7 Layout of the pixel detector [55]. 53

3.8 Layout of the CMS tracking detectors [56]. 54

3.9 The CMS DAQ system. Taken from ptdr1 [60] 56

4.1 Layout of the testbeam line at H2. 58

4.2 EB,HB and HE on the rotatable table. The white line represents the beam. 59

4.3 Plots of energy in EB vs energy in HB for a) 300, b) 30, c) 9 and d) 2 GeV beam momenta. 61

4.4 EB+HB performance for $\pi^{\pm}, p, \overline{p}$ and $K^{\pm}$ as a function of beam momentum [50]. 62

4.5 π/e vs $log < E_{HB} >$ for HB only. Above 8 GeV the data is parametrized using Wigmans' method with e/h'=1.39 and the data below 8 GeV is parametrized using a logarithmic function. 65

4.6 *π/e vs log $< E_{HB} >$ for HB only. Above 8 GeV the data is parametrized using Wigmans' method with e/h'=1.39 and the data below 8 GeV is parametrized using a logarithmic function. The data is also fitted to a 4^{th} order polynomial.* 65

4.7 Measured $< (\pi/e)_{EB} >$ vs $log(E_{EB})$ with and without the cuts on E_{EB}. The linear fit to these data are also shown. 66

4.8 a) π/e corrected energy of EB+HB combined system. b) π/e corrected response of EB+HB combined system as a function of the EB energy fraction and the fitted cubic function in EB energy fraction. c) and d) are the energy and response corrected with the cubic function in b). 67

4.9 Raw and π/e corrected energy resolution curves determined from sample means and rms values. 70

4.10 Raw and π/e corrected energy resolution curves determined from Gaussian mean and σ. 70

4.11 Raw and π/e corrected responses determined from sample means and rms values. 71

4.12 Raw and π/e corrected responses determined from Gaussian mean and σ. 71

5.1 Feynman diagram for Higgs boson production through Vector Boson Fusion. The Higgs boson decays into W's which further decay into electron/muon-neutrino pairs. 74

5.2 Uncorrected and corrected jet E_T response as a function of generator level jet E_T for four different η regions in 0.2 bins. . . . 83

5.3 $\Delta\eta = |\eta_1 - \eta_2|$ distribution for the forward tag jets which have $E_{T1} > 50$ GeV and $E_{T2} > 30$ GeV for a) qqH, $m_H = 120$ GeV and backgrounds b) $t\bar{t}j$, c) EW W^+W^-jj and d) QCD W^+W^-jj. Note that the EW W^+W^-jj background is basically irreducible. 86

5.4 $\eta_0 = \eta_3 - (\eta_1 + \eta_2)/2$ for the third jet. η of the third jet with respect to the average of the two forward jets. For signal a) qqH, $m_H = 120$ GeV and backgrounds b) $t\bar{t}j$, c) EW W^+W^-jj and d) QCD W^+W^-jj. 88

5.5 Fraction of fake central jets per event as a function of E_T veto threshold. A fake is defined as the probability to find at least one jet(due to pile-up) satisfying the central jet veto conditions, with no "real" jets satisfying the central jet veto condition in that event. 89

5.6 Electron E_T spectra, for the signal process when $m_H = 120$ GeV 89

5.7 Centrality of the leptons, using the quantity η'_ℓ defined in the text for a) qqH, $m_H = 120$ GeV and backgrounds b) $t\bar{t}j$, c) EW W^+W^-jj and d) QCD W^+W^-jj. 91

5.8 Invariant mass distributions for the two forward tag jets, for a) qqH, $m_H = 120$ GeV and backgrounds b) $t\bar{t}j$, c) EW W^+W^-jj and d) QCD W^+W^-jj. 93

5.9 The overall p_T-balance in the event. for a) qqH, $m_H = 120$ GeV and backgrounds b) $t\bar{t}j$, c) EW W^+W^-jj and d) QCD W^+W^-jj. 94

5.10 Di-lepton invariant mass distribution after jet and lepton cuts, for a) qqH, $m_H = 120$ GeV and backgrounds b) $t\bar{t}j$, c) EW W^+W^-jj and d) QCD W^+W^-jj. 95

5.11 The distribution of the difference in azimuthal angle between the two leptons, $\Delta\phi$ after jet and lepton cuts, for a) signal events, qqH, $m_H = 120$ GeV and backgrounds b) $t\bar{t}j$, c) EW W^+W^-jj and d) QCD W^+W^-jj. 96

5.12 The $\Delta\phi$ distribution between the two leptons after jet and lepton cuts for qqH, $m_H = 200$ GeV 97

5.13 The transverse mass of the two W bosons, $M_{T,WW}$, for a) signal events, qqH, $m_H = 120$ GeV and backgrounds b) $t\bar{t}j$, c) EW W^+W^-jj and d) QCD W^+W^-jj. 98

5.14 The transverse mass, $M_{T,WW}$, distributions for signal and background, with Higgs mass = 120, 130, 140, 160, 180 and 200 GeV respectively shown in a),b),c),d),e),f). The Lower plot (light grey) is the signal, the middle plot(dark grey) is the background, and the black histogram is the sum. 99

5.15 The azimuthal angle difference (in radians) between the dilepton momentum as a function of $\not{E}_T$ vs p_T^{Higgs} for qqH with $m_H = 120$ GeV. The lines in the figure correspond to the cuts: $57.29\Delta\phi(ll, \not{E}_T) + 1.5p_T^{Higgs} > 180$ and $12 \times 57.29\Delta\phi(ll,\not{E}_T) + p_T^{Higgs} > 360$. . 100

5.16 a) $\Delta\phi(ll, \not{E}_T)$ vs. $\Delta\phi_{ll}$ and b) the sum of $\Delta\phi_{ll}$ and $\Delta\phi(ll, \not{E}_T)$ for qqH $m_H = 120$ and for ttj bacground c) and d). The lines correspond to $\Delta\phi_{ll} + \Delta\phi(ll,\not{E}_T) = 3$ radians. 101

5.17 Significance of the Higgs signal as a function of Higgs mass for a 30 fb^{-1} integrated luminosity. 104

5.18 Minimum integrated luminosity (fb^{-1}) needed to obtain a 5σ excess over the $t\bar{t}j + W^+W^-jj$ background as a function of the Higgs mass. 105

5.19 $M_{\ell\ell}$ distribution computed with looser cuts and full analysis cuts. 113

5.20 The transverse mass, $M_{T,WW}$ distribution for estimated(dashed) and real(solid) background. 114

5.21 Estimated(dashed) and real(solid) $M_{T,WW}$ distributions for signal events, with Higgs mass of 120,130,140,160,180 and 200 GeV shown in a),b),c),d),e) and f) respectively. 116

5.22 Kolmogorov test function for estimating the Higgs boson mass for Higgs masses of 120,130,140,160,180 and 200 GeV shown in a),b),c),d),e) and f) respectively. 117

CHAPTER 1

INTRODUCTION

I'm astounded by people who want to 'know' the universe when it's hard enough to find your way around Chinatown.

- Woody Allen

The Standard Model (SM) of particle physics is the current best mathematical description of particles and their interactions. Almost all the predictions of the Standard Model were verified to a very high precision. The theory is based on local gauge symmetry group $SU(3)_c \otimes SU(2)_L \otimes U(1)_Y$ and predicts that interactions are mediated by the exchange of vector bosons. There are eight gluons responsible for the strong interactions, and four bosons responsible for the electroweak interaction, namely $W^{\pm}$, Z and the photon. There is an asymmetry between the electroweak bosons - $W^{\pm}$ and Z are massive while the mass of the photon is exactly zero. Unfortunately, an explicit bare term in the Lagrangian of the theory that specifies the mass of the electroweak bosons violates the local gauge invariance. However, adding the Higgs mechanism, which spontaneously breaks the local gauge symmetry to $SU(3)_c \otimes U(1)_{em}$ rescues the theory and allow the electroweak bosons to acquire mass [1, 2, 3, 4]. The idea of the Higgs

mechanism emerged from a relativistic analog of the Landau-Ginzburg (LG) description of superconductivity in which the photon gains an effective mass in a superconductor by the spontaneous breaking of the electromagnetic gauge invariance. Both in the LG description of superconductivity and the Higgs mechanism, below the critical parameter of the theory, the underlying symmetry is "hidden". The Higgs mechanism assumes a scalar doublet field, composed of two complex Higgs fields, with one of the complex components charged and the other neutral, that interacts with initially massless vector fields. In this way, the masses of the vector bosons and the massless photon can easily be accommodated without spoiling the theory: the interaction of the scalar field with the vector fields reduces to the mass of the vector bosons as long as the vacuum expectation value of the scalar field is non-zero. The spontaneous symmetry breaking gives mass not only to the vector bosons but it can give mass to the fermions. Even though explicit mass terms violate the symmetry of the Standard Model, the Yukawa coupling of the Higgs scalar to a pair of fermions are allowed. Fermion masses then are proportional to the vacuum expectation value of the Higgs field. The Yukawa coupling values required to reproduce the observed fermion masses range from 3×10^{-6} for the electron to 1 for the top quark. The Standard Model does not try to explain the values, nor the huge range of these dimensionless couplings.

The Higgs mechanism predicts the existence of one neutral scalar, namely

the Higgs boson with its self couplings. The Higgs boson is the only Standard Model particle that is not yet observed. One of the difficulties for Higgs searches is that the mass of the Higgs boson is not predicted by the Standard Model. In theories beyond the Standard Model, the mechanism of spontaneous symmetry breaking is usually the same as the Standard Model but with more complicated Higgs fields, and a higher number of surviving Higgs bosons, including charged scalar bosons. One of the most important goals of the Large Hadron Collider (LHC), which will start operations soon after the completion of this thesis is to clarify the origin of particle masses. LHC has two major general purpose detectors, namely ATLAS and CMS, and two smaller experiments, one for heavy ion physics (ALICE) and another for b-physics (LHCb).

For the most part of this thesis presents my work within the CMS collaboration over the past two years - namely, a study of the search for a Standard Model Higgs boson via vector boson fusion in the $H \rightarrow WW \rightarrow l\nu l\nu$ channel. A second major part of the thesis is the study of optimization of energy reconstruction in CMS using the Test Beam 2006 data. The thesis is organized as follows: Chapter 2 is an overview of the electroweak theory with special emphasis on the Higgs mechanism and the Higgs boson. Chapter 3 gives a general description of the LHC and CMS, and describes each subdetector of CMS. Chapters 4 and 5 include the main topics and the original contributions of my thesis to CMS. In 2006, from late summer to the end of November, tests of CMS ECAL+HCAL

combined calorimeter system have been made at the H2 beam line at the Super Proton Synchrotron (SPS) at CERN. Chapter 4 describes these tests and presents the studies that optimize the response of the combined EB+HB system. Chapter 5 describes the simulation study for the search for the Higgs boson via vector boson fusion in the $H \rightarrow WW \rightarrow l\nu l\nu$ channel. This channel has good prospects both for the discovery of the Standard Model Higgs boson and the determination of the HWW coupling which is crucial to establishing the origin of electroweak symmetry breaking and the vector boson masses.

CHAPTER 2

THE STANDARD MODEL HIGGS BOSON

With gauge bosons W_μ^i, i=1-3 for the group, SU(2), and B_μ for the group, U(1), the gauge group SU(2)$\otimes$U(1) is the symmetry group of the electroweak theory. Except for the photon, the weak gauge bosons become massive only after Spontaneous Symmetry Breaking (SSB) of the electroweak symmetry from SU(2)$\otimes$U(1) to $U(1)_{em}$. That is, the interactions allowed by SU(2)$\otimes$U(1) are locally gauge invariant. Since mass terms like $m\psi\overline{\psi}$ are not locally gauge invariant under the SU(2)$\otimes$U(1) group, the mass of the W,Z particles should be zero. However, if the vacuum has a non-zero expectation value for some scalar field, the component of the scalar field can be absorbed into the longitudinal part of the vector fields giving them mass. Thus, vector fields are responsible for the dynamics but scalar fields create inertia. Vector fields are an appearance of local symmetry, but the scalar field(s) break the symmetry, and allow the vector fields to have mass.

In QED, the Lagrangian, whose density is invariant under local gauge transformations, U(1), describing the coupling of the photon fields, A^μ, to an electron

field, ψ is given as;

$$\mathcal{L} = \frac{-1}{4} F^{\mu\nu} F_{\mu\nu} + \overline{\psi}(i\not{D} - m_e)\psi \tag{2.1}$$

where $F^{\mu\nu} = \partial^\mu A^\nu - \partial^\nu A^\mu$ and $D_\alpha = \partial_\alpha + ieA^\alpha$ is the covariant derivative. If the gauge field transforms as

$$A_\mu(x) \rightarrow A_{\mu(x)} - \frac{1}{e}\partial_\mu \theta(x) \tag{2.2}$$

then the Lagrangian is independent of the definition of the phase $\psi'(x) = e^{i\theta(x)}\psi(x)$. Therefore Lagrangian is locally gauge invariant, under a U(1) gauge transformation. The gauge coupling constant in QED is the electric charge, e.

The electroweak theory assumes invariance under the group SU(2) $\otimes$ U(1), in which the 3 massless gauge bosons $W^i (i = 1, 2, 3)$ are associated with the gauge group SU(2) and one massless boson, B, is associated with U(1). The piece of the Lagrangian for the 4 gauge bosons is

$$\mathcal{L} = \frac{-1}{4} W^{i\mu\nu} W^i_{\mu\nu} - \frac{1}{4} B^{\mu\nu} B_{\mu\nu} \tag{2.3}$$

where $W^i_{\mu\nu} = \partial_\mu W^i_\nu - \partial_\nu W^i_\mu - g_W \epsilon^{ijk} W^j_\mu W^k_\nu$ (g_W is the SU(2) gauge coupling) and $B_{\mu\nu} = \partial_\mu B_\nu - \partial_\nu B_\mu$. The expression for $W^i_{\mu\nu}$ contains quadratic self interactions for the W^i. This is due to the non-Abelian nature of SU(2).

Coupling of the gauge fields to fermion fields is again described by the covariant derivative but now in a more complicated form:

$$D^\mu = \delta_{ij}\partial^\mu + ig_W (T \cdot W^\mu)_{ij} + iY\delta_{ij} g'_W B^\mu \tag{2.4}$$

where g'_W is the U(1) gauge coupling. Here, Y is the weak hypercharge representing the charge of U(1). SU(2) algebra is represented by the matrices T^i. The Levi-Civita tensor, ϵ^{ijk}, comes from the non-commutation of the isospin operators

$$[T^i, T^j] = i\epsilon^{ijk}T^k. \tag{2.5}$$

If we define $W^{\pm}_{\mu} \equiv (W^{(1)}_{\mu} \mp iW^{(2)}_{\mu})/\sqrt{2}$ and $T^{\pm} \equiv T^{(1)} \pm iT^{(2)}$, then

$$W_{\mu} \cdot T = W^{(1)}_{\mu}T_1 + W^{(2)}_{\mu}T_2 + W^{(3)}_{\mu}T_3 \tag{2.6}$$

$$= \frac{1}{\sqrt{2}}W^{+}_{\mu}T^{+} + \frac{1}{\sqrt{2}}W^{-}_{\mu}T^{-} + W^{3}_{\mu}T_3 \tag{2.7}$$

where $[T^+, T^-] = 2T^3$ and $[T^3, T^{\pm}] = \pm T^{\pm}$. T^+ and T^- are the raising and lowering operators for weak isospin. $T_{\alpha} \equiv \frac{1}{2}\sigma_{\alpha}$, where σ_{α} is the α^{th} component of the Pauli matrices;

$$\sigma_1 = \begin{pmatrix} 0 & 1 \\ 1 & 0 \end{pmatrix}, \sigma_2 = \begin{pmatrix} 0 & -i \\ i & 0 \end{pmatrix}, \sigma_3 = \begin{pmatrix} 1 & 0 \\ 0 & -1 \end{pmatrix}. \tag{2.8}$$

For the SM the simplest choice that can generate masses for the three gauge bosons but keeping the photon massless assumes a complex SU(2) doublet of scalar fields

$$\Phi = \begin{pmatrix} \phi^+ \\ \phi^0 \end{pmatrix} = \begin{pmatrix} \phi_1 + i\phi_2 \\ \phi_3 - i\phi_4 \end{pmatrix} \tag{2.9}$$

The corresponding term in the SM Lagrangian is given by

$$\mathcal{L}_{Higgs} = (D^{\mu}\Phi)^{\dagger}(D_{\mu}\Phi) - V(\Phi^{\dagger}\Phi) \tag{2.10}$$

where D^μ is the covariant derivative given by Eq. (2.4) and $V(\Phi^\dagger\Phi)$ is the so-called Higgs potential,

$$V(\Phi^\dagger\Phi) = -\mu^2\Phi^\dagger\Phi + \lambda(\Phi^\dagger\Phi)^2. \tag{2.11}$$

If λ and $\mu^2 > 0$, the potential has its minimum point not at the origin but at $\Phi^\dagger\Phi = \mu^2/2\lambda$ which is the value that the Higgs field assumes in the vacuum.

This means that the neutral component of the scalar doublet now has a vacuum expectation value, $v = \mu^2/\lambda$,

$$< 0|\Phi|0 >= \begin{pmatrix} 0 \\ \\ v/\sqrt{2} \end{pmatrix}. \tag{2.12}$$

The direction of the minimum in SU(2) space is chosen such that the component for the charged scalar field is 0 which preserves the U(1) symmetry of QED. In this choice, the electric charge is $Q = T^3 + Y$ which leaves the vacuum expectation invariant. The Higgs potential can be displayed graphically, for example, by setting the imaginary parts of the doublet of scalar fields to zero (see Fig. 2.1). In Fig. 2.1, it is seen that the minimum corresponds to a circle on the graph. Considering the excitations around the vacuum state and parametrizing the Higgs field with the three fields and H we obtain

$$\Phi = \begin{pmatrix} \epsilon_1 + i\epsilon_2 \\ \\ \frac{1}{\sqrt{2}}(v + H) - i\epsilon_3 \end{pmatrix} = U^{-1}(\epsilon) \begin{pmatrix} 0 \\ \\ \frac{1}{\sqrt{2}}(v + H) \end{pmatrix} \tag{2.13}$$

where $U^{-1} = e^{i\epsilon_\alpha\sigma^\alpha/v}$. Then making a transformation ($\Phi \rightarrow U(\epsilon)\Phi$) to the

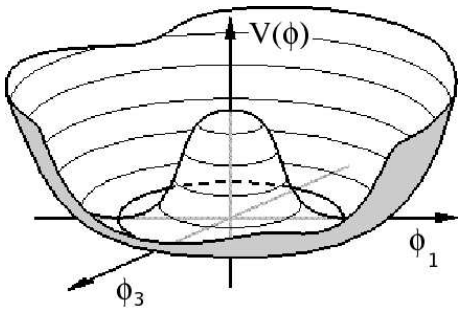

Figure 2.1: The Higgs potential [5].

unitary gauge in which the unphysical degrees of freedom disappear, we obtain

$$\Phi = \frac{1}{\sqrt{2}} \begin{pmatrix} 0 \\ \\ v + H \end{pmatrix} \tag{2.14}$$

Then, expanding the $|D_\mu \Phi|^2$ term of the Higgs Lagrangian,

$$|D_\mu \Phi|^2 = |(\delta_{ij}\partial_\mu - i g_W T_\alpha W_\mu^\alpha + \frac{i}{2}\delta_{ij} g'_W B_\mu)\Phi|^2 \tag{2.15}$$

Inserting the Pauli matrices explicitly we find,

$$|D_\mu \Phi|^2 = \frac{1}{2} \left| \begin{pmatrix} \partial_\mu - \frac{i}{2}(g_W W_\mu^3 + g'_W B_\mu) & \frac{-ig_W}{2}(W_\mu^1 - iW_\mu^2) \\ \\ \frac{ig_W}{2}(W_\mu^1 + iW_\mu^2) & \partial_\mu + \frac{i}{2}(g_W W_\mu^3 - g'_W B_\mu) \end{pmatrix} \begin{pmatrix} 0 \\ \\ v + H \end{pmatrix} \right|^2 \tag{2.16}$$

Taking the square, the $|D_\mu \Phi|^2$ term is

$$|D_\mu \Phi|^2 = \frac{1}{2}(\partial_\mu H)^2 + \frac{g_W^2 (v+H)^2}{8} |W_\mu^{(1)} - iW_\mu^{(2)}|^2 + \frac{(v+H)^2}{8} |g_W W_\mu^{(3)} - g'_W B_\mu|^2. \tag{2.17}$$

Three fields can be defined such that:

$$W^\pm = \frac{1}{\sqrt{2}}(W_\mu^1 \mp i W_\mu^2), \qquad Z_\mu = \frac{g_W W_\mu^3 - g'_W B_\mu}{\sqrt{g_W^2 + g_W'^2}}$$
$$A_\mu = \frac{g_W W_\mu^3 + g'_W B_\mu}{\sqrt{g_W^2 + g_W'^2}} \tag{2.18}$$

Putting these definitions in Eq. (2.17) and looking at the terms quadratic in the gauge bosons $W^{\pm}, Z$ and A, we get

$$(\frac{v^2 g_W^2}{4}) W_\mu^+ W^{-\mu} + \frac{v^2(g_W^2 + g_W'^2)}{8} Z_\mu Z^\mu + 0 \times A_\mu A^\mu$$
$$= m_W^2 W_\mu^+ W^{-\mu} + \frac{1}{2} m_Z^2 Z_\mu Z^\mu + m_A^2 A_\mu A^\mu \tag{2.19}$$

m_W, m_Z and m_A represent the W, the Z and the photon mass respectively. Therefore, spontaneous symmetry breaking allowed the three Goldstone bosons to be "eaten" by or absorbed in the definition of $W^{\pm}$ and Z bosons. The $\mathrm{U}(1)_{em}$ symmetry survives so that the photon is still massless.

To first order the Z and W boson masses are related by

$$m_Z = \frac{m_W}{\cos\theta_W} \tag{2.20}$$

where θ_W is the Weinberg angle defined by

$$\sin^2\theta_W \equiv \frac{g_W^2}{g_W^2 + g_W'^2}. \tag{2.21}$$

The other terms in the Higgs Lagrangian describes the Higgs self-couplings

$$\frac{1}{2}\partial_\mu H \partial^\mu H - \mu^2 H^2 - \lambda v H^3 - \frac{1}{4}\lambda H^4 \tag{2.22}$$

with mass $m_H^2 = 2\mu^2 = 2\lambda v^2$. The vacuum expectation value, $v = \mu/\sqrt{2\lambda}$ is determined by the theory, λ, however remains arbitrary.

2.0.1 Fermion Masses and Couplings

Although existence of fermion masses directly implies that the electroweak symmetry is broken, the electroweak theory does not predict the fermion mass

values. Every fermion needs a Yukawa coupling whose values are as to match the observed masses. After the spontaneous symmetry breaking, the Yukawa couplings represent the mass terms and the Lagrangian for the fermion fields become [8]

$$\begin{aligned}\mathcal{L}_F = \sum_i \overline{\psi}_i \left(i\partial\!\!\!/ - m_i - \frac{g m_i H}{2 m_W} \right) \psi_i \\ -\frac{g}{2\sqrt{2}} \sum_i \overline{\psi}_i \gamma^\mu \left(1 - \gamma^5\right) \left(T^+ W_\mu^+ + T^- W_\mu^- \right) \psi_i \\ -e \sum_i Q_i \overline{\psi}_i \gamma^\mu \psi_i A_\mu \\ -\frac{g}{2\cos\theta_W} \sum_i \overline{\psi}_i \gamma^\mu \left(g_V^i - g_A^i \gamma^5 \right) \psi_i Z_\mu \end{aligned} \tag{2.23}$$

The first term of the fermion Lagrangian contains the fermion masses, m_i which are directly proportional to Yukawa coupling and vacuum expectation value

$$m = g_f \frac{v}{\sqrt{2}}. \tag{2.24}$$

The second term of the Lagrangian represents the charged weak current interaction, the third term represents the QED interaction and the last term is for the weak-neutral current interaction. The weak-neutral interaction is universal for all families for which the coupling terms are given by $g_v^i = T_i^3 - 2Q_i \sin^2\theta_W$ and $g_A^i = T_i^3$. The electromagnetic coupling constant e is related to the weak charge and the mixing angle,

$$e = g \sin\theta_W = g' \cos\theta_W \tag{2.25}$$

In the fermion Lagrangian the doublets

$$\psi_i = \begin{pmatrix} \nu_i \\ \\ l_i^- \end{pmatrix} \quad \text{and} \quad \begin{pmatrix} u_i \\ \\ d_i' \end{pmatrix} \tag{2.26}$$

represent the left-handed lepton and quark fields and $d_i' = \sum_j V_{ij} d_j$ where V_{ij} are the elements of the unitary CKM matrix which relate the electroweak eigenstates (d_i') to their mass eigenstates (d_j).

The leptons and quarks are grouped in three families. The grouping of

Table 2.1: Three families in the Standard Model

	generation	
first	second	third
u	c	t
d	s	b
ν_e	ν_μ	ν_τ
e^-	μ^-	τ^-

quarks and leptons in complete families are required to cancel the anomalies in the current-gauge coupling. For each complete family the relation $3(Q_u + Q_d) + Q_e = 0$ is satisfied in any quantum mechanical gauge theory evidently including the Standard Model.

It is important to note that discovering the Higgs boson might not necessarily show us how the fermions get their masses, and moreover the mechanism for neutrino masses might be different. There have been some attempts to find a simple explanation for the observed fermion masses (*e.g.* see [7]) but none have been completely successful yet.

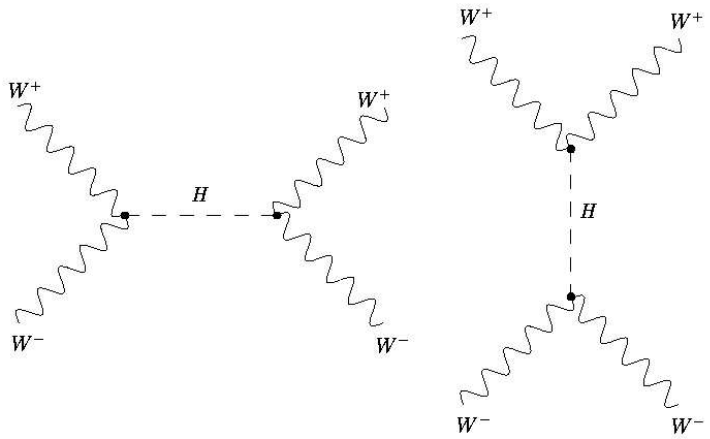

Figure 2.2: WW scattering with the exchange of a Higgs boson. The perturbative unitarity breaks down if $m_H \geq 1$ TeV.

2.0.2 Experimental and Theoretical Limits on the Higgs Boson

A weak upper limit to the Higgs boson mass can be obtained by theoretical arguments. It is shown in [32] that if the Higgs boson mass is $\sim (8\sqrt{2}\pi/3G_F)^{1/2} \sim$ 1 TeV, in the WW scattering with the exchange of an Higgs boson shown in Fig. 2.2, the amplitude becomes large and the perturbative unitarity breaks down. At this point, the interactions become strong suggesting that the Higgs boson is not a fundamental electroweak scalar [33]. This is a weak limit and the violation of this limit shows that the derivation of the bound by perturbative theory is not adequate. The parameter λ in the definition of the Higgs potential Eq. (2.11) depends on the energy scale, and λ at a fixed scale μ can be related

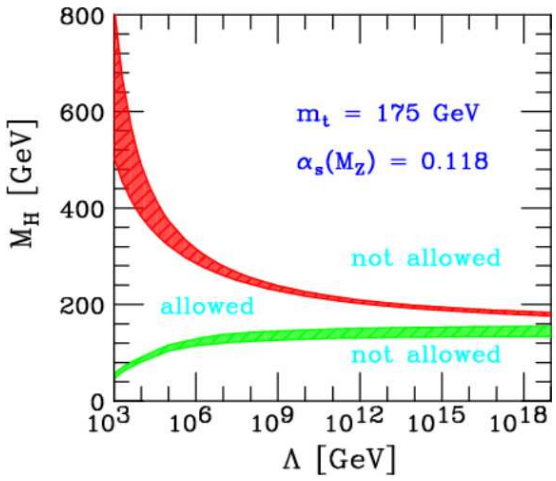

Figure 2.3: Higgs boson theoretical mass limits. The light-shaded areas are the forbidden zones. The upper limit is determined from the requirement of consistency of the electroweak theory up to the Λ scale. The lower limit is determined from the condition of absolute vacuum stability. The solid areas show the uncertainties in the bounds [19].

to the value of λ at another scale Λ with $\Lambda > \mu$,

$$\frac{1}{\lambda(\mu)} = \frac{1}{\lambda(\Lambda)} + \frac{3}{2\pi^2}\log(\frac{\Lambda}{\lambda}). \tag{2.27}$$

If $\lambda(\Lambda) < 0$ then the vacuum energy becomes $-\infty$. To prevent this, $\Lambda \leq \mu e^{2\pi^2/3\lambda(\mu)}$. This is equivalent to an upper limit for the Higgs boson mass if the energy scale is chosen to be m_H which is equal to $\sqrt{2\lambda}v$. A lower bound on the SM Higgs boson mass is obtained by higher-order the corrections to the Higgs potential fixing the absolute minimum at $v/\sqrt{2}$. A summary of theoretical Higgs mass limits are shown in Fig. 2.3. The upper limit is determined from the requirement of consistency of the electroweak theory up to the Λ scale. The lower limit is determined from the condition of absolute vacuum stability [6].

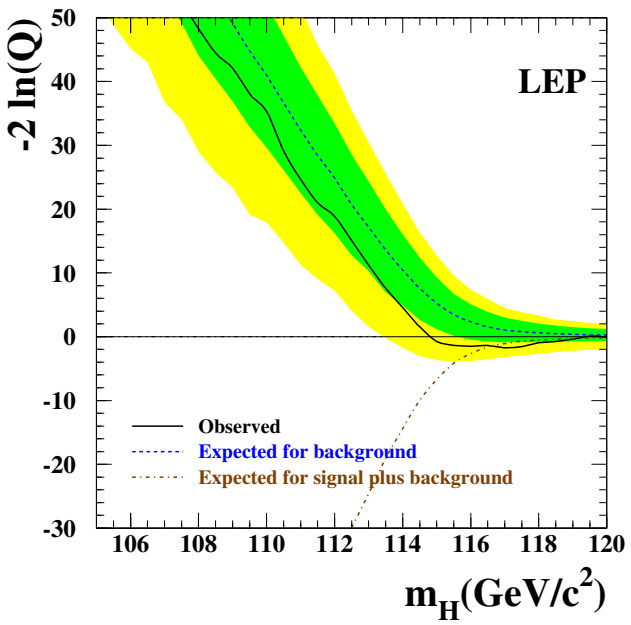

Figure 2.4: Solid line shows the observed and the dashed line the expected values for the test statistics parameter -2lnQ. Dark region represents 1σ and the light region represents 2σ around the mean. [35].

The mass of the SM Higgs boson must lie between $\sim$ 130 GeV/c^2 to 200 GeV/c^2 for the electroweak theory to be meaningful up to the Planck scale, and it should be less than $\sim$ 500 GeV/c^2 if the theory is to be valid up to 1 TeV. Better limits are provided by the experimental data, which will be explained below.

Higgs boson searches have been done in electron and hadron colliders [35]. Also, there are indirect searches that utilize the precision electroweak measurements [35]. The direct searches for the SM Higgs boson produced by $e^+ + e^- \rightarrow H + Z$ at LEP set the lower limit at 114.4 GeV/c^2 for a 95% CL [62]. This

is demonstrated in Fig. 2.4 as the Higgs mass value corresponding to the zero of the observed log-likelihood variable (-2lnQ). The minimum point of $-2\ln Q$ gives the central value for the Higgs mass as ~ 115 GeV/c^2.

Fig. 2.5 displays the SM Higgs boson production channels for the Tevatron Run II period. The center of mass energy of the Tevatron is 1.96 TeV. The most dominant Higgs production channel is the gluon fusion, $gg \rightarrow H$, followed by the associated production $qq \rightarrow VH$ channel with an electroweak vector boson, V where $V = Z$ or $W^{\pm}$. The $H \rightarrow b\bar{b}$ decay mode is dominant for Higgs masses less than about 140 GeV/c^2 and the searches are performed in these channels: $WH \rightarrow l^{\pm}\nu b\bar{b}$, $ZH \rightarrow l^{+}l^{-}b\bar{b}$, $WH, ZH \rightarrow jjb\bar{b}$ and $ZH \rightarrow \nu\bar{\nu}b\bar{b}$. The $H \rightarrow W^{+}W^{-}$ decay mode is dominant for masses higher than $\sim$ 140 GeV/c^2. In the HWW decay mode, one of the W-bosons may be virtual. The searches for Higgs bosons with mass higher than 140 GeV/c^2 are made in the following channels; $gg \rightarrow H \rightarrow W^{+}W^{-}(dileptons)$ and $WH \rightarrow W^{\pm}W^{+}W^{-}$(2 lepton and 3 lepton final states). About 1 fb^{-1} Run II Tevatron has been analyzed by CDF and D0 and until now no excess Higgs boson signal above the background is detected [17]. The upper limits accessible with the current analyzed data is a factor of $\sim 8-10$ larger for $m_H = 115$ GeV/c^2 and ~ 4 for $m_H = 160$ GeV/c^2 [17, 18]. Although still far from the SM predictions, Tevatron is getting closer to seeing the first indications of its existence. The current sensitivity to Higgs boson can be seen in the Figures 2.6 and 2.7.

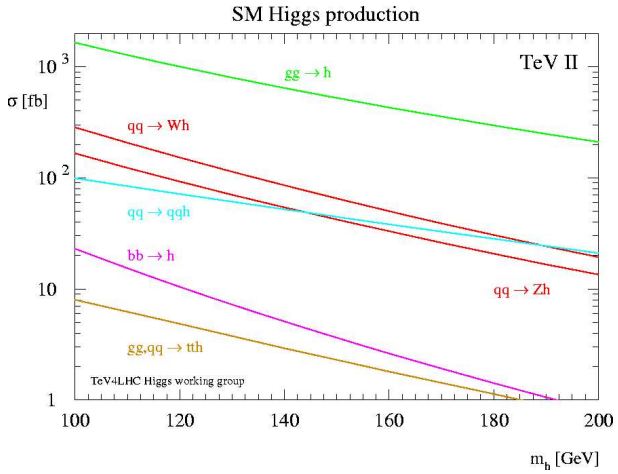

Figure 2.5: Higgs production for the dominant channels for Tevatron Run II. The center of mass energy is 2 TeV [14].

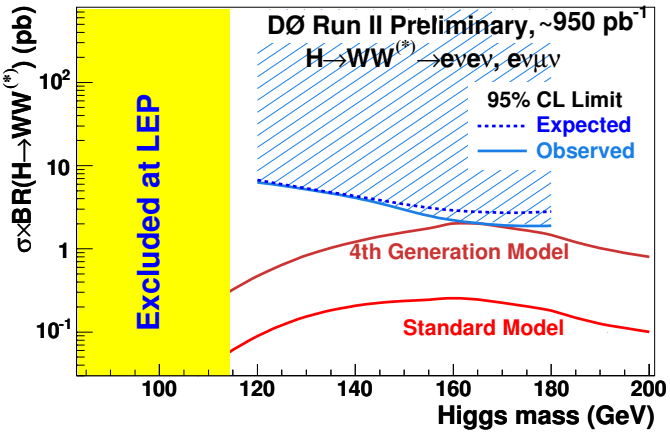

Figure 2.6: Search for the Higgs boson in $H \rightarrow WW* \rightarrow ll'(l, l' = e, \mu)$ decays with 950 pb^{-1} in D0 in Run II [34, 35].

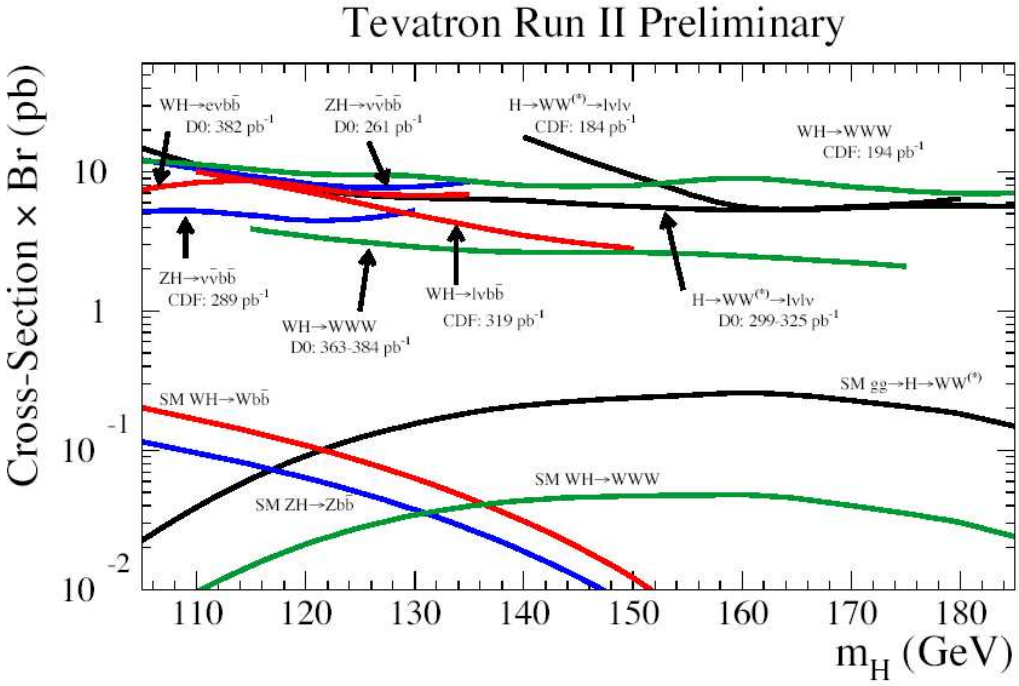

Figure 2.7: Tevatron run II preliminary upper limits by CDF and D0 experiments for the SM Higgs boson production. The upper curves represent the experimental limits at the 95% confidence levels and the curves in the lower part are the Standard Model predictions [35, 36].

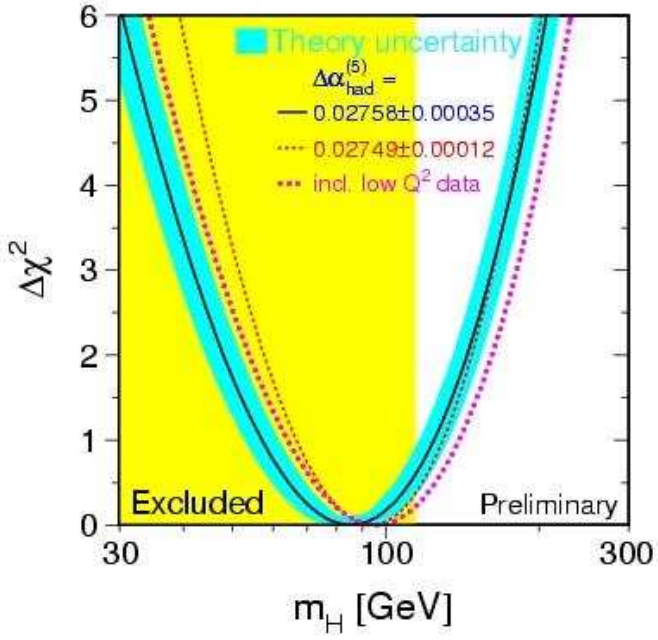

Figure 2.8: $\Delta\chi^2$ determined from a fit to electroweak precision measurements *vs* the Higgs boson mass. Solid line shows the fit. The band around the fit curve shows the uncertainty induced by the higher order corrections. The excluded region is determined from the direct searches at LEP corresponding to 95% CL [31].

The electroweak theory is constrained by α, G_F and m_Z. These parameters are related to each other at the tree level by the relations [33]

$$m_W^2 = \frac{\pi\alpha}{\sqrt{2}G_F \sin^2\theta_W}, \tag{2.28}$$

$$m_Z^2 = \frac{\pi\alpha}{\sqrt{2}G_F \sin^2\theta_W \cos^2\theta_W}, \tag{2.29}$$

$$m_W = m_Z \cos\theta_W. \tag{2.30}$$

Radiative loop corrections due to heavy quarks, Higgs and possible new particles that must be applied in the current energy scale of experiments affect the observed electroweak parameters. These corrections logarithmically depend on the Higgs boson mass. Therefore, Higgs boson mass can be constrained indirectly using the precision electroweak measurements. Global fits to electroweak measurements from LEP, Tevatron and SLD constrain the Higgs mass to be less than about 194 GeV [35] at 95% CL (see Fig. 2.8). Figures 2.9 and 2.10 show the Higgs mass constraints from m_W and m_t values. The global fit to all data yields $m_H = 89^{+38}_{-28}$ GeV/c^2, $m_t = 172.7 \pm 2.8$ GeV/c^2 [35]. Recently, CDF made a new measurement of the W mass (80.398 ± 0.025 GeV/c^2). Preliminary studies show that the global fit to the Higgs boson central value $m_H = 80^{+36}_{-26}$ GeV/c^2 and the LEPII upper limit $m_H < 189$ GeV/c^2 at 95% CL [30]. If the newest CDF and D0 combined top mass measurement $m_t = 170.9 \pm 1.8$ GeV/c^2 is used with the new W mass value, the upper limit for the mass of the Higgs boson becomes $m_H < 144$ GeV/c^2 at 95% CL [31].

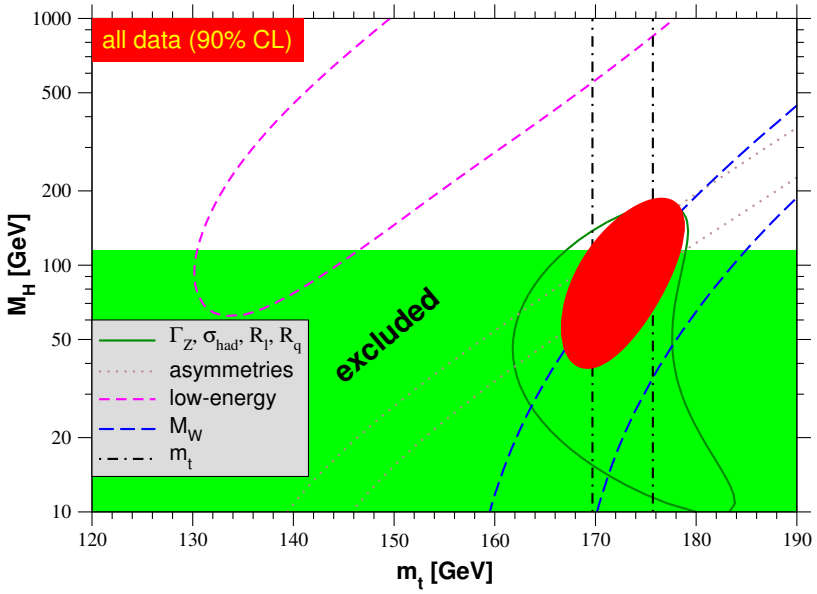

Figure 2.9: SM Higgs mass as a function of top mass [35].

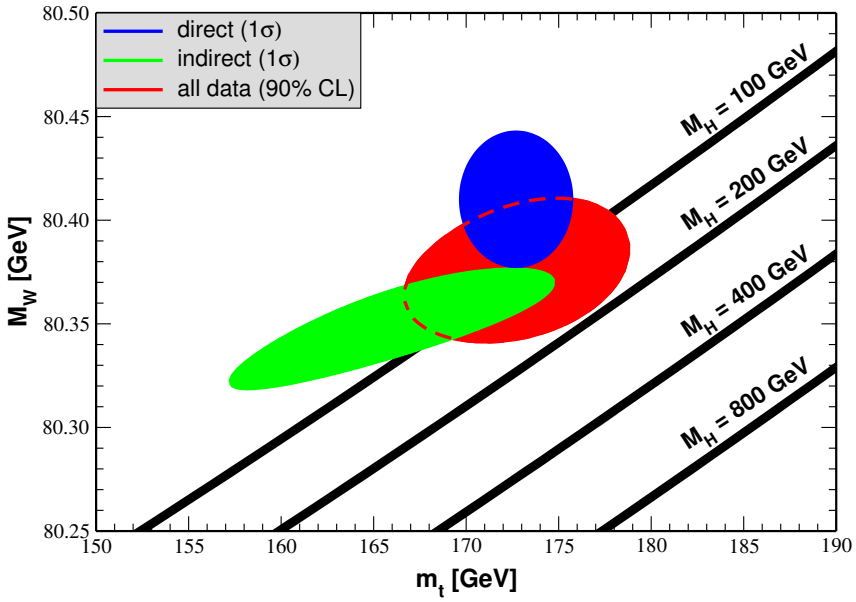

Figure 2.10: m_W *vs* m_t. The SM prediction for different Higgs masses are also shown [35].

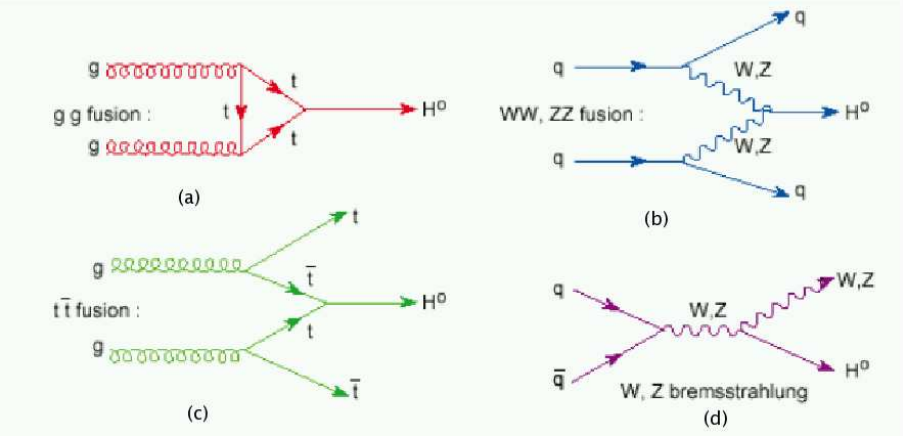

Figure 2.11: Feynman diagrams for the dominant Higgs production mechanisms at the LHC.

2.0.3 Standard Model Higgs Boson Searches at the LHC

2.0.3.1 Higgs Boson Production at the LHC

At the LHC, the dominant Higgs production mechanisms are gluon-gluon fusion ($gg \rightarrow H$), vector boson fusion ($qq \rightarrow qqH$), associated production with vector bosons ($q\bar{q} \rightarrow WH, ZH$) and associated production with top quark pairs ($gg, q\bar{q} \rightarrow t\bar{t}H$) for which the leading order Feynman diagrams are shown in Fig. 2.11. The cross sections vs Higgs boson mass for these processes along with the production processes with lower cross sections for the LHC are displayed in Fig. 2.12. The cross sections reported in Fig. 2.12 are fully inclusive without any acceptance cuts or any branching ratios.

The gluon fusion dominates the Higgs boson production for all the Higgs boson mass range because of the much larger gluon density in the proton than

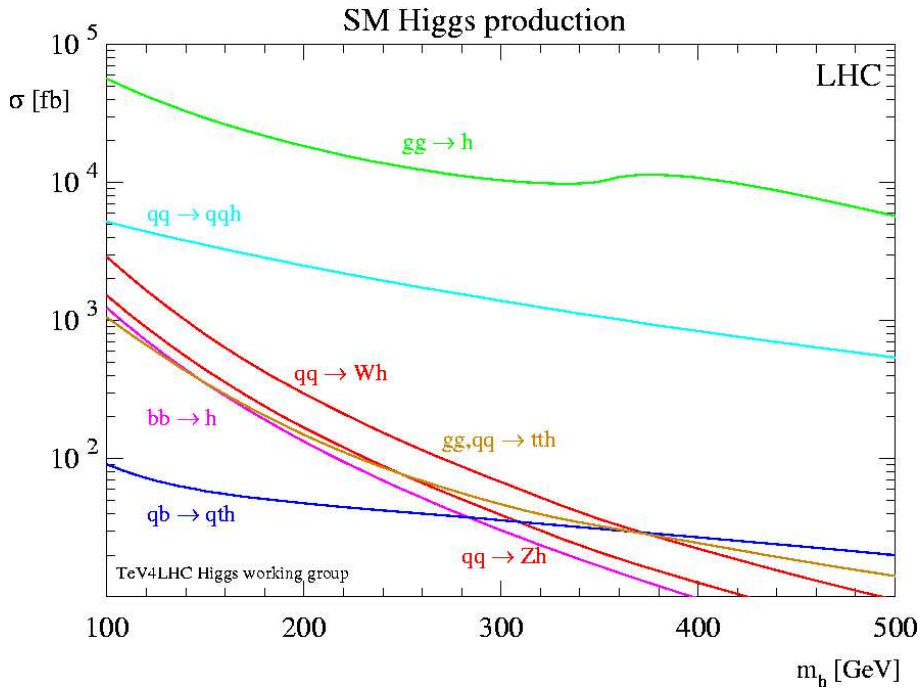

Figure 2.12: Higgs production for the dominant channels for the LHC where $\sqrt{s} = 14$ TeV [14].

the quark density at around 100 GeV masses at the LHC energy. As seen from the Feynman diagram of the process (Fig. 2.11 (a)), the process is mediated by a virtual top loop radiating a Higgs boson. There are large next-to-leading order (NLO) QCD corrections to this process. The corrections are known up to next-to-next-to-leading order (NNLO) [20, 21] and are included in Fig. 2.12. The theoretical uncertainty is about 10% [16].

Although the Higgs boson production rate via VBF is about an order of magnitude smaller, it is a promising channel for the discovery of a Standard Model-like Higgs boson, especially in the intermediate mass range $m_H \leq 2m_Z$. This is because of its unique kinematics and QCD properties. Fig. 2.12 includes the NLO QCD and leading-order electroweak corrections, and the PDF used is CTEQ6M [28, 29] with the renormalization and factorization scales at the Higgs boson mass. The uncertainty is smaller than $\sim$10% [16]. VBF channel is characterized by two forward jets with transverse momentum $p_T \sim m_W/2$ and between the forward jets a large rapidity gap in which the decay products of the Higgs boson lie. The topology of a typical Higgs event is shown in Fig.2.13. In the case when the Higgs boson decays to two W-bosons, the HWW vertex both in production and decay provides a relatively clean access to the HWW coupling which is very important for establishing the origin of electroweak symmetry breaking. The search for a Standard Model Higgs boson in this channel in CMS with $H \rightarrow WW \rightarrow l\nu l\nu$ is one of the main topics of this thesis and will be

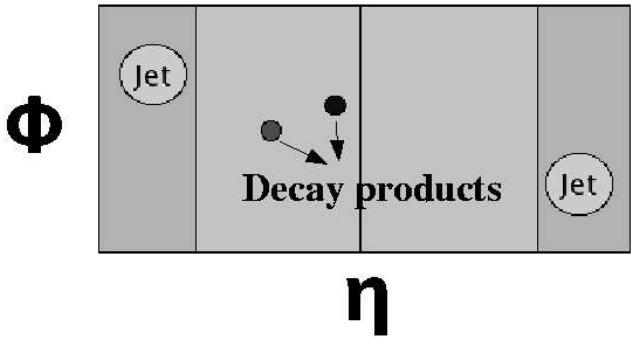

Figure 2.13: A typical VBF event with the forward/backward jets and the two leptons in the central region.

described in detail in Chapter 5.

The associated production with a W or a Z boson is also referred to as the Higgs-strahlung. The decay products of W or Z bosons are used to identify such events. This channel is effective in the intermediate mass range. The NLO QCD corrections enhance the total production cross section by about 30% [22, 23]. The NNLO QCD corrections increase the cross section by about another 10% [15], and the scale dependence for this calculation is ∼1%. The electroweak corrections decrease the total cross section up to ∼10% [24]. The uncertainty from the parton distribution functions in this channel is less than 5% [24].

The associated production with a $t\bar{t}$ pair is effective for Higgs boson masses less than about 150 GeV/c^2. The cross section reported in Fig. 2.12 includes the NLO QCD corrections which increases the total leading-order cross section

by ∼20% [25, 26, 27]. The PDF used is CTEQ6M with the renormalization and factorization scales set at $m_t + m_H/2$ [16].

2.0.3.2 Higgs Boson Decays

Since the Higgs couples to higher mass particles more strongly, the probability of the Higgs boson to decay into the high mass particles is larger as long as the kinematics allows. The branching ratios for the SM Higgs boson as a function of Higgs boson mass are displayed in Fig. 2.14 in the Higgs mass range ∼80 - 500 GeV/c^2. The most dominant decay modes of the Higgs boson are expected to be into $b\bar{b}$ and $\tau^+\tau^-$ pairs for Higgs boson masses less than about 130 GeV/c^2. In this mass range, the other decay modes are not significant except for $\gamma\gamma$ at the LHC. For Higgs boson masses larger than 130 GeV/c^2, the two main decay modes are expected to be into W^+W^- and ZZ pairs . One of the vector bosons in these decays can be virtual. As seen in Fig. 2.14 at m_H ∼160 GeV/c^2, the branching ratio into W^+W^- bosons becomes ∼100% when the W bosons produced are allowed to be on-shell. The other decay mode, $t\bar{t}$ has a small probability. It increases with mass and only rises to ∼20% for Higgs boson masses above 400 GeV/c^2. The total decay width of the Higgs boson is ∼1 GeV at $m_H \sim 200$ GeV/c^2 and becomes about a TeV at $m_H \sim 1$ TeV/c^2.

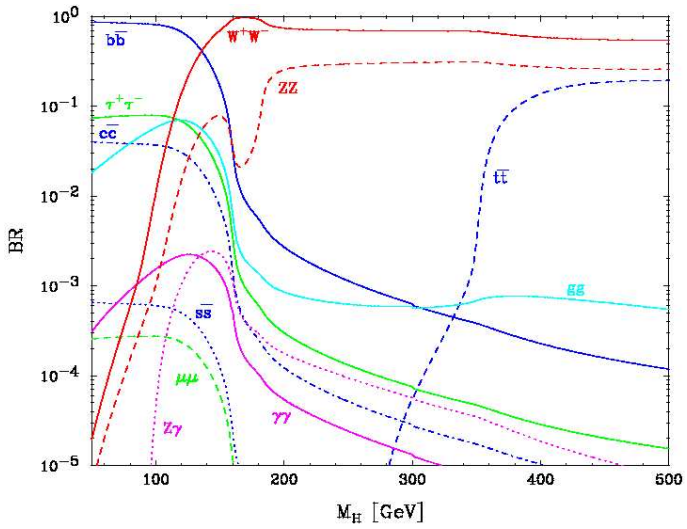

Figure 2.14: Branching ratios for the standard model Higgs boson *vs* mass [12]

2.0.3.3 Search Strategies for the Higgs Boson at the LHC

$H \rightarrow \gamma\gamma$ is one of the most important channels for Higgs searches at the LHC for the Higgs boson masses in the range ∼110-150 GeV/c^2. The signature for the $H \rightarrow \gamma\gamma$ channel is two high E_T isolated electromagnetic clusters. Although the branching ratio into two γ's is very small, the Higgs signal can be observed as a small but narrow peak ($\delta M_{\gamma\gamma} < 1\%$) in the di-photon mass distribution (over a large background) [59]. The background consists of two prompt photons, one prompt photon + jet (bremstrahlung photons, photon from π^0 decay) and dijets. The background can be measured from the sidebands outside the peak position. This channel is extensively studied in CMS utilizing both the standard cut based analysis as well as an optimized analysis for the discovery [59].

$H \rightarrow ZZ^{(*)} \rightarrow l^+l^-l^+l^-$ channel is one of the most promising processes that might lead to the discovery of a Higgs boson at the LHC. The branching ratio for $H \rightarrow ZZ^{(*)}$ is not small for $m_H > 130$ GeV/c^2. The branching ratio is ~20% for $m_H \geq 2m_Z$ (Fig. 2.14). The main backgrounds for this channel are $ZZ^{(*)}$, $t\bar{t}$ and $Zb\bar{b} \rightarrow l^+l^-b\bar{b}$. After the selection cuts, the remaining background is $ZZ^{(*)}/\gamma^*$. This background can be measured by normalization to the $Z \rightarrow l^+l^-$ data. The background can also be measured by normalizing to the sidebands of the signal in the invariant mass of the four-leptons [59]. Both of these methods individually can reduce the luminosity uncertainties totally and can partially reduce the PDF, scale and experimental uncertainties. $H \rightarrow ZZ^{(*)} \rightarrow l^+l^-l^+l^-$ channel also offers the opportunity to measure the mass and the production cross section of the Higgs boson. It can also be used to measure the spin and CP properties of the Higgs boson [37]. Moreover, combining the $ZZ^{(*)}$ and $WW^{(*)}$ decay modes might help in reducing the systematic uncertainties in the Higgs boson coupling measurements.

Another significant channel for Higgs boson discovery is $H \rightarrow WW^{(*)} \rightarrow l\nu l\nu$ in which the Higgs boson is produced by gluon-gluon fusion and vector boson fusion. This channel is important in the Higgs boson mass range from 120 to 200 Fig. 2.14. The dominant backgrounds for this process are $q\bar{q} \rightarrow W^+W^- \rightarrow l\nu l\nu$, $gg \rightarrow t\bar{t} \rightarrow \mu\nu\mu\nu$, $q\bar{q} \rightarrow \gamma^*$ and $Z \rightarrow l^+l^-$. The other contributing background processes are $b\bar{b} \rightarrow 2l$, $ZW \rightarrow 3l$, $tWb \rightarrow 2l$ and $ZZ \rightarrow 2l$. The background

can be measured directly from the data using a region of the phase space that is signal-free. One possible method particularly useful for the $t\bar{t}j$ background estimation is described in detail in Chapter 5 for the $H \rightarrow WW^{(*)} \rightarrow 2l2\nu$ channel in which the Higgs is produced by VBF.

For the Vector Boson Fusion, one of the channels that is important in Higgs Boson searches is $qqH \rightarrow qq\tau\tau \rightarrow l + \tau^{jet} + \not{E}_T$. This channel has potential in the mass range from the LEP lower limit to ∼145 GeV/c^2 above which the branching ratio drops abruptly. The major backgrounds to this channel are the QCD 2τ + 2 or 3 jets, EW 2τ+2 jets, W+jets and $t\bar{t} \rightarrow WbWb$ [59, 39].

$qqH \rightarrow qq\gamma\gamma$ channel has potential up to about 150 GeV/c^2. The main backgrounds to this channel are QCD multi-jets, Drell Yan e^+e^- pair production, gluon fusion producing two photons with two additional jets, $pp \rightarrow 2\gamma + 2$ jets and $pp \rightarrow 2\gamma + 3$ jets.

$qqH \rightarrow W^+W^- \rightarrow l^{\pm}\nu jj$ is another potential discovery channel for the Higgs boson. It is also complementary to $qqH \rightarrow W^+W^- \rightarrow l\nu l\nu$ channel in the ∼160-180 GeV/c^2 mass range where the probability to decay into two W's is the highest. This channel also has potential for discovering high-mass Higgs bosons. The major backgrounds are $t\bar{t}j$, $W + t\bar{b}(\bar{t}b)$, $W/Z + jets$, $WW/WZ/ZZ + jets$ and QCD background.

Searches for the Higgs Boson decaying into two photons in the associated $t\bar{t}$H and VH can be done at high luminosity. The channel is significant for the Higgs

boson masses from 115 to ∼150 GeV/c^2. The Higgs mass can be reconstructed in the inclusive H→ $\gamma\gamma$ channel [59].

Figure 2.15 shows the statistical significance of the signal as a function of the mass of the Higgs boson for an integrated luminosity of 30 fb^{-1} for different production and decay channels and the corresponding luminosity needed for 5σ discovery. The ATLAS Higgs reach for 30 fb^{-1} is shown in Figure 2.16. Comparing the Higgs boson discovery potential in CMS and ATLAS for 30 fb^{-1}, in the H→ $\gamma\gamma$ channel, CMS can make the discovery with a significance larger than 5σ for $m_H < 150$ GeV/c^2, while ATLAS significances are always lower than 4σ. In the $H \rightarrow ZZ \rightarrow 4l$ channel, CMS is capable of discovering the Higgs boson with $> 5\sigma$ in the Higgs boson mass range $m_H = 120 - 160$ GeV/c^2 and $m_H = 180 - 600$ GeV/c^2 and ATLAS can make the discovery in the mass range $m_H = 130 - 165$ GeV/c^2 and $m_H > 175$ GeV/c^2. In the $H \rightarrow WW \rightarrow 2l2\nu$ channel, both CMS and ATLAS can make a Higgs boson discovery for $m_H = 130 - 190$ GeV/c^2. CMS seems not to be capable of making a 5σ discovery in the qqH, $H \rightarrow \tau\tau$ channel, while ATLAS can make it for $m_H = 120 - 135$ GeV/c^2.

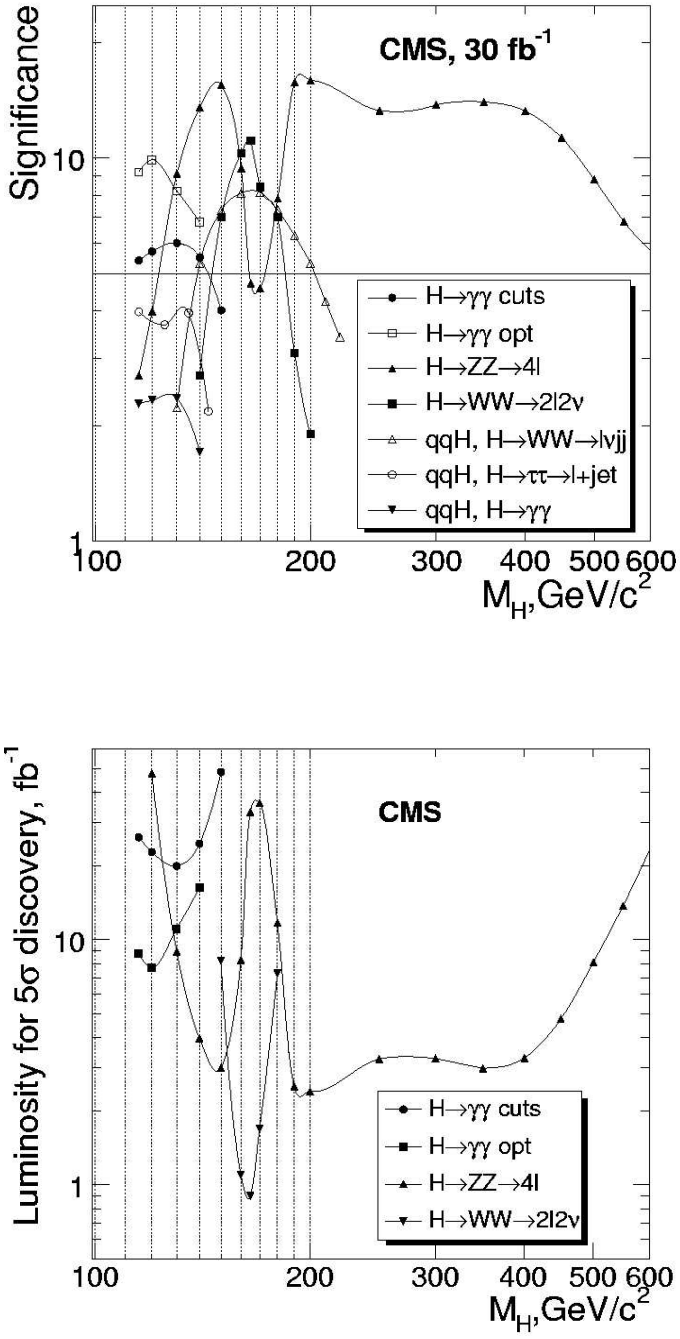

Figure 2.15: The statistical significance for an integrated luminosity of 30 fb^{-1} of Higgs boson reach for CMS (top) and the needed integrated luminosity to achieve a 5σ discovery (bottom) [59].

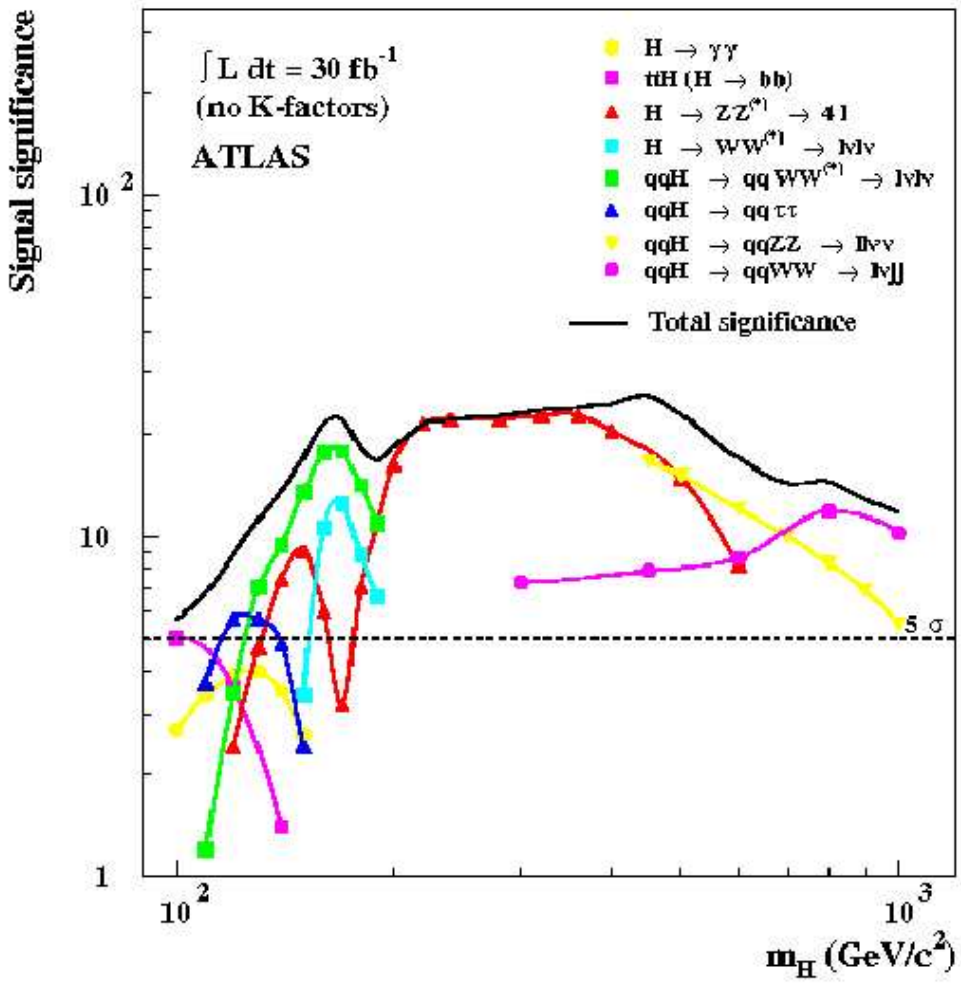

Figure 2.16: The statistical significance for an integrated luminosity of 30 fb^{-1} of Higgs boson reach for ATLAS [39].

CHAPTER 3

THE EXPERIMENT

3.1 Large Hadron Collider (LHC)

Large Hadron Collider (LHC) will be the most powerful instrument ever built to investigate particles and their interactions. LHC will collide beams of protons at a center of mass energy of 14 GeV. One of the main goals of LHC is to find out the mechanism(s) behind electroweak symmetry breaking. LHC is built in the existing Large Electron-Positron (LEP) tunnel at CERN, Geneva. The luminosity goal of LHC is 10^{34} cm^{-2}s^{-1}. LHC is a two-ring accelerator in the same tunnel where the circumference of the LHC tunnel is $\sim$ 27 km. LHC is located 50-175 m underground. Collisions of the full energy of 14 TeV is planned for the spring of 2008. (Apart from colliding proton beams, it also can collide lead (Pb) ions with energy of 2.76 TeV/nucleon.) The relativistic $\gamma = (\sqrt{1 - v^2/c^2})^{-1}$ factor will be 479.6 at the injection and 7461 at the collision points. For most of the ring, the beams will travel in two separate vacuum pipes. The beams of protons will be made to collide at four interaction points. These interaction points are surrounded by large detectors; the Compact Muon Solenoid (CMS), A large

Toroidal LHC Apparatus (ATLAS), Large Hadron Collider b-quark experiment (LHCb) and A Large Ion Collider experiment at CERN (ALICE). Total cross section Elastic scattering and diffraction dissociation at the LHC (TOTEM) and LHC forward (LHCf) focusing on forward physics will be installed near CMS and ATLAS experiments, respectively. The overall view of the LHC experiments is shown in Figure 3.1. CMS detector will be described in detail in Section 3.2.

The injector complex consists of Linac2, Linac3, the booster, the Low Energy Ion Ring, the PS and the SPS. The beams will be injected from SPS with an energy of 450 GeV by two fast pulsed magnet systems each of which produces magnetic pulses of 1.3 Tesla-meters with a risetime of at most 900 ns. The ratio of the active structure in a period to the total length (the packing fraction), at LHC is $\sim 65\%$ so that the total bending arc-length in the main ring is $27 \times 0.65 = 17.6$ km which corresponds to a bending radius of ~ 2.8 km. The magnetic field needed to make the protons orbit each ring at 7 TeV is $B = p/(0.3\rho) = 8.33\ T$. To achieve this, the total number of magnets used around the ring is ~ 9300. The number of main dipoles is 1232, each of which is 35 tonnes and 15 m long. Superconducting magnets operated at superfluid He temperatures are used to obtain the highest possible fields at an affordable power consumption. The superconducting dipole magnets are one of the key elements for the LHC. The operating temperature of the He will be 1.9 °K and will be provided by a huge cryogenics supply system. It is able to transport over 140 kW at 4.5 °K more

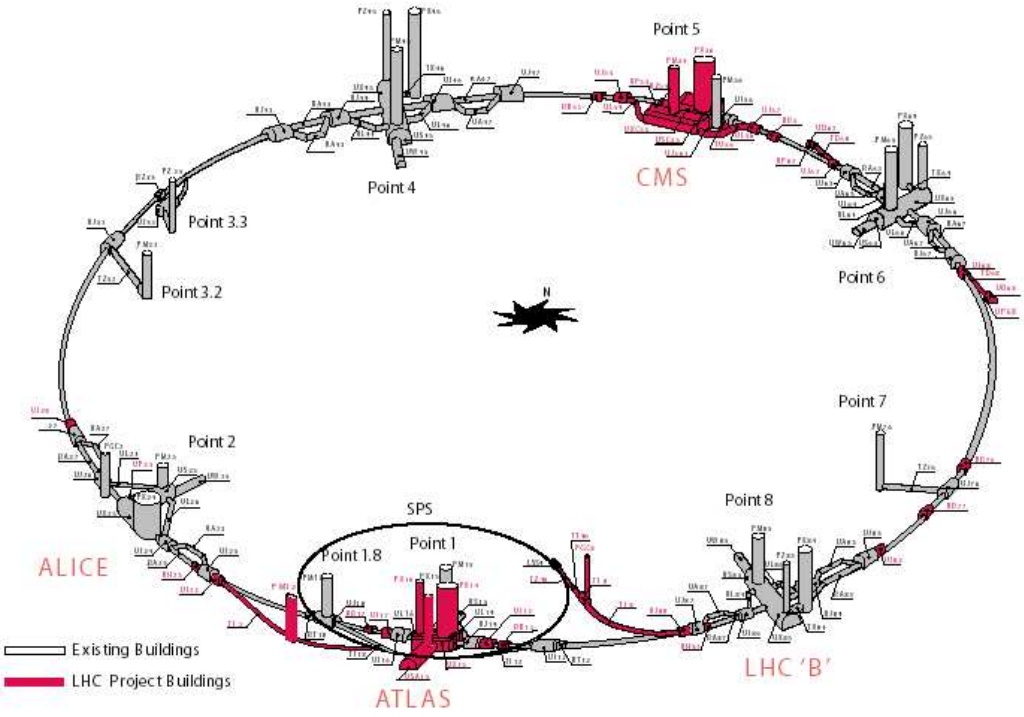

Figure 3.1: Structure and experiments of the LHC [40].

than a kilometer with a temperature change of less than 0.1 °K. The magnets are powered by AC to DC converters in which the delivered current depends very strongly on the magnet that is fed. There will be 8 RF cavities per beam and the field strength at peak energy is ~ 5.5 MV/m.

Each proton beam at full intensity will consist of 2808 bunches. Each bunch will contain 1.15×10^{11} protons (required for 10^{34} cm^{-2}s^{-1}) at the start of nominal fill and the Gaussian bunch length will be 11.24 cm and 7.55 cm at injection and collision, respectively. The transverse dimensions of the beam will be about

Table 3.1: Some of the LHC parameters relevant for CMS and ATLAS [40]

	pp
Collision Momentum	7 TeV
Beam energy at Injection (SPS)	450 GeV
Circumference	27 km
Dipole field at 7 TeV	8.33 T
Design Luminosity	10^{34} cm^{-2}s^{-1}
Bunch spacing	25 ns
No. of bunches	2808
No. of particles per bunch	1.15 10^{11}
Number of collisions/crossing	$\sim$20
Operating temperature	1.9 K
Number of dipoles	1232
Number of quadrupoles	858
Number of correcting magnets	6208
Number of RF cavities	8/beam
Δ highest & lowest pnts.	122 m
F(θ)	0.836
Energy loss/turn	$\sim$7 keV

a millimeter, but at the collision point low-beta[1] quadrupoles will squeeze it to $\sim$ 16 microns. The stored energy per beam is 362 MJ which makes the large collimation and protection systems vital. The spacing of the bunches in time will be 25 ns and in space about 7.5 m. However, due to the filling scheme from the SPS, the structure of the bunch spacings is more complex. Gaps in the bunch structure are used for synchronization, calibration, and resetting the front-end-electronics. The PS forms 25 ns spaced 26 GeV bunches. Then SPS increases the beam energy to 450 GeV.

[1] The term "low-beta" comes from the beta function which is proportional to the size of the beam

The number of interactions per unit time or event rate R can be found from $R = L \times \sigma$, where L is the luminosity and σ is the inelastic cross section. The peak LHC luminosity at the interaction points 1 (ATLAS) and 5 (CMS) will be $\sim 10^{34}$ cm^{-2}s^{-1}. The inelastic pp cross section ~60 mb. Therefore, the inelastic event rate will be 6×10^8 events per second. For counter-rotating bunches of N_p particles with the collision frequency of f, the luminosity is given simply by

$$L = \frac{f N_p^2 F(\theta)}{4\pi\sigma_x\sigma_y} \tag{3.1}$$

where σ_x and σ_y are the transverse areas where the two beams overlap and $F(\theta)$ is the factor for the luminosity reduction due to crossing-angle, θ. Crossing angle is needed because otherwise there would be about 30 bunch interactions around the interaction region. $F(\theta)$ depends also on the bunch length. $F(\theta)$ is $\sim$ 85% for LHC and the collision frequency, is f= 40 MHz. The beam-size varies with the inverse square-root of the γ-factor and it is $\sim$ 17 μm for the LHC. To achieve a luminosity of 10^{34} cm^{-2}s^{-1}, the LHC will be filled with 2808 bunches with $\sim 10^{11}$ particles per bunch.

The first physics run is expected in spring 2008, first with 75 ns bunch spacing then with 25 ns. The luminosity after the first year is expected to be 2×10^{33} cm^{-2}s^{-1}. This is referred as the low luminosity run, and the physics analysis presented in Chapter 5 is valid for the low luminosity period. After the first year of the physics run with proton-proton collisions, some runs with heavy ions will start.

Although the proton collision energy is 14 TeV, the maximum parton energy available will be $\sqrt{x_1 x_2 s}$ where x_1 and x_2 are the momentum fraction of proton's momentum carried by each parton in a frame in which the proton's momentum is large, and $\sqrt{s}$ is the center of mass energy. LHC will be able to probe the physics at several TeV. The total proton-proton cross section at 14 TeV is ~ 110 mbarns with 60 mbarns contribution from inelastic, 12 mbarns single diffractive and 40 mbarns elastic [13]. Proton-(anti)proton cross sections at the Tevatron and LHC are displayed in Figure 3.2. The Higgs cross section for a 150 GeV Higgs is about 10^9 times smaller than the total inelastic cross section. Note that at the LHC, the cross section for $m_H = 150$ GeV increases by about 100 times over the Tevatron. But, $t\bar{t}$ cross section increases by 200. Elastic and diffractive events produce particles with very small angles to the beam axis. These will be detected by the TOTEM detector [46].

The LHC parameters are summarized in Table 3.1 and the details of the LHC machine can be found in the LHC Design Report [40].

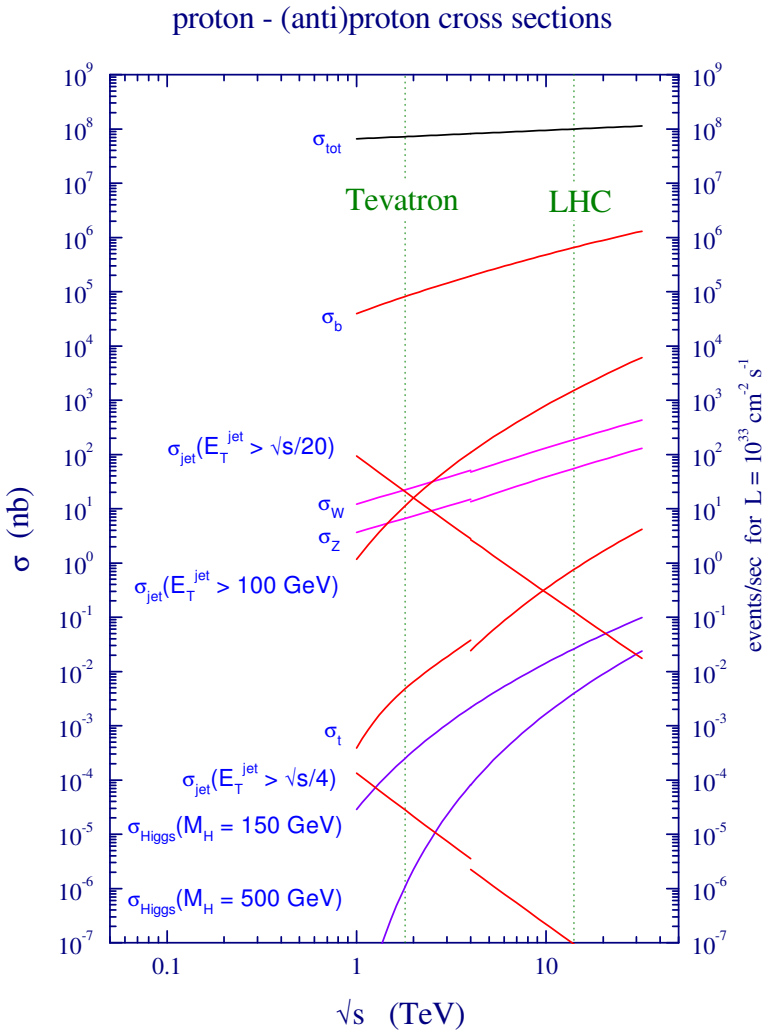

Figure 3.2: Proton-(anti)proton cross sections at Tevatron and LHC as a function of center of mass energy [13].

3.2 The CMS Experiment

The Compact Muon Solenoid (CMS) [47] is a multipurpose detector that is designed to measure particles from proton-proton collisions at the LHC. Its design is optimized for detecting the Higgs boson and other new particles. The CMS detector is shown in Figures 3.3, and 3.4. CMS consists of 100 million separate detecting elements. It is located 100 m underground in Cessy, France. It weighs 12500 tonnes. The CMS is the shape of a cylinder $\sim$21 m long and with a diameter $\sim$15 m. The CMS has an onion structure in which each layer is a subdetector. Although it is a cylindrical detector, it has a coverage of almost 4π. From inside to outside, the CMS detector consists of the pixel detector, silicon tracker, electromagnetic calorimeter (ECAL), hadronic calorimeter (HCAL), superconducting coil and the muon detectors. The CMS superconducting magnet generates 4 Tesla field (corresponding to about 2.7 GJ of stored energy) which is essential for having a high momentum resolution and distinguishing particles in high multiplicity events.

CMS is centered on the collision point 5 at the LHC (see. Fig. 3.1). The CMS convention for coordinates defines the z axis parallel to the beam pointing to the north-west (at the Jura mountains), the y-axis points upwards and x-axis points to the center of the LHC ring. The azimuthal angle ϕ is defined with relative to the positive x-axis and the polar angle θ is defined relative to the

positive z-axis. The pseudo-rapidity can be defined as $\eta = -\ln[\tan(\theta/2)]$. The transverse momentum ($p_T = p\sin\theta$) and the transverse energy ($E_T = E\sin\theta$) lie in the x-y plane. The set (ϕ, η, p_T, p_z) is a complete and convenient set of variables to describe particle kinematics in colliders.

3.2.1 The CMS Magnet - Superconducting Solenoid

The uniform 4 Tesla magnetic field, required to achieve a muon momentum resolution of $\sim$ 10% at a momentum of 1 TeV, is produced by the superconducting solenoid of CMS that make up the helical winding of the coil. This field strength is achieved by passing a 20 kA of current in the niobium-titanium superconductor. The magnet is 12.9 m long and has an inner diameter of 5.9 m. Except for the outer hadron calorimeter (HO), the calorimeters and the tracking detectors are in the magnet bore. The iron return yoke interspersed with muon chambers, returns the magnetic flux. Details on the CMS magnet can be found in the Magnet TDR [41].

3.2.2 Muon System

Many interesting physics events (like $H \rightarrow ZZ^*/WW^* \rightarrow \mu\mu ll$ and $Z' \rightarrow \mu\mu$) are expected to have at least one muon in final state. Muons are the only charged particles (coming directly from the primary collision) that are not absorbed by the calorimeters. Muons deposit only minimum ionizing energy in

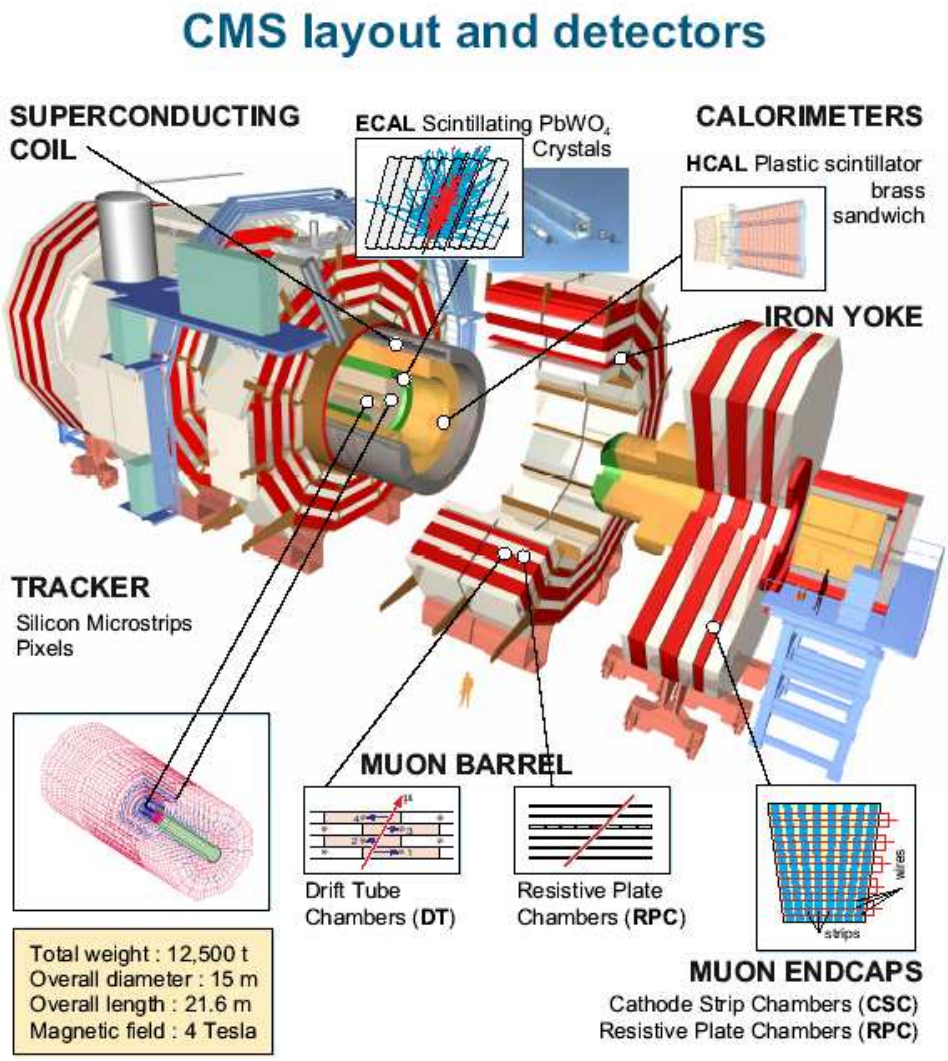

Figure 3.3: Schematic view of CMS.

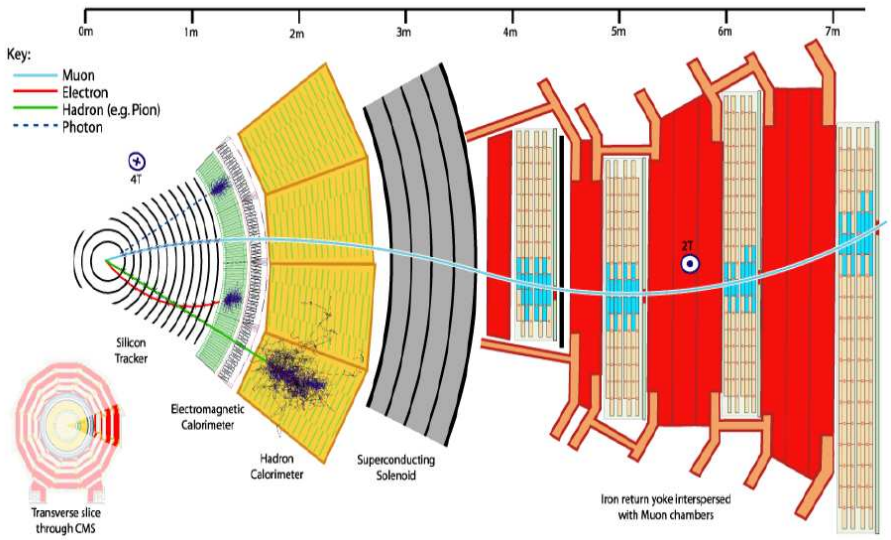

Figure 3.4: The CMS Experiment

the electromagnetic and the hadronic calorimeters. In general, a high energy particle is identified as a muon if it passes through a large amount of material with a little energy loss and with small deflection. Muons are relatively easy to detect with high accuracy due to the fact that they have no strong interactions and have long lifetimes (2.2 μs). The muon detectors in CMS are located behind the calorimeters and the magnet coil.

The CMS muon system uses three different types of detectors, the drift tubes (DT) located in the barrel $|\eta| < 1.2$, cathode strip chambers (CSC) in the endcaps ($0.9 < |\eta| < 2.4$) that have faster response and finer segmentation, and resistive plate chambers (RPC) located at barrel and endcaps ($0 < |\eta| < 2.1$). The DTs and CSCs are mainly used for tracking, p_T triggering and bunch

crossing identification. The RPCs are dedicated trigger detectors with good timing resolution of ~ 3 ns that are not used for tracking except for resolving ambiguities [11, 42]. The muon system has 250 DTs, 540 CSCs and 912 RPCs. Barrel region of the muon system consists of 5 rings of iron structures. Each ring is divided into 12 sectors. The muon system in the barrel has four stations and integrated into the iron yoke. Each station is composed of 3 layers of chambers. DT chambers are composed of 4 layers of DTs. Totally, there are 70 chambers for the outmost station and 60 in each of the inner stations. Muon system layout is displayed in Figure 3.5.

In the barrel region, the neutron-induced background and muon rates are small. In the barrel region, the iron yoke confines the magnetic field, and the field is uniform and low inside the muon stations. In the endcaps, the magnetic field is non-uniform and it can be as high as ~ 3.5 T. The spatial resolution for an RPC is just its cell size which is about one centimeter. The spatial resolution of the DTs is $\sim 100\ \mu m$ in $r-\phi$ space and $\sim 150\ \mu m$ in $r-z$ space. The resolution of the CSCs is $< 100\ \mu m$ [42]. Both the DTs and CSCs have trigger spatial resolutions of $\sim 1-2\ mm$ and bunch crossing identification efficiency of $\sim 99\%$ at the maximum LHC interaction rates. RPCs combined with DTs and CSCs provide very good triggers. RPCs are two highly resistive plate pairs in which the plates in each pair are separated by 2 mm gap filled with a gas mixture (mostly $C_2H_2F_4$, few percent of $iso-C_4H_{10}$ and less than a percent

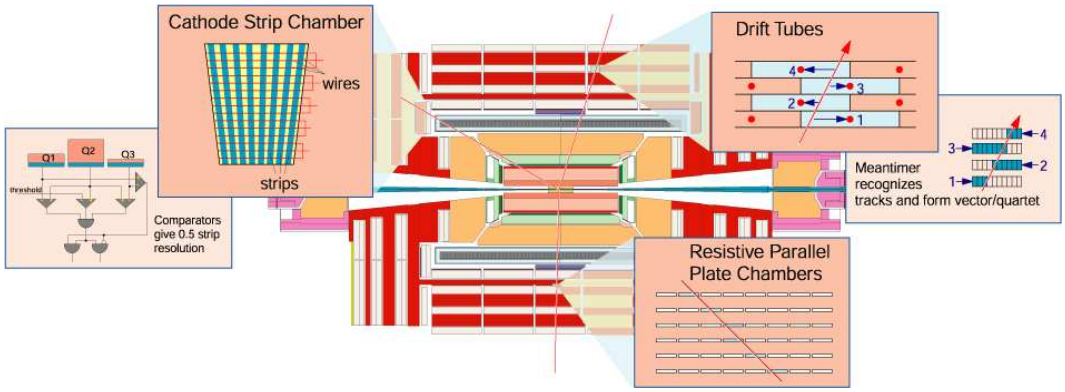

Figure 3.5: Layout of the muon system [48].

of SF_6). The detectors are operated at $\sim 10\ kV$ utilizing the graphite coating of the plates. The generated electric field inside causes an avalanche along the path of the particle. The avalanche makes a signal in the strips outside the gas volume which are isolated from the graphite coating. DT cells are filled with a gas mixture of 85% Ar and 15% CO_2 [42]. The electrons generated in the DTs move to anode wire in the center, and due to the high electric field close to the wire, the signal is amplified. The position of the track is measured by the time needed for the electrons to reach the wire. DTs use mean-timer circuits that enable a fast trigger [43] and the time resolution of DTs is 5 ns [42]. The CSC in the station that is closest to the interaction point has the finest segmentation to obtain a very precise momentum measurement. CSC chambers in each station consists of 6 layers of radial strips and 6 layers of tangential wires. The time resolution of CSC's is 6 ns.

The muon detectors provide measurement of p_T after the coil, and also the

measurement of sagitta in the return yoke. These measurements can be used for trigger and offline event reconstruction. In the inner tracker, sagitta measurement can be done. When the bending angle, the sagitta measurement in the muon system, and the inner tracker and the vertex position are combined, a resolution of 15 mm can be obtained.

The muon spectrometer has a laser system to align the muon stations to each other and to the tracker. The alignment system monitors the positions of the detectors. The system provides a single hit resolution of $\sim 220\mu m$ in DT's and CSC's.

The muon system is capable of providing extremely pure muon sample with no loss and identifying narrow physics signal peaks over backgrounds. The muon system (combined with the tracker) can identify muons with high efficiency and with good momentum resolution in $|\eta| < 2.5$. The momentum resolution is limited by the bending angle measurement which depends on the accuracy of the tracking and multiple scattering. The resolution is directly proportional to the square root of the amount of material in the muon system in units of X_0(radiation length) and inversely proportional to $\int Bdl$. For high p_T ($\sim 1\ TeV$) the momentum resolution is proportional to the spatial resolution of the muon chambers. Up to the last muon station the thickness of the absorber is 16 interaction lengths, up to $|\eta| \sim 2.4$. Good muon identification is achieved by absorption of charged particles before the muon system in ECAL and HCAL,

and in the muon system by the iron yoke. Moreover, the muon system is able to measure the charge of the muons up to about 1 TeV. The muon system can withstand the radiation environment, high rate interaction background of the LHC, and strong magnetic field in the iron yoke.

A more complete description of the Muon System can be found in the Muon TDR [42].

3.2.3 Electromagnetic Calorimeter (ECAL)

ECAL[51] is a hermetic and homogeneous calorimeter. It is made of lead-tungstate($PbWO_4$) crystals of high density (8.3 g/cm^3), small Moliere radius (2.2 cm), and are radiation-hard. The scintillation light is emitted with a time scale on the order of the LHC bunch crossing time (25 ns). It consists of about 61000 crystals in the ECAL barrel (EB) and about 7300 crystals in the ECAL endcaps (EE). The layout of the ECAL detector is displayed in Fig. 3.6.

The distance of the EB crystals to the interaction point measured from their faces is 1.29 m. The barrel part is composed of 36 identical supermodules and each supermodule has 4 modules. The EB extends to $|\eta| < 1.48$. Each crystal covers $\Delta\eta \times \Delta\phi = 0.0174 \times 0.0174$ corresponding to 22×22 mm^2 at the front face and 26×26 mm^2 at the back. The length of each crystal is 23 cm, equivalent to $\sim$ 26 radiation lengths (X_0). To reduce the gaps between the crystals, the crystals are placed such that their axis have a 3^o angle with respect to the

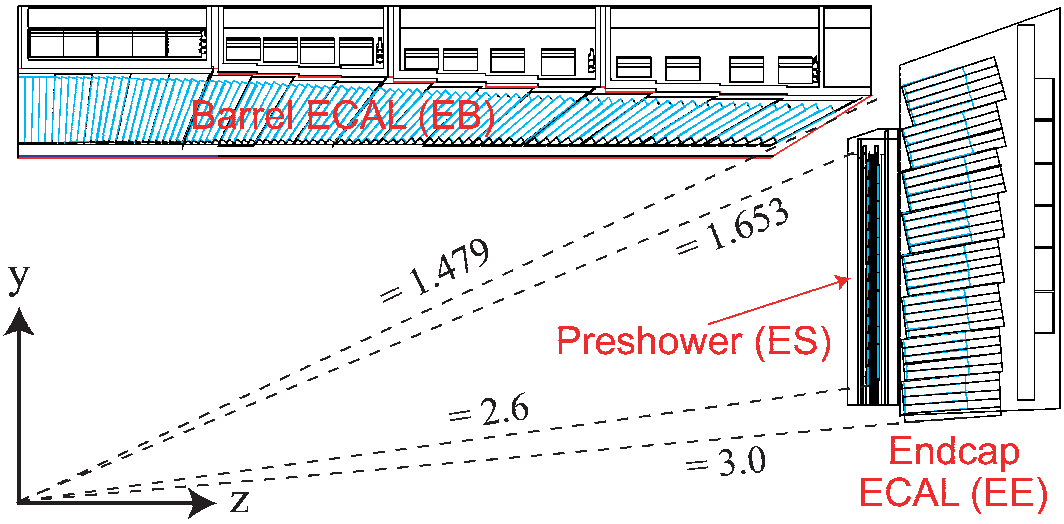

Figure 3.6: Layout of the ECAL detector [51]

.

interaction point.

The EE covers the pseudorapidity region $|\eta| \sim 1.5 - 3.0$. Each EE crystal covers 28.6×28.6 mm^2 at the front face and 30×30 mm^2 at the back. The length of each EE crystal is 22 cm, equivalent to $24.7X_0$. The distance of EE crystals to the interaction point measured from their faces is 3.14 m.

Each end cap has a preshower detector (ES) in front covering $|\eta| \sim 1.6 - 2.6$. The purpose of the preshower detector is to detect π^0's, to help electron identification, and to increase the precision of the position measurement of electrons and photons. The ES is a sampling calorimeter with 2 layers. The first layer is composed of lead radiators, and the second layer is composed of silicon strip sensors behind each radiator.

Two avalanche photo-diodes (APDs) each with a 5x5 mm^2 active area are attached to the rear face of each EB crystal. For each EE crystal, one vacuum phototriode(VPT) is attached instead.

The energy resolution of ECAL can be parametrized as

$$\left(\frac{\sigma}{E}\right)^2 \approx \left(\frac{N}{E}\right)^2 + \left(\frac{S}{\sqrt{E}}\right)^2 + C^2 \tag{3.2}$$

where N is the electronic noise term, S the stochastic term, and C the constant term. The ECAL supermodule energy resolution was measured in a test beam and gave $N = 124\ MeV$, $S = 3.63\%$ and $C = 0.26\%$, where the data was obtained with a 20×20 mm^2 trigger [51].

3.2.4 Hadron Calorimeter (HCAL)

The CMS Hadronic Calorimeter (HCAL) is a sampling calorimeter made of alternating layers of brass and plastic scintillator plates. The total energy is the energy deposited in the sampling layers from ionization which is converted to an electrical signal and then digitized. HCAL will help identify quarks and gluons by detecting jets. It will also complement the identification of electrons, photons and muons. HCAL plays a crucial role in the identification of neutrinos by way of missing energy.

HCAL is located behind ECAL with the HCAL barrel (HB) and HCAL endcap (HE) subdetectors. HB covers up to $|\eta| = 1.4$, has a length of 9 m and it extends from 1.8 m to 2.9 m in the radial direction. HE covers the region

from $|\eta| = 1.3$ to $|\eta| = 3.0$ and its inner and outer radii are 0.4 m and 3 m respectively.

The blue light produced in the scintillators are wavelength shifted to green by wavelength shifting (WLS) fibers embedded in the scintillator tile grooves. The light collected from all the tiles of a tower are channeled to Hybrid Photo Diode (HPD) photo-detectors that convert the light to electrical signals and then amplified. The channeling is done by clear fibers into the same pixel of an HPD. HPDs are capable of operating at high magnetic fields (up to 4 Tesla) perpendicular to the surface of the HPD.Clearly, all the front-end electronics must be able to operate at high CMS magnetic fields and high neutron fluences ($\sim 10^{11}$ cm^{-2} [52]). In the central region, the thickness of the HB corresponds to 5 interaction lengths [2] ($\sim 5\lambda_I$) which is not enough for full hadron shower containment. Because of this, a tail catcher (designated the Hadronic Outer (HO) calorimeter) is placed behind HB outside the magnetic coil extending to $|\eta| = 1.26$. With the inclusion of HO, the total depth of HCAL becomes $\geq 11\lambda$ for $|eta| < 1.26$.

HCAL is a non-compensating calorimeter so the response to hadrons compared to electrons is not a linear function of the incident particle energy. For HCAL the ratio of conversion efficiency of electromagnetic to hadronic energy yielding a visible signal is found to be $e/h = 1.41$, for the incident particle

[2] λ_I is the interaction length defined to be the mean distance a hadron traverses without suffering a nuclear interaction [49].

energies of above 10 GeV.

The performance of the combined EB+HB system is measured in test beams. The latest test-beam data in 2006 showed that the energy resolution of the combined EB+HB system for beam momenta in 2-300 GeV/c range, can be parametrized as

$$(\frac{\sigma}{E})^2 = (\frac{0.71}{E})^2 + (\frac{0.97}{\sqrt{E}})^2 + 0.08^2 \tag{3.3}$$

when both EB and HB are calibrated by 50 GeV electrons [50]. The first term represents the electronic noise which dominates the energy resolution at low energies. The second term is the stochastic term which is determined by the statistical fluctuations in the shower development. The last term is the a that depends on the degree of non-compensation [49].

Detection in the range $|\eta| = 2.9 - 5$ is provided by the Hadron Forward (HF) calorimeter which is optimized for measuring high energy jets. HB, HE and HF together provides hermetic coverage which is especially important for missing E_T measurements. HF calorimeter modules are at a distance of 11.15 m from the interaction point and has an outer radius of 1.3 m with a cylindrical hole at its center to accommodate the beam pipe. Each HF module consists of 18 wedges, each wedge covering a 20^o azimuthal angle. HF is segmented into 13 η-towers with $\Delta\eta \sim 0.175$, except for the first and last towers, $\Delta\eta = 0.111$ and $\Delta\eta = 0.302$, respectively. In the ϕ direction, each tower subtends 10^o, except the last two towers, which cover 20^o. HF will receive a high radiation dose

about 0.1 GRad/year [53] which was the main design constraint. HF utilizes radiation-hard quartz fibers (fused-silica core and polymer hard-clad) as the active medium, and steel absorbers, composed of 5 mm thick grooved plates for the absorber. The 0.6 mm diameter quartz fibers are placed in the grooves. The quartz fibers of HF are not projective, but are parallel to the beam line. Signal generation in HF is based on Cherenkov radiation that is produced in the quartz fibers when the charged particles in the electromagnetic component of the showers exceed the corresponding Cherenkov thresholds [54]. Charged hadrons are detected mainly through π^0 production. The produced light is guided to photomultipliers by the fibers. To compensate the different responses for electrons and pions, HF uses two different sets of fibers with different lengths, which are read-out separately. *Long* (165 cm) and *short* (143 cm) quartz fibers run through HF with a 5 mm separation. The long fiber extend to the front face of the detector, while the short fibers end 22 cm before the front face. This distance is larger than the depth of electromagnetic showers. Photomultipliers are used since HF lies outside the strong magnetic field of CMS. Use of long and short fibers, which are readout separately, makes it possible to distinguish electromagnetic and hadronic showers in HF.

The HF energy resolution is parametrized by stochastic and constant terms determined in test beams. When the long and short fiber sections are used, the stochastic and constant terms for the electromagnetic energy resolution are 198%

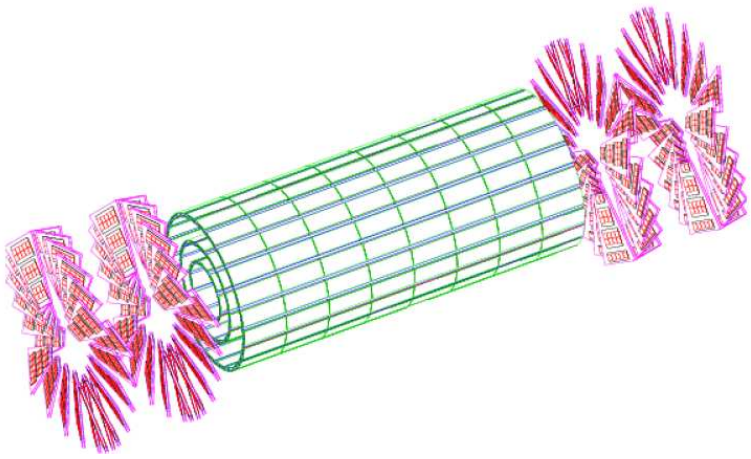

Figure 3.7: Layout of the pixel detector [55].

and ∼9% respectively, and 280% and ∼11% for the hadronic energy resolution [53]. Photoelectron statistics of the photomultiplier dominates the electromagnetic energy resolution, and π^0 fluctuations dominate the hadronic.

Further details of HCAL can be found in HCAL TDR [52].

3.2.5 The Tracker

The CMS components dedicated to track and vertex finding lie in the innermost part of the CMS detector. The tracking system is made up of highly segmented silicon pixel and silicon strip detectors that determine the momenta, position, and decay points of the charged particles from the ionization they produce along their paths. The pixel detector has a spatial resolution of about 15 μm. The tracker system consists of a single detector in the barrel and two in the endcaps. In the barrel part, there are three pixel layers and ten silicon strip

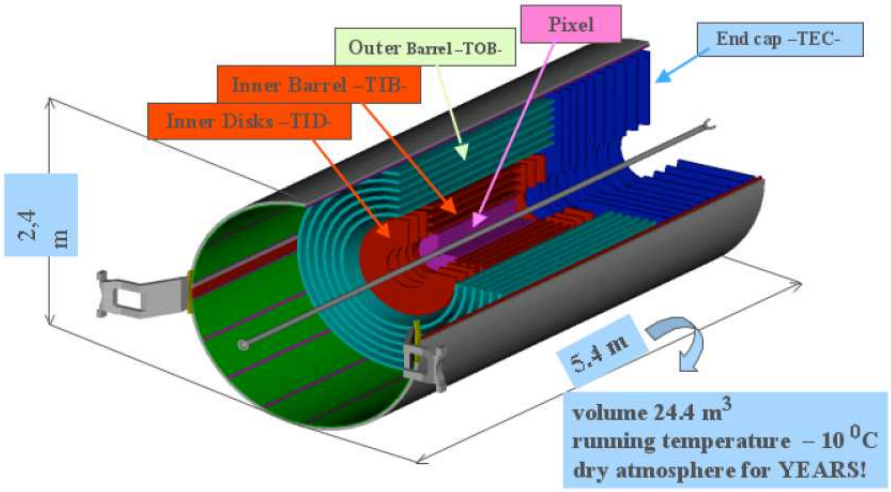

Figure 3.8: Layout of the CMS tracking detectors [56].

layers. Four of the 10 silicon strip layers makes the Inner Barrel(TIB) and 6 of them makes the Outer Barrel(TOB). In the endcaps, there are two pixel layers and three inner disk (TID) and nine outer forward silicon disk detectors. The layout of pixel detector can be seen in Fig. 3.7 and the CMS tracking detectors can be seen in Fig. 3.8. The silicon strip modules in the endcaps (TEC) are assembled on carbon-fiber support wedges. The tracker covers up to $|\eta| = 2.5$. In total, there are 25000 silicon strip detectors that covers about 200 m^2 and the signal is read out by about 10 million electronic channels. The momentum resolution of the tracker is $\Delta P/P \sim [15(P_T/TeV) \oplus 0.5]\%$ for $|\eta| < 1.6$ and becomes $[60(P_T/TeV) \oplus 0.5]\%$ as η approaches 2.5.

More details of the tracking system can be found in [55].

3.2.6 Triggers

The LHC bunch crossing rate is 40 MHz. About 20 inelastic pp events are produced at each bunch crossing at the design luminosity of 10^{34} cm^{-2}s^{-1}. This produces ∼1 MB of data at each crossing. Only a small portion of the data can be kept since current storage capacity is limited to about ∼ 100 MB/s or about 100 crossings per second. Therefore, a Trigger and Data Acquisition(DAQ) system is required that selects the interesting data with a rejection factor of $\sim 10^6$. The CMS trigger system consists of a level-1 (L1) trigger followed by a high level trigger (HLT) performed completely at the software level. The total time needed for the L1 trigger to come to a decision to store or not to store the data is 3.2 μs. This is mainly determined by the time needed for a signal to be transferred from the front-end electronics to the L1 logic system, since the time needed for the trigger calculations is less than about 1 μs. The data waits in the pipe-line buffers for $3.2\mu s/25\ ns = 128$ bunch crossings before it is decided that it will be kept or not. The L1 trigger reduces the event rate to 100 kHz for the design luminosity.

The L1 trigger uses calorimeter, muon system, and global(combination) triggers, that combine the data from calorimeters and the muon system. The "trigger-primitive" objects (photons, electrons, muons and jets) are constructed using the detector systems. These objects are created only if the p_T or E_T are above some thresholds. Also, the sum E_T and missing E_T which are determined

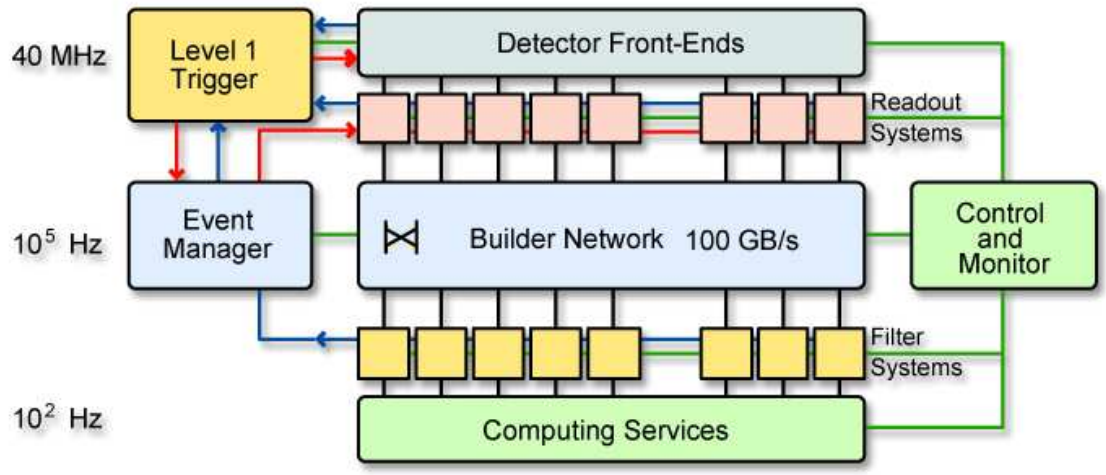

Figure 3.9: The CMS DAQ system. Taken from ptdr1 [60]

globally, are included as trigger primitive objects.

HLT reduces the 100 kHz L1 event rate to ∼100 Hz. All calculations beyond L1 are performed in a single filter farm of about 1000 dual-CPU computers. The HLT is highly flexible when it comes to changes in the decision trees. HLT first does partial event reconstruction using the calorimeters and the muon system. At this stage, it refines the objects created at L1. Then it combines the data from pixel and tracker for further rejection. The design of the HLT makes it possible that the offline reconstruction algorithms can be used in the HLT.

The schematics of the CMS trigger and DAQ system are displayed in Fig. 3.9. For further details, see the trigger CMS technical design reports [57, 58, 59].

CHAPTER 4

OPTIMIZATION OF ENERGY RECONSTRUCTION IN CMS USING TEST BEAM 2006 DATA

4.1 Introduction

In this chapter, the performance of the combined EB+HB system, as well as the optimization of the energy response and resolution are discussed. Section §4.2 summarizes test beam setup, beam clean-up and particle identification. Section §4.3 discusses energy reconstruction and the detector performance. Section §4.4 outlines the method for energy optimization, and Section §4.5 summarizes the results.

4.2 Test Beam Setup, Beam Clean-up and Particle Identification

The tests of the EB+HB calorimeter system were performed at the H2 beam line at the CERN SPS. The H2 beam line setup is displayed in Figure 4.1. The tests were done in high (10-350 GeV) and low-energy (1-9 GeV) beam configurations. In the beam line, there are 4 scintillator counters (S1-4) and 4 beam halo veto counters, which have a 7×7 cm hole in their center (BH1-4).

There are three Cerenkov counters (CK1-3) and two time-of-flight (TOF1-2) counters dedicated to particle ID. Only CK2 and CK3 were used in the test beam experiment. CK2 was filled with CO_2 and CK3 was filled with Freon 134a gas. As can be seen from the figure, there are several wire chambers in various locations in the beam line. Just behind HB1 there are 8 muon veto counters (VM1-8) and far behind the calorimeters there are two muon veto detectors, namely muon veto front (VMF) and muon veto back (VMB), which is separated from VMF by a thick absorber to achieve better muon identification.

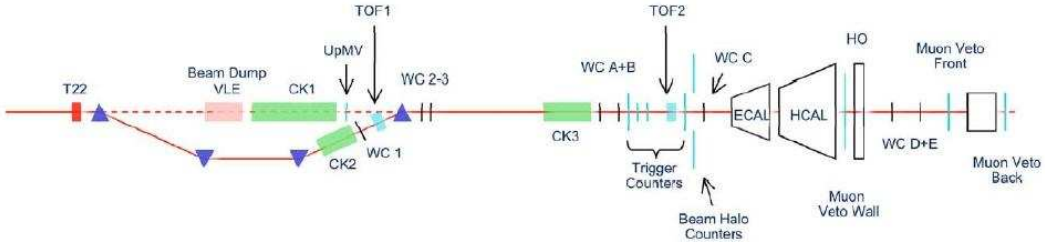

Figure 4.1: Layout of the testbeam line at H2.

The HCAL part of the calorimeter system consisted of two HB wedges(HB1 and HB2) corresponding to 8 segments covering 40 degrees in azimuth, four HE segments covering about 20 degrees in azimuth, and the Outer Barrel Calorimeter HO. The ECAL part used in the test beam is one of the 36 supermodules, namely SM9. Both ECAL and HCAL detectors were equipped with the final CMS production electronics. The entire calorimeter system was placed on a rotatable table whose pivot mimics the interaction point at LHC. The calorimeters

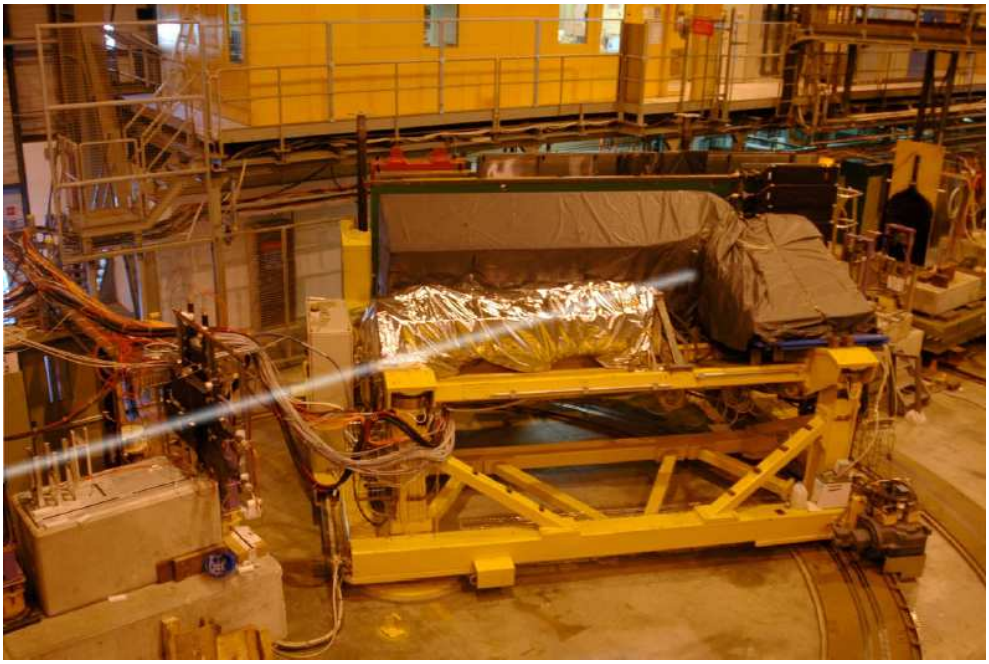

Figure 4.2: EB,HB and HE on the rotatable table. The white line represents the beam.

were placed on the rotatable table is shown in Figure 4.2.

To get a clean beam, only single-hit events in the scintillators S1, S2 and S4 were used in the trigger. Moreover, beam halo events and wide-angle secondaries were removed using the beam halo counters (BH1-4). VMB was used in later analysis to tag the muons in the high energy beam. To identify the muons in the low energy beam configuration (VLE), VMB, VMF and the muon veto counters (VM1-8) were utilized. At low beam momentum, electron contamination in the pion beam was dominant. Therefore, in addition to CK2, which was dedicated to electron tagging at VLE, CK3 also was used to remove the electrons in the

pion beam since CK3 could identify pions down to 4 or 5 GeV/c, depending on the pressure setting used during the data taking. Protons/antiprotons and kaons in the pion beam were identified using time-of-flight counters and CK3.

4.3 Energy Reconstruction and Detector Performance

HCAL and ECAL rechits, which is the energy in a cell of the calorimeter in units of GeV, were used for energy reconstruction. Six time-slices were used for HCAL signal reconstruction. ECAL uses phase dependent weights for the reconstruction [61]. Energy was collected in $\eta \times \phi = 4 \times 3$ towers for HB, while 3×2 towers were used for HO and 7×7 crystals were used for EB. Pedestals are measured and subtracted separately for each run.

Energies in EB and HB are displayed in a scatter plot for four different energies shown in Fig. 4.3. For these plots, EB energies are calibrated using electrons and HB energies are calibrated using 50 GeV pions.

For this study, EB was calibrated using 50 GeV electrons. There are two possible ways to calibrate the HB energy. One uses 50 GeV pions and the other electrons. When the calibrated EB and HB energies are combined, we obtain a more linear response in the first case, and better energy resolution but worse linearity in the second case. We chose to calibrate the HB with electrons as well. The HO energy scale calibration was optimized using the HO weight that gives the best HB+HO energy resolution at a beam momentum of 300 GeV/c. The

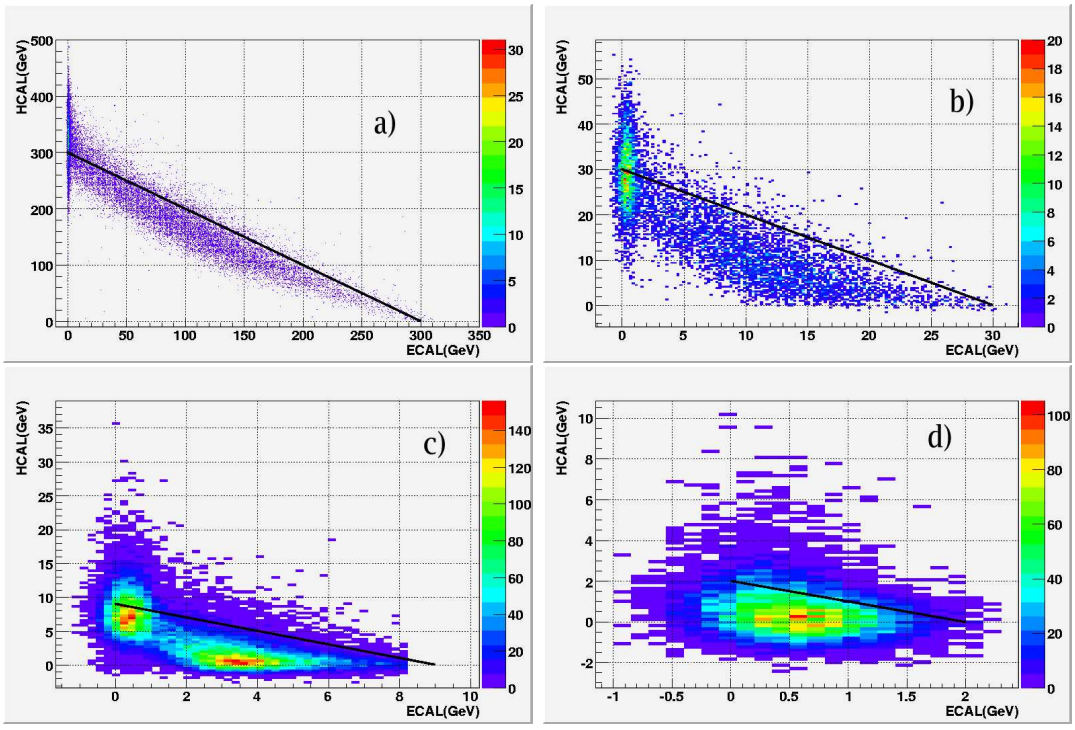

Figure 4.3: Plots of energy in EB vs energy in HB for a) 300, b) 30, c) 9 and d) 2 GeV beam momenta.

resulting responses for different particle species are displayed in Fig. 4.11.

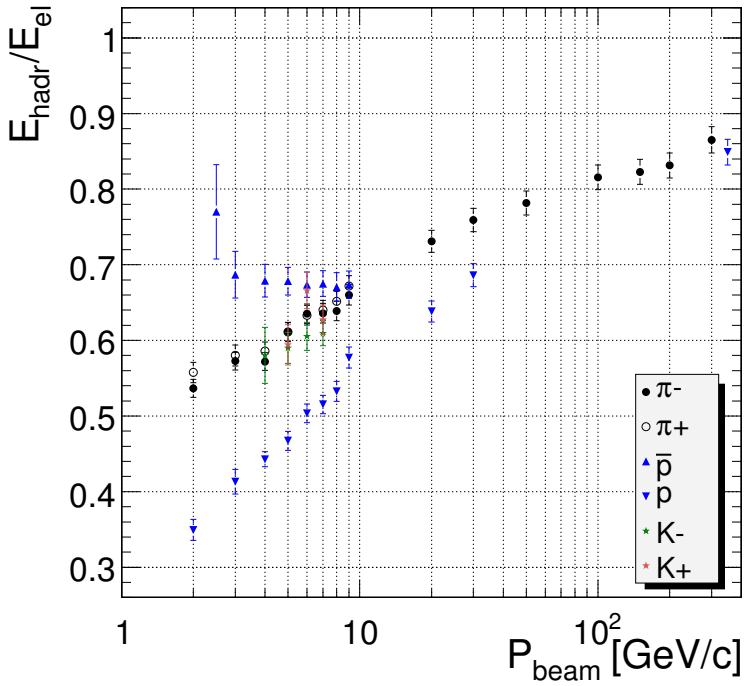

Figure 4.4: EB+HB performance for $\pi^{\pm}, p, \overline{p}$ and $K^{\pm}$ as a function of beam momentum [50].

It is seen that the response to antiprotons is higher than the pion and kaon energy response, and the response to protons, lower. The lower response of protons can be explained by baryon number conservation in the interaction of the protons with the detector material, and the "Leading Particle" effect. In showers induced by protons, a leading baryon is produced in the early stages of the shower development, unlike the showers induced by pions in which the leading particle is a neutral pion [49]. If the available energies (i.e. kinetic energies) are used the

difference between pions and protons/antiprotons is reduced to roughly $\sim 5\%$.

4.4 Optimization of Energy Reconstruction

The energy response to pions is not a linear function of the incident energy for non-compensating calorimeters. For these types of calorimeters the ratio of conversion efficiency of electromagnetic to hadronic energy producing a visible signal (e/h) is different from one. This is due to the fact that a significant fraction of the incident energy goes into exciting the sampling medium and the resulting nuclear break-up does not contribute to the measured signal. This results in a non-linear response since the fraction of electromagnetic energy in a hadronic shower f_0 increases with energy. In addition, the fluctuations in f_0 result in increased energy resolution. The e/h ratio is intrinsic to each type of calorimeter system. It can not be measured directly, but it can be inferred by measuring the π/e response.

The method used to correct and optimize the total energy using observed EB and HB energies and the known beam momentum is described below. Thresholds are applied on EB and HB energy clusters constructed from 7×7 EB crystals, 4×3 HB towers and 3×2 HO towers. If the energy in the cluster is less than the threshold for that event the energy of the cluster is set to zero. The thresholds, which are set at least 3σ away from the noise levels, are 0.8, 1.0 and 2.0 GeV for EB,HB and HO respectively. (The energy correction procedure was checked

by first applying the thresholds on individual HB towers and EB clusters. Very similar results were obtained for the sample means and rms values of the energy distributions).

The next step after applying thresholds is to parametrize the π/e for HB as a function of the mean HB energy using only events that deposit a minimum ionizing energy in EB ($E_{EB} < 1$ GeV). Down to ~ 10 GeV/c, π/e is:

$$\pi/e = \frac{1 + (e/h - 1)f_0}{e/h} \tag{4.1}$$

where f_0 is parametrized using Wigmans' function [80] given by $f_0 = 0.11log(P_0)$. The result of the fit, when the horizontal axis is the beam momentum, gave 1.41 for the value of e/h. Below ~ 10 GeV/c, π/e is represented through another logarithmic function, in the form $a\log(P_0)+b$. Further studies are planned to understand the physics behind logarithmic function describing the low energy(< 10 GeV/c) points.

Fig. 4.5 displays the π/e for HB as a function of the log of the mean HB energy. Fig. 4.6 shows the fit with the 4^{th} order polynomial. Down to ~ 8 GeV, the Wigmans' parametrization with $e/h' = 1.39$, and below 8 GeV, the logarithmic function $0.179\log(E_{HB}) + 0.413$ describe the data well. The e/h value determined from the fit in which the argument is P_0 and when it is E_{HB} are differentiated. In the latter case it is denoted by e/h'. The latter case is used for the analysis. Similarly, the Groom parametrization [81] instead of Wigmans' parametrization for f_0 yielded $e/h \approx 1.3$ in the same energy range.

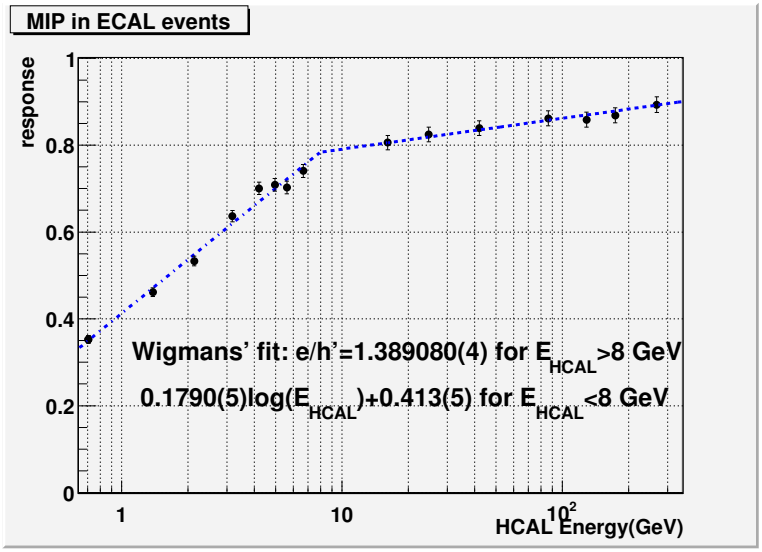

Figure 4.5: π/e vs $log < E_{HB} >$ for HB only. Above 8 GeV the data is parametrized using Wigmans' method with e/h'=1.39 and the data below 8 GeV is parametrized using a logarithmic function.

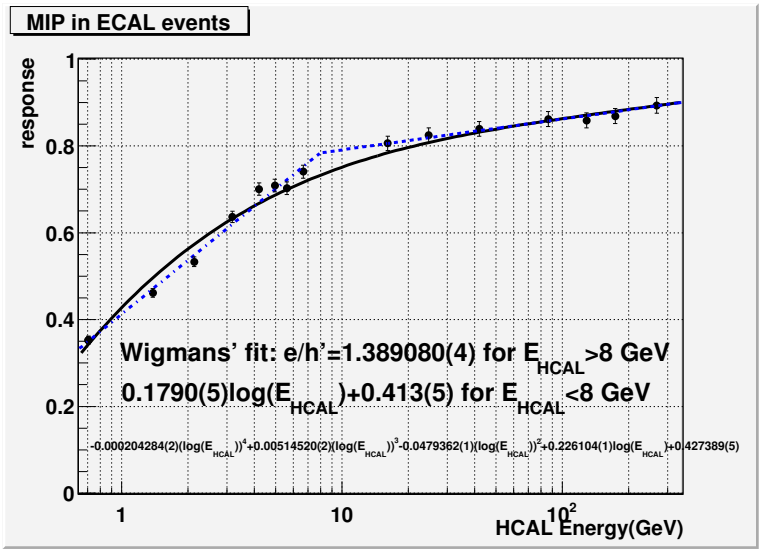

Figure 4.6: *π/e vs $log < E_{HB} >$ for HB only. Above 8 GeV the data is parametrized using Wigmans' method with e/h'=1.39 and the data below 8 GeV is parametrized using a logarithmic function. The data is also fitted to a 4^{th} order polynomial.*

The Wigmans function can be extrapolated up to very high energies without π/e becoming larger than one.

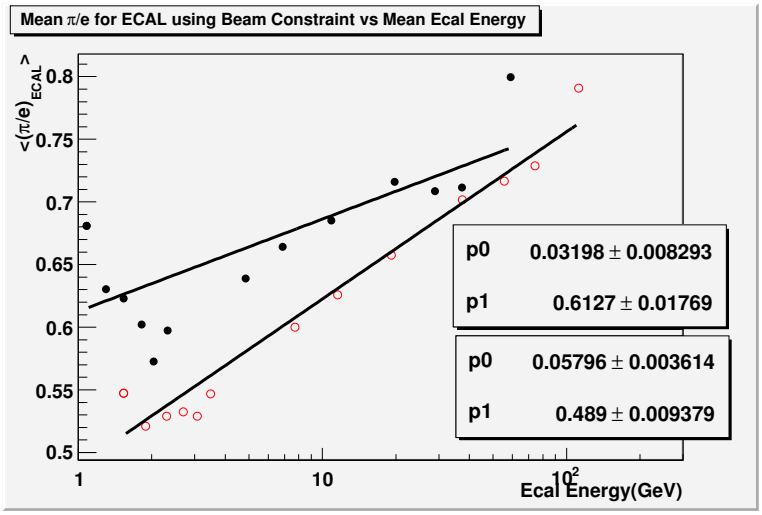

Figure 4.7: Measured $< (\pi/e)_{EB} >$ vs $log(E_{EB})$ with and without the cuts on E_{EB}. The linear fit to these data are also shown.

After correcting the HB energy points using the above function, the mean π/e for EB, $< (\pi/e)_{EB} >$ is estimated using the known beam momentum (P_0) as a function of mean observed EB energy (E_{EB}) for each beam momentum;

$$(\pi/e)_{EB} = \frac{E_{EB}}{P_0 - E^*_{HB}} \tag{4.2}$$

where E^*_{HB} is the corrected HB energy, $E_{HB}/(\pi/e)_{HB}$. The mean π/e for EB as a function of the logarithm of the observed EB energy shows a linear behavior (see Fig. 4.7). In this plot there are two different cases: the open circles represent the data calculated with the cuts $E_{EB} < 0.2P_0$ and $E_{EB} > 0.6P_0$ representing a more pure sample. The latter cut removes the events from charge exchange

reaction. The former cut removes the MIP in ECAL events including the tail of the MIP energy distribution from the bremsstrahlung. The filled circles are the data points calculated without these cuts. Notice that although both of the data points are well-represented by a logarithmic function, the fluctuations are less in the case when we select certain portion of the events with the E_{EB} cuts.

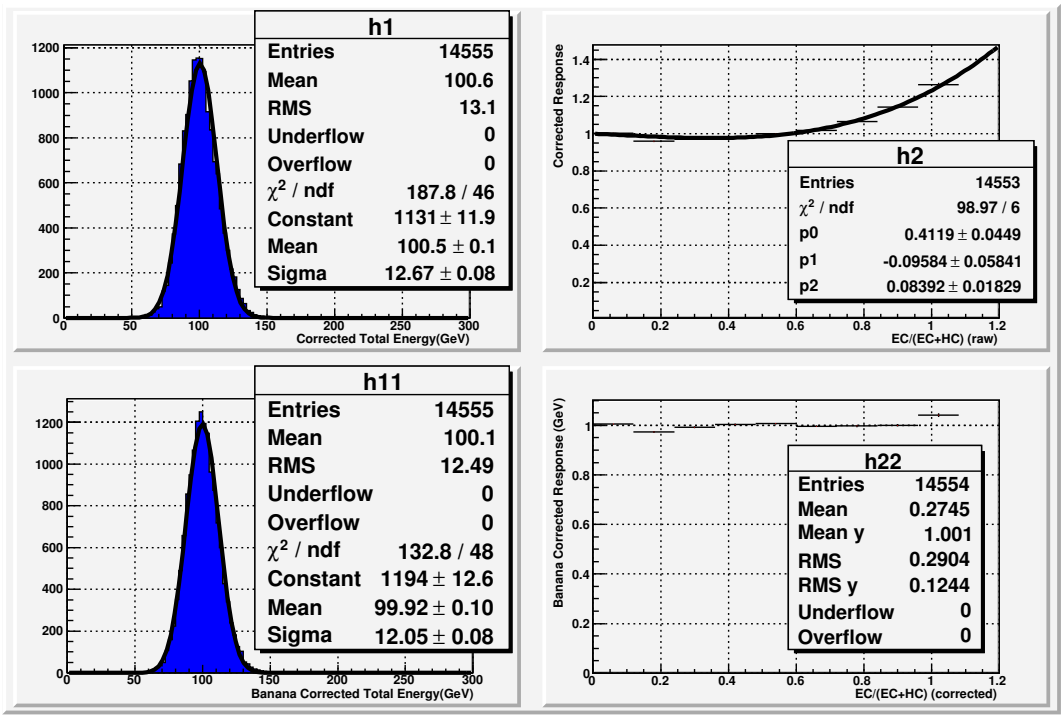

Figure 4.8: a) π/e corrected energy of EB+HB combined system. b) π/e corrected response of EB+HB combined system as a function of the EB energy fraction and the fitted cubic function in EB energy fraction. c) and d) are the energy and response corrected with the cubic function in b).

Therefore the cuts on E_{EB} for the analysis are used. The function representing $< (\pi/e)_{EB} >$ is of the form

$$< (\pi/e)_{EB} >= a_E log(E_{EB}) + b_E \tag{4.3}$$

The best fit parameters are $a_E = 0.057$ and $b_E = 0.49$. After correcting the EB energies using the above function, $E^*_{EB} = E_{EB}/(\pi/e)_{EB}$, we found that the π/e correction overestimates the energies for events with large EB energy fractions, $Z \equiv E_{EB}/(E_{EB} + E_{HB}) > 70\%$. This is expected since these events correspond to the cases when a pion shower in EB fluctuates largely to neutral particles. Also the response corresponding to an EB fraction of about 0.4 is lower due to the energy lost in the inactive region between the active elements of EB and HB. The π/e corrected EB+HB energy and response obtained from the 100 GeV/c pion beam as a function of EB fraction is displayed in Fig. 4.8 a) and b), respectively. This nonlinear response was fit to another correction function;

$$< \frac{E^*_{EB} + E^*_{HB}}{P_0} >= 0.4119Z^3 - 0.09584Z^2 - 0.08392Z + 1.00 \tag{4.4}$$

This function is used and as seen from Fig. 4.8 c) and d) the linearity is restored.

4.5 Results

The raw and corrected energy resolution using RMS and sample means are displayed in Fig. 4.9. The resolution is parametrized as;

$$\frac{\sigma}{E} = \frac{a}{\sqrt{E}} \oplus b \tag{4.5}$$

where a is the stochastic and b is the constant term, and the factors are combined in quadrature. The raw resolution of the EB+HB system is found to have 111% stochastic and 9% constant term. After the corrections, the stochastic term reduces to $\sim 94\%$ and the constant term becomes 8%. The corresponding resolution plot using the Gaussian fit values down to $P_0 = 6$ GeV/c are displayed in Fig. 4.10. The mean energy response and the response after all the corrections for each energy point are displayed in Fig. 4.11 and Fig. 4.12 for sample mean and Gaussian fit cases respectively. The corrected mean response remains in the range $\sim 96\% - 105\%$.

A simpler method can also be used to correct the energies in the test beam data by optimizing the EB and HB weights (α and β) in $E_{tot} = \alpha E_{EB} + \beta E_{HB}$. When $\alpha = 1.5$,$\beta = 1.2$ for beam momenta higher than 9 GeV/c and $\alpha = 1.9$,$\beta =$ 1.5 for beam momenta less than 9 GeV/c are used the stochastic term becomes $\sim$98% and the constant term becomes $\sim$11% and response is $\sim$100% for all energies.

It is important to note that the method presented above used the beam momenta. But in practice, when applying this method, only *observed* EB and HB cluster energies are needed.

For this method to be useful, it should be applicable to jets. However, directly applying the correction method determined from single particle energies on the jets is not possible. This is because jets are formed both from isolated as well

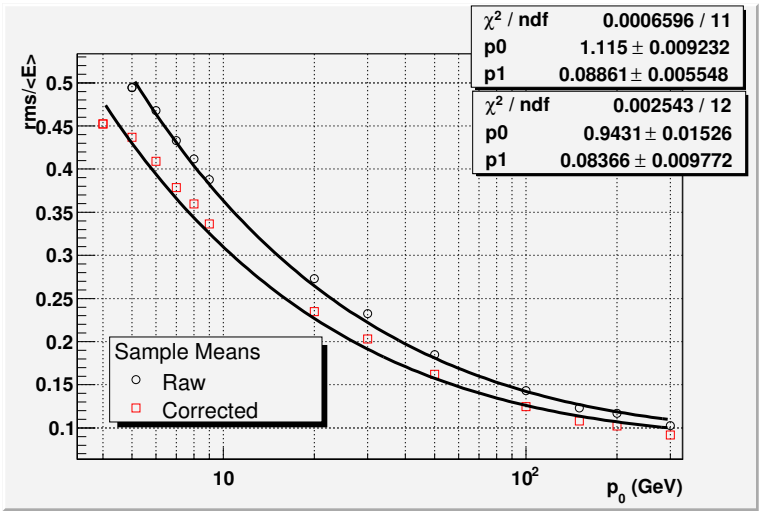

Figure 4.9: Raw and π/e corrected energy resolution curves determined from sample means and rms values.

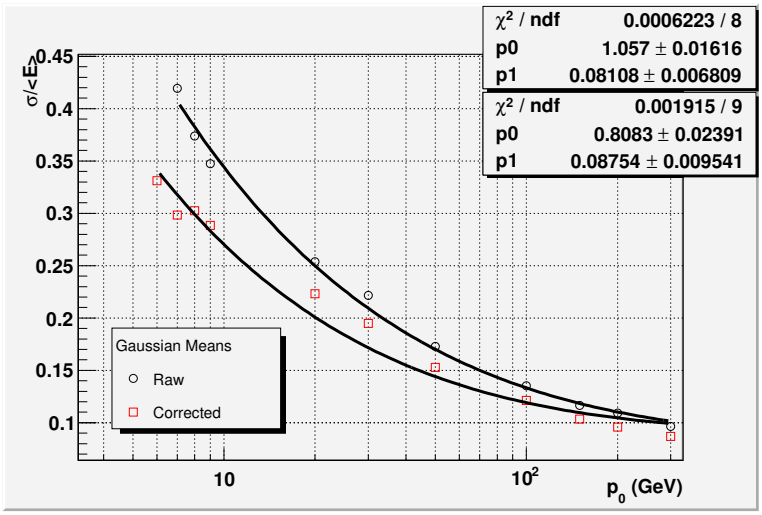

Figure 4.10: Raw and π/e corrected energy resolution curves determined from Gaussian mean and σ.

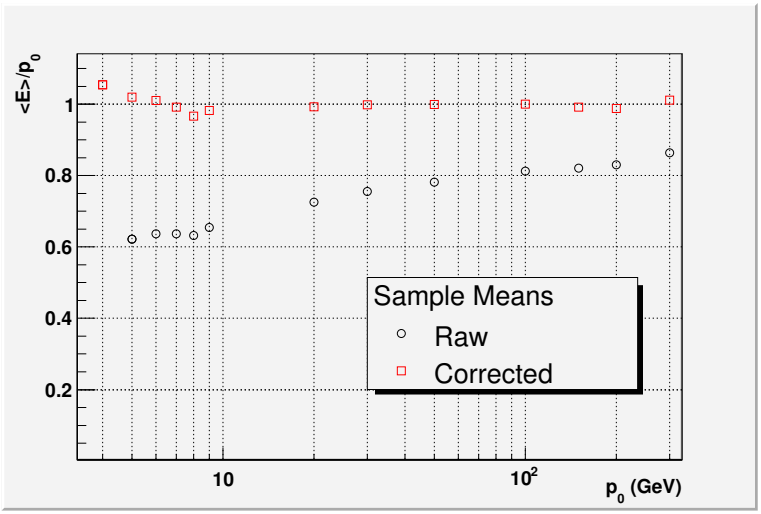

Figure 4.11: Raw and π/e corrected responses determined from sample means and rms values.

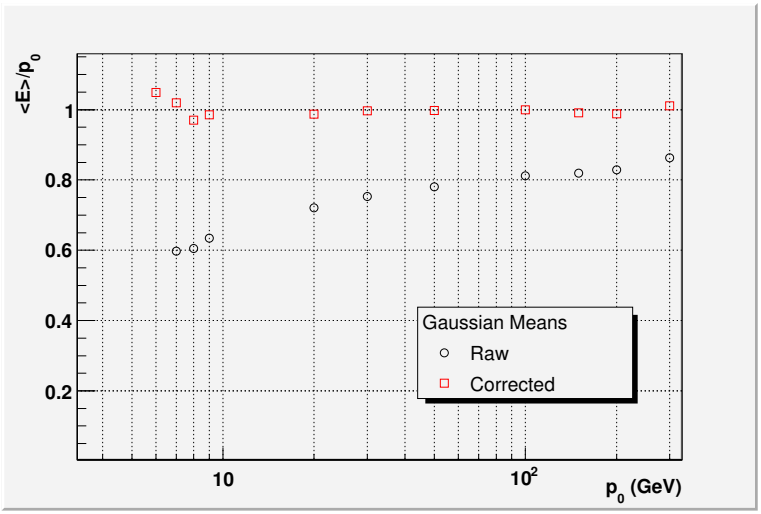

Figure 4.12: Raw and π/e corrected responses determined from Gaussian mean and σ.

as non-isolated objects. Jets are a mixture of electromagnetic and hadronic objects. If the photons from π^0's in a jet can be separated from the charged hadrons, then the corrections determined in this study can be applied on the charged hadrons and the jet then can be reconstructed with a better response and resolution. Separation of the photons and the charged hadrons is possible by using the tracker information. Also, particle flow methods might be useful in this direction, because it provides a way to distinguish all the particles in an event.

CHAPTER 5

SEARCH FOR A STANDARD MODEL HIGGS BOSON IN CMS VIA VECTOR BOSON FUSION IN THE $H \rightarrow WW \rightarrow l\nu l\nu$ CHANNEL

5.1 Introduction

One of the primary goals of the LHC experiments is to prove or disprove the existence of the Higgs boson. The LEP experiments set the lower limit on the Standard Model (SM) Higgs boson at 114.4 GeV for a 95% C.L. [62], and unitarity puts an upper limit of about 1 TeV. Even more constraining are the results of fits to precision electroweak measurements, which limit the mass of a Standard Model-like Higgs boson to be less than about 194 GeV [35] at 95% C.L. In extended Higgs sectors, there is often one scalar boson that resembles the Higgs boson of the Standard Model, and is responsible for electroweak symmetry-breaking. The mass of such a Higgs must also satisfy these constraints approximately. In the Minimal Supersymmetric extension of the Standard Model (MSSM), there is a more stringent bound coming from the internal constraints of the theory; the lightest Higgs boson must have a mass less than about 135 GeV.

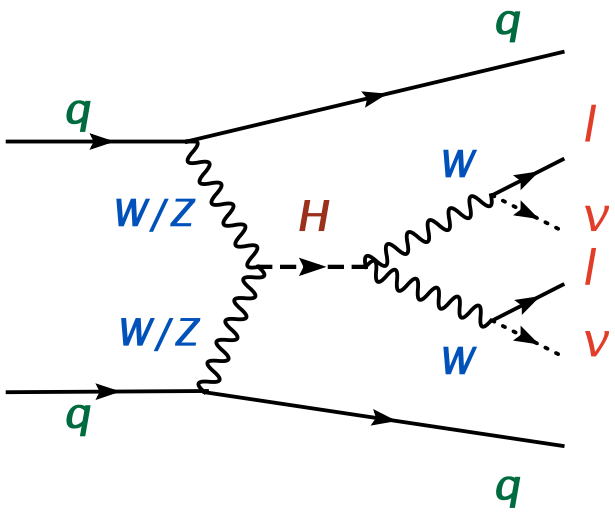

Figure 5.1: Feynman diagram for Higgs boson production through Vector Boson Fusion. The Higgs boson decays into W's which further decay into electron/muon-neutrino pairs.

For these reasons, we focus on the mass region $120 < m_H < 200$ GeV.

The two main decay modes of the Standard Model Higgs boson in this mass range are $H \to b\bar{b}$ and $H \to W^+W^-$. In the latter case, one of the W bosons may be off the mass shell. If the Higgs boson is heavier than about 135 GeV, the WW^* branching fraction will dominate, but it can be important for masses as low as 120 GeV. In this study, we consider the decay $H \to WW^*$ with the subsequent decay of the W-bosons to two charged leptons.

Higgs bosons may be produced in pp collisions when radiated off the virtual W-boson that is exchanged in the t-channel - this is called "Vector Boson Fusion" (VBF). The Feynman diagram for this process is shown in Fig. 5.1. This channel has good prospects for the discovery of a Standard Model Higgs boson, especially

if it is not too heavy because of the distinctive VBF topology which contains two jets with small angles with respect to the beam axis. Furthermore, when the Higgs decays to two W-bosons, the presence of the HWW vertex both in production and decay of the Higgs boson gives a relatively clean determination to the HWW coupling. Given the Higgs mass the Standard Model is completely determined, so that a measure of HWW coupling over-constrains the SM. This will be crucial to establishing the origin of electroweak symmetry breaking.

The VBF mechanism was proposed as a potential discovery channel several years ago [64]. The initial study of this channel for the CMS detector was carried out in 2002 [65], with a number of simplifications. The conclusion of this previous CMS study was that a convincing signal for a Higgs boson with a mass of 120 GeV would be observed with about 70 fb^{-1}. In the present study, we repeat the entire analysis in the mass range 120–200 GeV, using the latest simulation and reconstruction software for CMS in order to verify and improve the 2002 study. A similar study of this channel for the ATLAS detector was performed in 2004 using different generators and slightly different cuts [66]. We also studied the background and Higgs mass determination using the data.

The VBF process is characterized by two forward jets with modest transverse momentum, $E_T \approx m_W/2$, separated by a large rapidity difference. The Higgs boson signature is at low rapidity, with a pair of clean, isolated leptons and missing energy. The main backgrounds for this channel are the irreducible

continuum W^+W^- production, and $t\bar{t}$ in which both top quarks decay semi-leptonically. These backgrounds are particularly troublesome when there are extra jets, j, in the event, so we have taken particular care with the generation of W^+W^-jj and $t\bar{t}j$ events.

5.2 Event Generation

The signal process and the W^+W^-jj background have been simulated on the basis of a matrix-element calculation using MadGraph [67]. For the $t\bar{t}j$ background, we used the AlpGen [68] package which correctly simulates spin correlations. We simulated the parton showers using Pythia [69], within the CMKIN [70] framework. MadGraph and AlpGen calculations are made leading order (LO). The parton distribution functions used by MadGraph and AlpGen are CTEQ6L1 and CTEQ5L1 respectively. The minimum transverse momentum cut on jets is 15 GeV, and the pseudo-rapidity is limited to $|\eta| < 5$. We required a separation of any jet pair, namely, $\Delta R > 0.5$, where $\Delta R = \sqrt{(\Delta\eta)^2 + (\Delta\phi)^2}$.

Next-to-leading order (NLO) cross sections differ from LO cross sections by $\sim 30\%$ for a 120 GeV Higgs boson and $\sim 10\%$ for a 200 GeV Higgs boson [71]. However, since there are no NLO cross section calculations for the backgrounds, the LO cross sections are used consistently for both signal and background processes in this study. The cross sections are listed in Table 5.1. The 'electroweak'

(EW) part of the W^+W^-jj process is defined as the subsample with no α_s-dependent vertex in the diagrams, and the 'QCD' part is the rest of this process. Note that the EW part is topologically very similar to the signal and hence is almost irreducible.

Table 5.1: Production cross section for the signal(qqH) and the main backgrounds

Channel	cross section [pb]	WW branching ratio	$\sigma\times$BR [pb]
m_H=120	4.549	0.133	0.605
m_H=130	4.060	0.289	1.173
m_H=140	3.648	0.486	1.773
m_H=160	3.011	0.902	2.715
m_H=180	2.542	0.935	2.376
m_H=200	2.177	0.735	1.600
ttj	736.5	1.	736.5
WWjj QCD	43.6	1.	43.6
WWjj EW	0.933	1.	0.933

5.3 Detector Simulation and Event Reconstruction

We processed the generated events through the CMS detector simulation software (OSCAR_3_6_5) which is based on the Geant-4 simulation of the CMS detector. We simulated pile-up from out-of-time interactions representing the low-luminosity LHC running condition ($\sim 2 \times 10^{33}$ cm^{-2}s^{-1}). Subsequently, we processed digitized information (digis) was processed using the CMS event reconstruction software (ORCA 8.7.4). The events are analyzed using ExRoot which is an ORCA package to produce root trees out of CMS data samples.

5.3.1 Trigger

We refer to Ref. [72] for the planned trigger table. The inclusive electron trigger has an E_T-threshold of 26 GeV, which is too high for our purposes. Therefore we will augment this trigger with the di-electron trigger, which has a threshold of 12 GeV for both electrons. The p_T-threshold for the inclusive single muon trigger is 19 GeV, which is well suited to this analysis. Concerning the e-μ channel, we plan to use the e+μ di-lepton trigger, which will have a threshold of 10 GeV for each lepton. The efficiency for the L1+HLT trigger with respect to our offline cuts varies from about 95% to 99% based on Ref. [73]. This presents no significant effect at the current state of our analysis.

There will be lepton+jet triggers which should be very useful for this analysis if lower lepton thresholds are needed. However, since the details for these triggers are not available at this time, we have based our study solely on the leptonic triggers.

5.3.2 Lepton Reconstruction and Identification

We have used standard packages and selection criteria for muon and electron identification. Below, we describe our assessment of the identification efficiency.

5.3.2.1 Muons

Muon reconstruction starts with the reconstruction of positions of hits in DTs, CSCs and RPCs. Then the hits within each DT and CSC are matched forming segments. Then the seeds are constructed by matching and combining the segments. The seeds contain position, direction and estimated p_T. This seed is used as an initial guess for the track fit that uses the segments. The result is a *Stand Alone Muon*. Stand Alone Muon reconstruction uses only muon detectors.

The *Global Muon* reconstruction uses Stand Alone Muons as seeds. The *Global Muon* reconstruction takes muons detected in the muon chambers and extrapolates their tracks into the silicon detectors to pick up additional hits and so better define the kinematics. This extrapolation takes into account the energy lost by the muon as well as multiple Coulomb scattering at low p_T's. For a muon with $p_T = 100\ GeV$, the momentum resolution expected from a Stand Alone reconstruction is $\sim 12\%$ and from a Global Muon reconstruction is $\sim 1.5\%$. Expected muon reconstruction efficiency is $95 - 99\%$ for Global Muons [45].

In this study, we use the "global" muon reconstruction. Muons are found within $|\eta| < 2.4$. The overall muon reconstruction efficiency in this range is $\approx 95\%$ for $10 < p_T < 30$ GeV and 97% for $p_T > 30$ GeV.

5.3.2.2 Electrons

Electrons are reconstructed by combining super-clusters [74, 75] and Kalman tracks [76]. The track – super-cluster (SC) matching condition is $\Delta R < 0.15$. Such tracks should have at least four hits, and transverse momentum $p_T >$ 5 GeV. If several tracks satisfy these conditions, then the one having the least difference $|p_T - E_T|$ is taken. We reject the electron candidates if $E_T^{\rm SC} < 10$ GeV or $|\eta^{\rm SC}| > 2.0$. The probability for a generator level electron with $p_T > 10$ GeV and $|\eta| < 2.0$ to be reconstructed within $\Delta R < 0.2$ is $\sim$ 92–98% for $10 < p_T(gen) < 20$ GeV and $\sim$ 98–99% for $p_T > 20$ GeV. These reconstructed electrons are said to be identified if they satisfy the following conditions,

$$\frac{E_{\rm HCAL}}{E_{\rm ECAL}} < 0.05 \tag{5.1}$$

$$|\Delta\eta({\rm trk}, {\rm SC})| < 0.005 \tag{5.2}$$

$$\frac{E^{\rm SC}}{p^{\rm trk}} > 0.8 \tag{5.3}$$

$$|\frac{1}{E^{\rm SC}} - \frac{1}{p^{\rm trk}}| < 0.06 \tag{5.4}$$

The first of these conditions utilizes the fact that E_{HCAL}/E_{ECAL} is quite different for electromagnetic and hadronic objects, that is hadrons deposit large fraction of their energy in HCAL and electrons deposit all of their energy in ECAL. The ratio $E^{\rm SC}/p^{\rm trk}$ should be about 1 for electrons. But there are two different cases causing tails in both sides of 1. Single pions leave part of their energy in ECAL but the tracker detects its energy fully. This causes a lower

tail and hence the third condition is needed. The higher tail is caused by the electrons emitting bremsstrahlung radiation. In those cases the measured track momentum is underestimated while the ECAL sees all the energy.

π^0 component of jets do not leave any energy in the tracks but a lot in ECAL. Therefore, a cut on $E^{\rm SC}/p^{\rm trk}$ from above is needed to get rid of jets. This can be achieved in a less energy dependent way[77] with the cut defined in Eq. 5.4.

Electrons loose energy through bremsstrahlung that they would not be perfectly isolated if we only use the calorimeter information. Therefore an isolation variable is defined using the calorimeter as well as the tracker. The isolation variable is defined by taking the sum of the p_T of all the tracks (except the electron candidate) within a cone of $\Delta R^{\rm SC} < 0.2$, and dividing by the $E_T^{\rm SC}$. The tracks entering this sum must have at least four hits, $p_T > 0.9$ GeV, and $|z^{\rm trk} - z^e| < 0.4$ cm, where z is the position of the track along the beam line. We place the requirement that this isolation ratio be smaller than 0.2. The overall single electron efficiency for electron isolation and identification is $\approx 80\%$ for $10 < p_T < 30$ GeV and $\approx 90\%$ for $p_T > 30$ GeV. The electron fake rate per jet is $\approx 3\%$ for $10 < p_T^j < 30$ GeV and less than $\approx 0.1\%$ for $p_T^j > 120$ GeV calculated using the jets from W decay in the associated production and using the forward jets in the qqH sample.

5.3.3 Jet and Missing E_T Reconstruction and Correction

The cell-level thresholds are set at least 2σ above the noise level to remove the effects of calorimeter noise fluctuations in jet reconstruction. This is important since we are mainly dealing with quite low-p_T jets in the current study. Changing the thresholds is done by an implementation of the parameters in the EcalPlusHcalTower package in ORCA. The thresholds for the corresponding detector parts are as follows: HB> 0.7 GeV, HO> 0.85 GeV, HES> 0.9 GeV, HED> 0.9 GeV, EBSum> 0.2 GeV, EESum> 0.45 GeV and no HE thresholds and no extra thresholds on individual crystals (this is referred to as the Scheme A in CMS convention). It is found that HF is overestimated by about 15% so to have a smooth fit function for jet correction, the HF weight is set to 0.85.

We reconstructed the jets using the "Iterative Cone" algorithm, with a cone size of $\Delta R = 0.5$ and a cone seed E_T cut of 1 GeV. We removed the jets from an event if they match the reconstructed electrons within a cone of $\Delta R < 0.45$.

We calibrated the reconstructed jets using the qqH signal sample. Reconstructed jets are first matched to generator level jets within a cone of $\Delta R < 0.12$. We fit the jet response to second-order polynomials as a function of generator-level jet E_T for 20 different η regions covering $\eta = 0$ to $\eta = 4$ in bins of $\Delta\eta = 0.2$ (see Fig. 5.2). The difference between the corrected and uncorrected responses varies by 10% to 30% depending on the jet E_T and η values. When applying the correction to jets with $|\eta| > 4$, we used the correction parameters for the

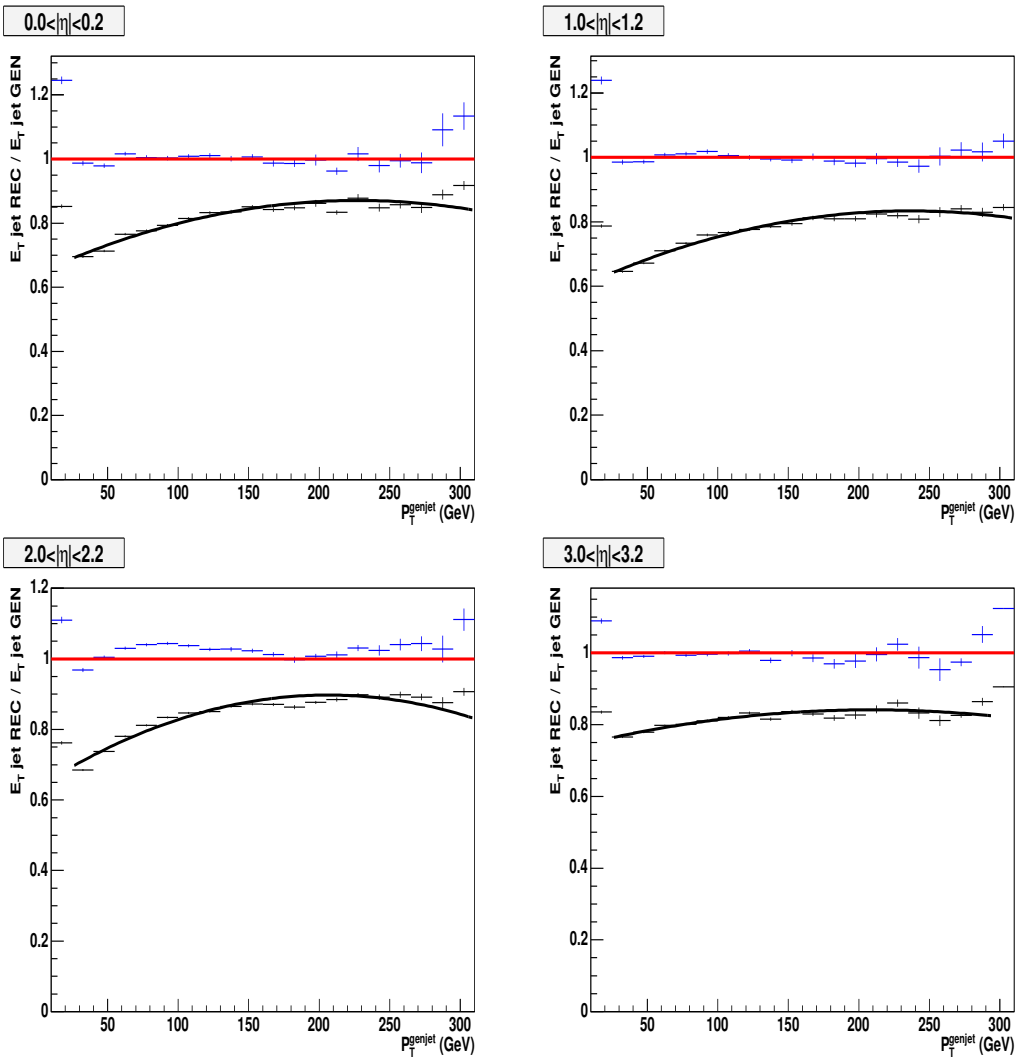

Figure 5.2: Uncorrected and corrected jet E_T response as a function of generator level jet E_T for four different η regions in 0.2 bins.

last interval $|\eta| = 3.8 - 4.0$. The polynomial extrapolation is unreliable beyond $p_T = 200$ GeV, so we fixed the corrections above 200 GeV to those obtained at 200 GeV. The correction procedure follows *ORCA MC jet correction* using a simpler polynomial form given by

$$p0[\eta] + p1[\eta] \times P_T(jet) + p2[\eta] \times P_T(jet)^2 \tag{5.5}$$

for $P_T(jet) < 200\ GeV$

$$p0[\eta] + p1[\eta] \times 200. + p2[\eta] \times 200^2 \tag{5.6}$$

for $P_T(jet) > 200\ GeV$. We calculated the jet correction function parameters using the signal sample with and without pile-up for this analysis. We used the one calculated from the sample with the pile-up events. The response to jets in the QCD di-jet sample is lower than the response to jets in the qqH sample. This produces different correction functions. However, in the current study, VBF tag jets are at high η and have at least $p_T > 30$ GeV and for this part of phase space the differences between responses (or equivalently, the jet correction functions) are very small.

In the analysis, we used missing $E_T(\not{E}_T)$ calculated from calorimeter hits.We corrected the $\not{E}_T$ using the sum of the E_T difference between the corrected and uncorrected jets for which the corrected jets have $E_T > 30$ GeV.

5.4 Event Selection

The strategy of the analysis is not complicated. We select events with two forward jets separated by a large rapidity difference, veto any event with additional central jets, and demand two energetic, isolated leptons in the central region. Finally, we apply additional cuts on the kinematics and the event topology.

5.4.1 Forward Jet Tagging

The jets are ordered in E_T after the corrections have been applied. The first two tag jets should be energetic, so we require $E_{T1} > 50$ GeV and $E_{T2} > 30$ GeV. Fig. 5.3 shows the rapidity separation $|\Delta\eta|$ between these two most energetic jets, for the signal(a) and the backgrounds(b-d). It is clear that the jets for signal events are well separated in rapidity, and we apply the cut $|\Delta\eta| > 4.2$. We also make sure that they fall in opposite hemispheres by requiring $\eta_1 \cdot \eta_2 < 0$.

5.4.2 Central Jet Veto

In the signal process, there is no color exchange between the protons, and consequently any additional jets will tend to be radiated in the forward direction. (Recall that we select only leptonic W's.) In contrast, the backgrounds will tend to have additional jets in the central region, especially the $t\bar{t}j$ process. We take advantage of this distinction by vetoing events with additional jets

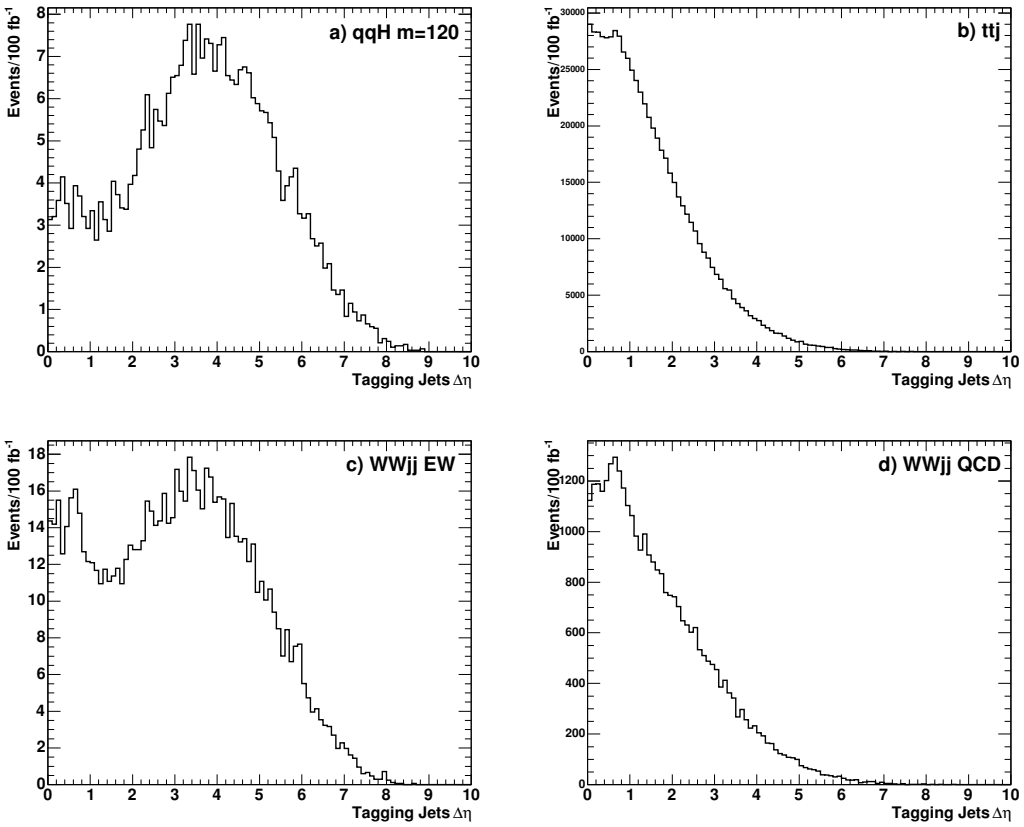

Figure 5.3: $\Delta\eta = |\eta_1 - \eta_2|$ distribution for the forward tag jets which have $E_{T1} > 50$ GeV and $E_{T2} > 30$ GeV for a) qqH, $m_H = 120$ GeV and backgrounds b) $t\bar{t}j$, c) EW W^+W^-jj and d) QCD W^+W^-jj. Note that the EW W^+W^-jj background is basically irreducible.

in the central region. In particular, we consider any jet with $E_{T3} > 20$ GeV and compute the rapidity with respect to the average of the two forward jets: $\eta_0 = \eta_3 - (\eta_1 + \eta_2)/2$. We veto the event if $|\eta_0| < 2$. See Fig. 5.4 for distributions of both signal and background. The probability to find a fake jet from pile-up events for low luminosity LHC running is shown in Fig. 5.5 as a function of the E_T threshold for the central jet veto. The fake rate is defined as the rate for pile-up jets satisfying the central jet veto condition in an event where there are no real jets satisfying those conditions. Therefore, the fake rate is just the rate of events mistakenly rejected due to pile-up. The loss of events for a E_T threshold of 20 GeV is only about 2%.

5.4.3 Lepton Kinematics

We require two opposite-sign leptons in an event. The most energetic lepton must have $p_{T1} > 20$ GeV, and the other, $p_{T2} > 10$ GeV. The p_T-threshold for the second lepton must be low since one of the two W's in the Higgs decay is off the mass shell for low Higgs masses. Fig. 5.6 shows the p_T spectra for electrons in the signal process ($m_H = 120$ GeV). We reject events with more than two leptons. The two leptons must be well separated from all jets with $\Delta R_{\ell j} > 0.7$.

In light of the thresholds for the electron triggers, we modified our p_T requirements slightly in the di-electron channel. An event is selected if it has two electrons which satisfy:

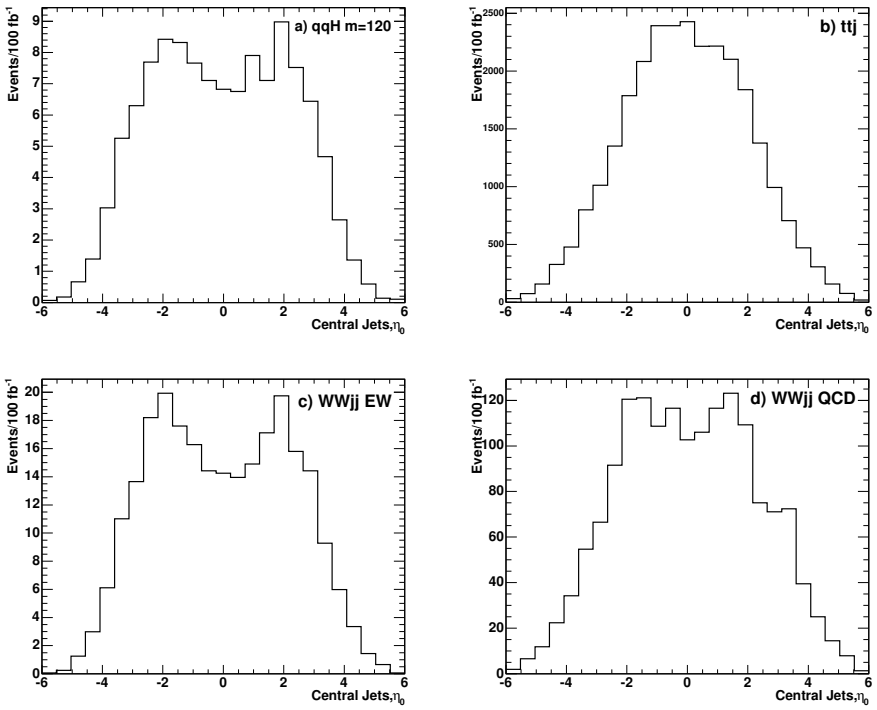

Figure 5.4: $\eta_0 = \eta_3 - (\eta_1 + \eta_2)/2$ for the third jet. η of the third jet with respect to the average of the two forward jets. For signal a) qqH, $m_H = 120$ GeV and backgrounds b) $t\bar{t}j$, c) EW W^+W^-jj and d) QCD W^+W^-jj.

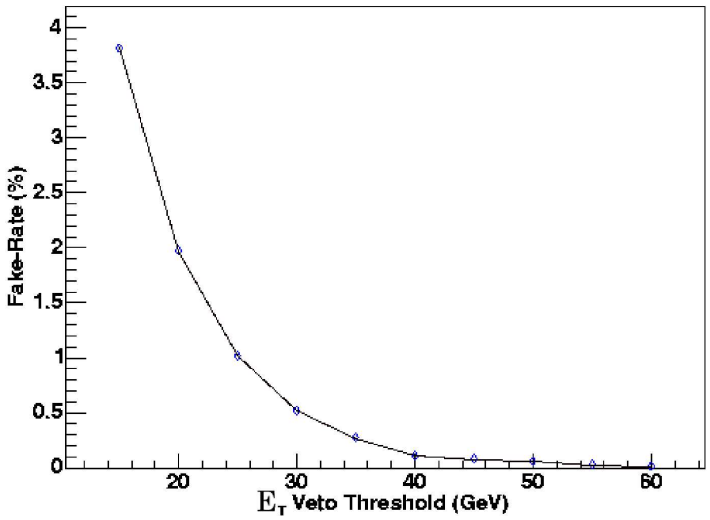

Figure 5.5: Fraction of fake central jets per event as a function of E_T veto threshold. A fake is defined as the probability to find at least one jet(due to pile-up) satisfying the central jet veto conditions, with no "real" jets satisfying the central jet veto condition in that event.

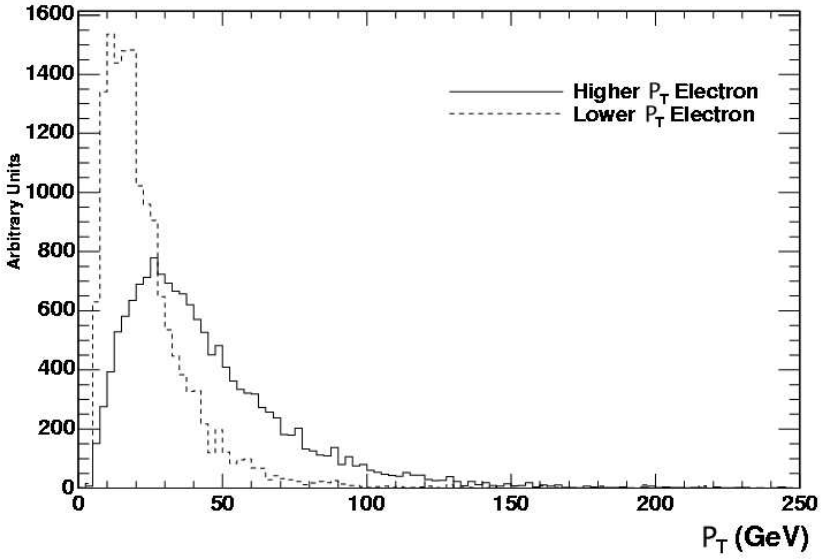

Figure 5.6: Electron E_T spectra, for the signal process when $m_H = 120$ GeV

$$(E_{T1} > 26 \text{ GeV AND } E_{T2} > 10 \text{ GeV})$$

$$\text{OR}$$

$$(E_{T1} > 20 \text{ GeV AND } E_{T2} > 12 \text{ GeV}) \ .$$

We find this has a minuscule impact on the acceptance for signal and background events, compared to the simple cuts $E_{T1} > 20$ GeV and $E_{T2} > 10$ GeV.

Since the leptons come from the W's that come from the centrally-produced Higgs boson, we require them to be central. If $\eta_{\rm hi}$ is the forward-tag jet having higher-rapidity, and $\eta_{\rm lo}$ is that of the lower-rapidity forward-tag jet, then our requirement can be written $\eta_{\rm lo} + 0.6 < \eta_\ell < \eta_{\rm hi} - 0.6$. This condition must be satisfied by both leptons. Fig. 5.7 shows the distributions of the related quantity, $\eta'_\ell = (\eta_\ell - (\eta_{J1} + \eta_{J2})/2) \times 4.2/\Delta\eta$. This quantity is sensitive to the η distribution of leptons with respect to the forward tag jets.

5.4.4 Further Kinematic Requirements

After the forward-jet tag, the central jet veto, and the lepton kinematics cuts, we are left with a sample which still has a large contamination from background processes. We can further reduce this contamination with some additional kinematic cuts.

First, we require the di-jet mass to be greater than 600 GeV (see Fig. 5.8). Next, we look at the overall p_T-balance in the event, by computing the vector sum of the transverse momenta of the two leading jets, the leptons, and the

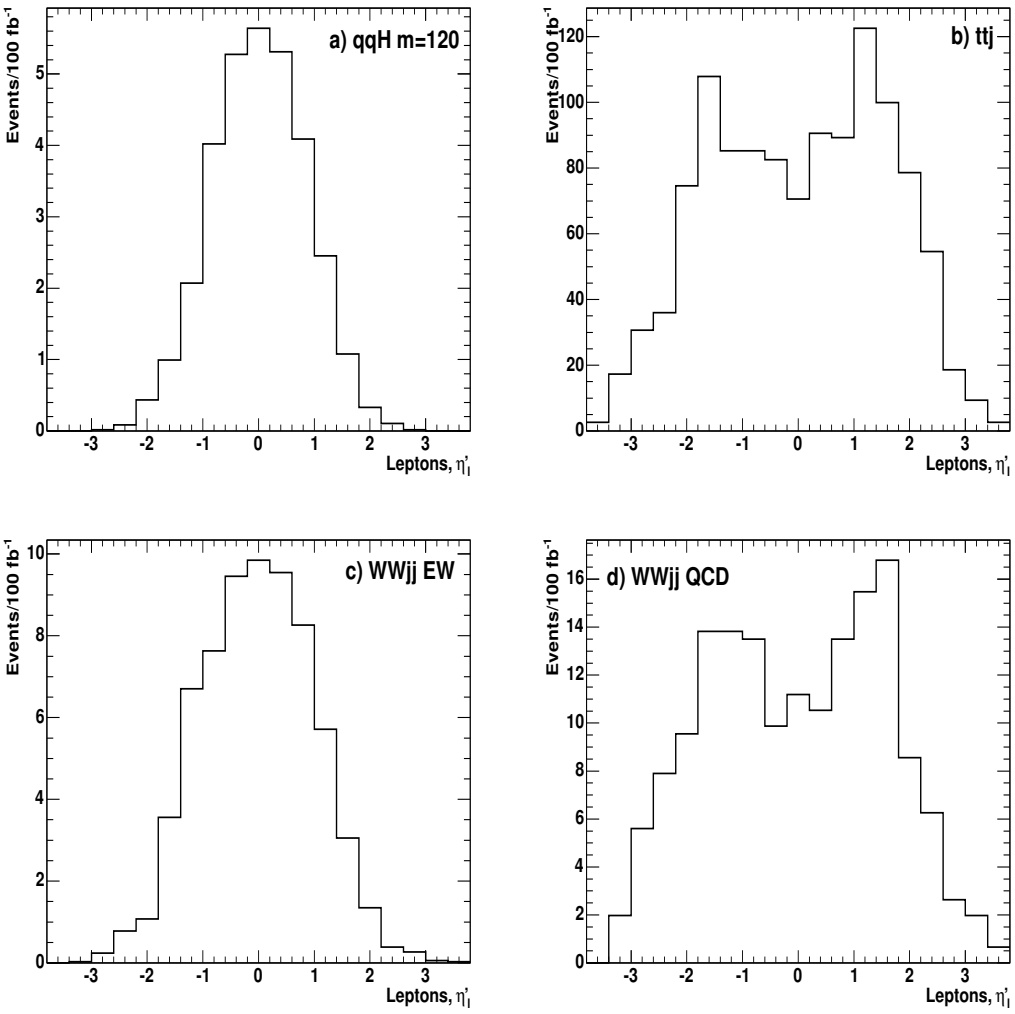

Figure 5.7: Centrality of the leptons, using the quantity η'_ℓ defined in the text for a) qqH, $m_H = 120$ GeV and backgrounds b) $t\bar{t}j$, c) EW W^+W^-jj and d) QCD W^+W^-jj.

missing energy. The magnitude of that sum should be less than 40 GeV (see Fig. 5.9).

When it comes to the leptons, we require a di-lepton mass $M_{\ell\ell} < 80$ GeV (see Fig. 5.10). This value is lower than the Z-mass, so that leptonic Z-decays do not affect the current analysis. A useful distinction arises in the relative azimuthal angle of the two leptons due to the spin-0 nature of the Higgs boson (see Fig. 5.11, 5.12). We take advantage of this discriminant and require $\Delta\phi < 2.4$ radians. Finally, we require that the "WW transverse-mass" be not too high when looking for Higgs bosons with mass below 150 GeV. The cut is that $M_{T,WW} < 125$ GeV, where $M_{T,WW} \equiv \sqrt{(\not{E}_T + E_{T,\ell\ell})^2 - (\vec{\not{E}}_T + \vec{P}_{T,\ell\ell})^2}$. See Fig. 5.13 and 5.14 for distributions of this quantity.

5.4.5 Additional Cuts

Additional cuts may be required for $bbjj$ and $\tau\tau jj$ backgrounds not pose a problem. The additional cuts $57.3\Delta\phi(\ell\ell, \not{E}_T) + 1.5p_T^{\text{Higgs}} > 180$ and $12 \times 57.3\Delta\phi(\ell\ell, \not{E}_T) + p_T^{\text{Higgs}} > 360$, and also $\not{E}_T > 30$ GeV if $p_T^{\text{Higgs}} < 50$ GeV, are imported from Ref. [64]. Here, p_T^{Higgs} is the vector sum of the transverse energy of tag jets. The distribution of signal events in the $\Delta\phi(\ell\ell, \not{E}_T)$-$p_T^{\text{Higgs}}$ plane is displayed in Fig. 5.15.

The Drell-Yan production of di-lepton pairs, $\gamma^* \to \ell^+\ell^-$, has a large cross section. In order to reduce this background sufficiently, we impose a di-lepton

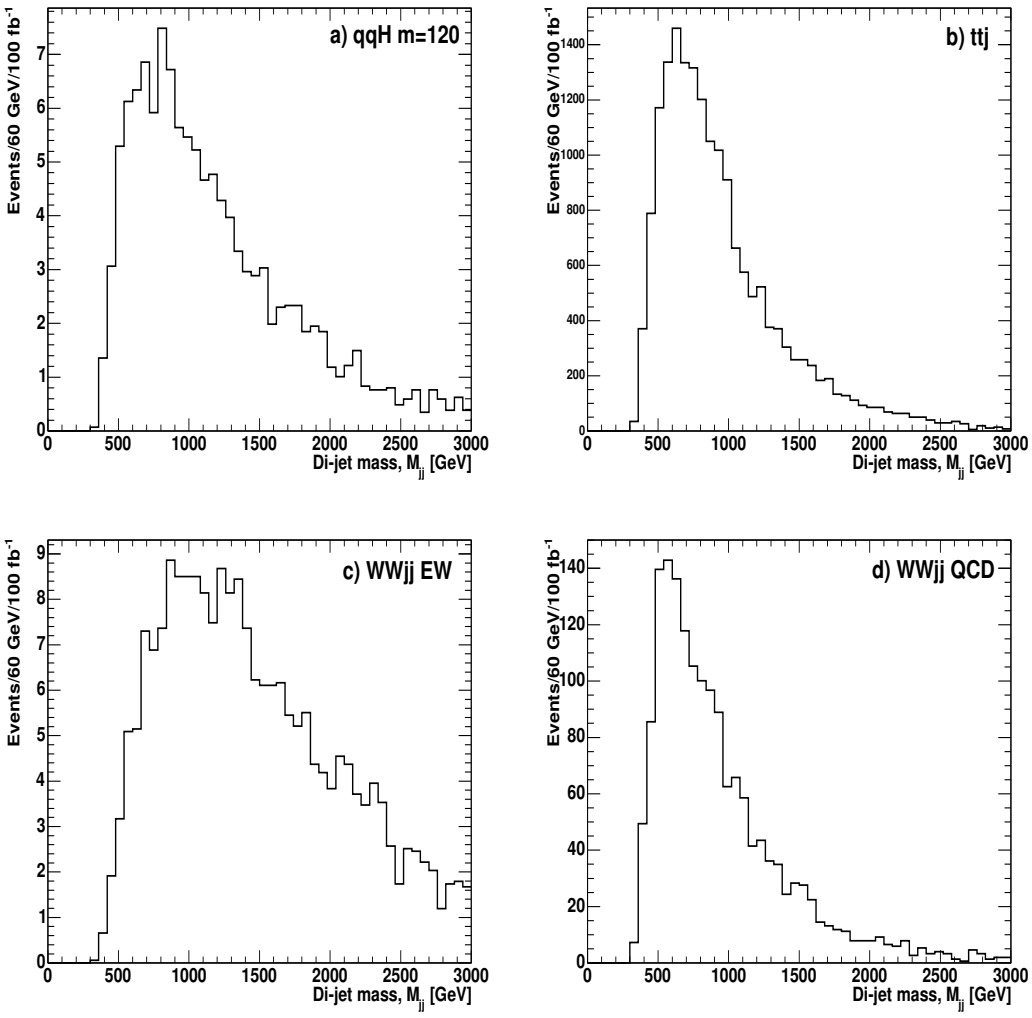

Figure 5.8: Invariant mass distributions for the two forward tag jets, for a) qqH, $m_H = 120$ GeV and backgrounds b) $t\bar{t}j$, c) EW W^+W^-jj and d) QCD W^+W^-jj.

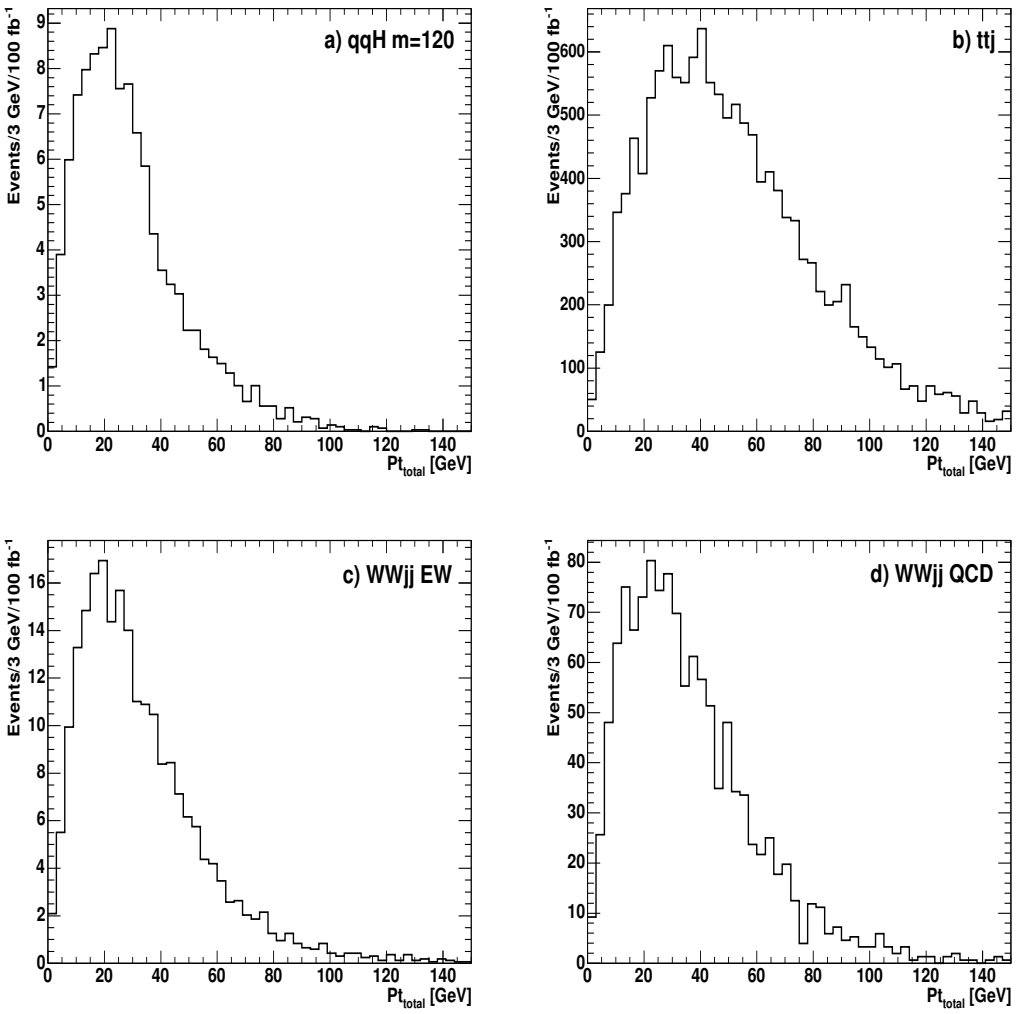

Figure 5.9: The overall p_T-balance in the event. for a) qqH, $m_H = 120$ GeV and backgrounds b) $t\bar{t}j$, c) EW W^+W^-jj and d) QCD W^+W^-jj.

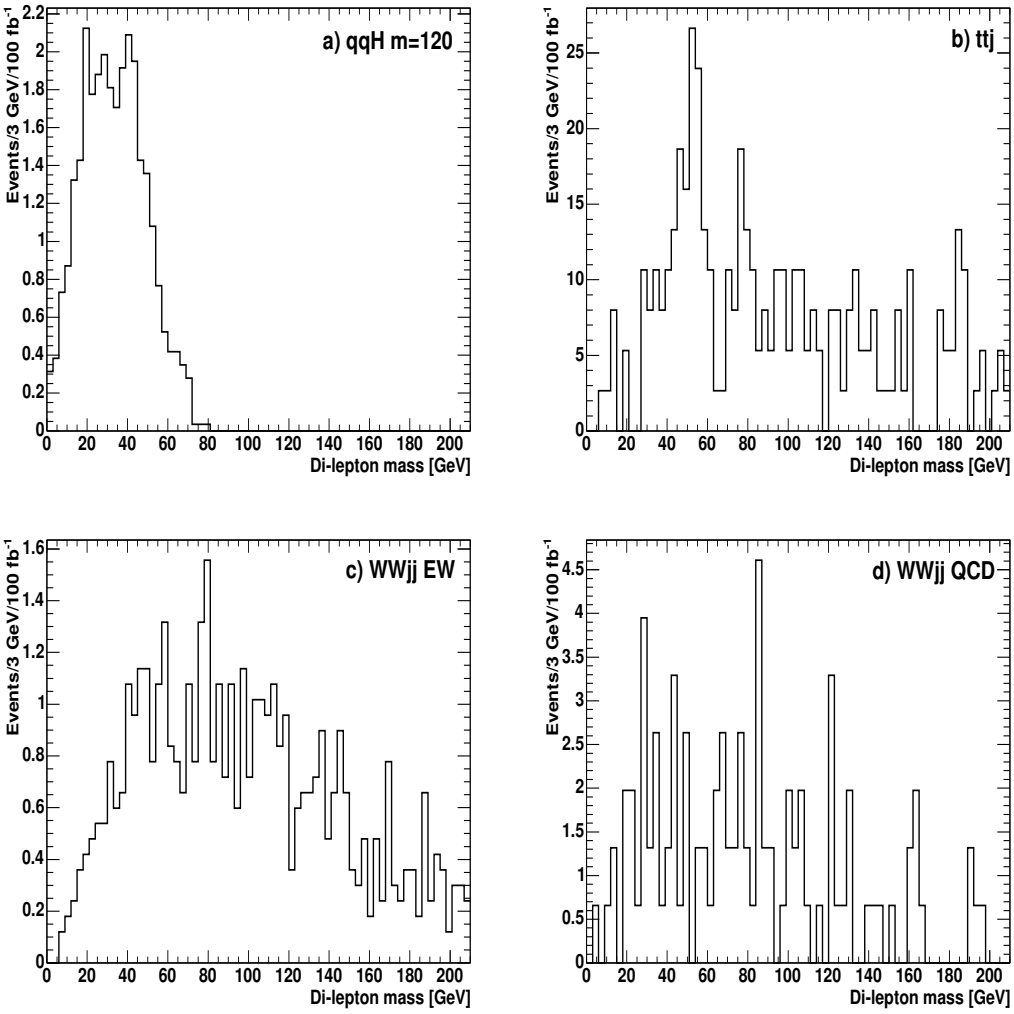

Figure 5.10: Di-lepton invariant mass distribution after jet and lepton cuts, for a) qqH, $m_H = 120$ GeV and backgrounds b) $t\bar{t}j$, c) EW W^+W^-jj and d) QCD W^+W^-jj.

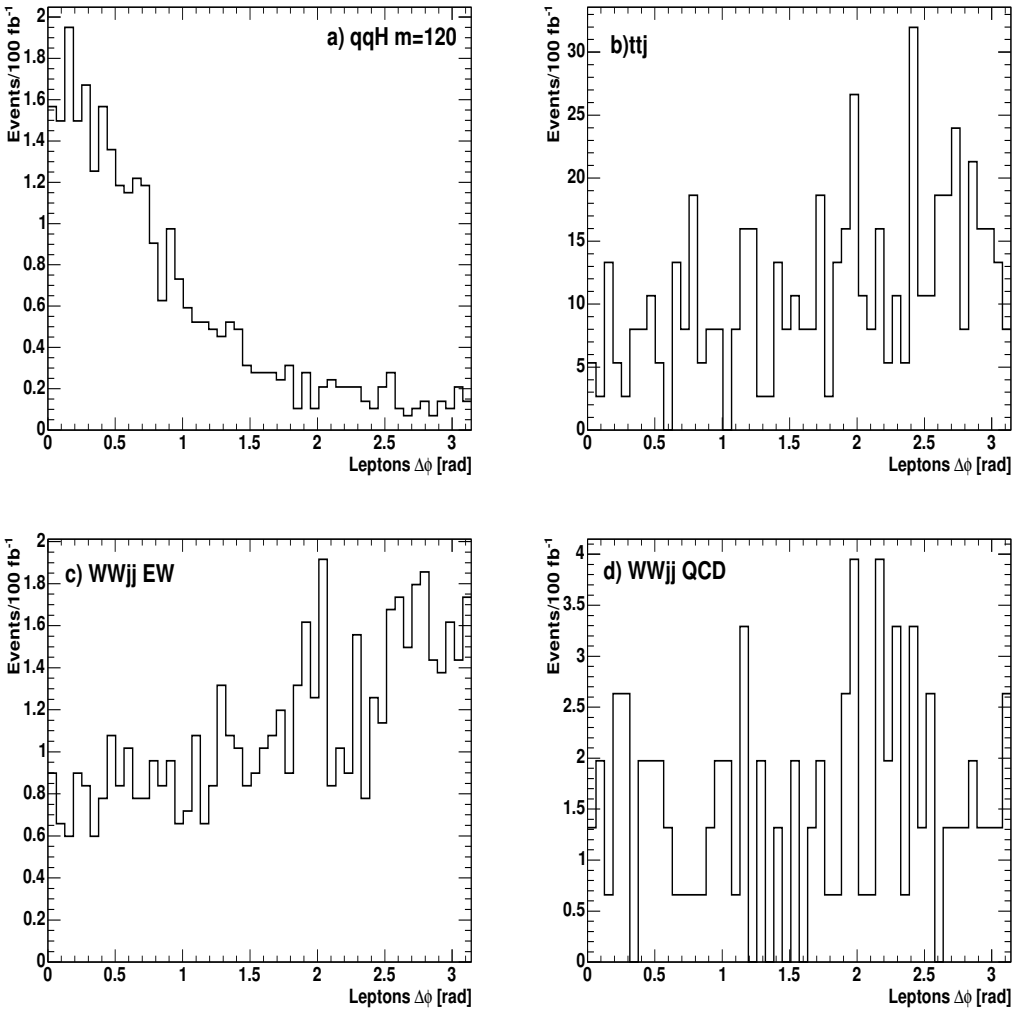

Figure 5.11: The distribution of the difference in azimuthal angle between the two leptons, $\Delta\phi$ after jet and lepton cuts, for a) signal events, qqH, $m_H = 120$ GeV and backgrounds b) $t\bar{t}j$, c) EW W^+W^-jj and d) QCD W^+W^-jj.

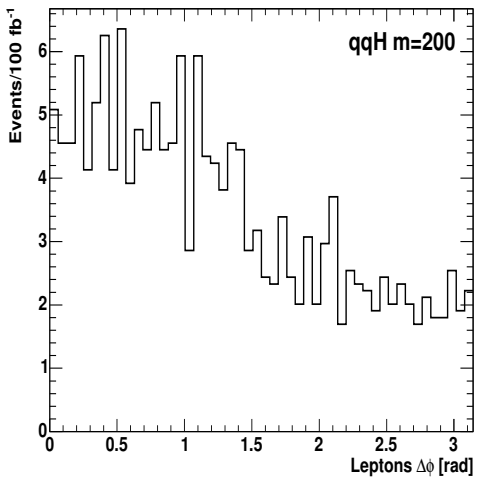

Figure 5.12: The $\Delta\phi$ distribution between the two leptons after jet and lepton cuts for qqH, $m_H = 200$ GeV

mass cut $M_{\ell\ell} > 10$ GeV and we require $\not{E}_T > 30$ GeV when the leptons have the same flavor (see Ref. [64]).

Finally, we impose the cut $\Delta\phi(\ell\ell,\not{E}_T) + \Delta\phi(\ell\ell) < 3$ radians, which increases the signal-to-background ratio. Fig. 5.16 shows distributions of this quantity. The resolution of the quantity $\Delta\phi(\ell\ell, \not{E}_T)$ is improved by the $\not{E}_T$ correction. After all the cuts, the additional backgrounds $bbjj$, $\tau\tau jj$ and $\gamma^* \rightarrow \ell^+\ell^-$ are only $< 1\%$ of the $t\bar{t}j$ and W^+W^-jj backgrounds [64]. The additional cuts imposed after transverse mass cut were determined for generator level analysis. Therefore, we did not include these cuts in the significance, background or mass estimation but their effects on the signal and other backgrounds are separately shown in Tables 4-6.

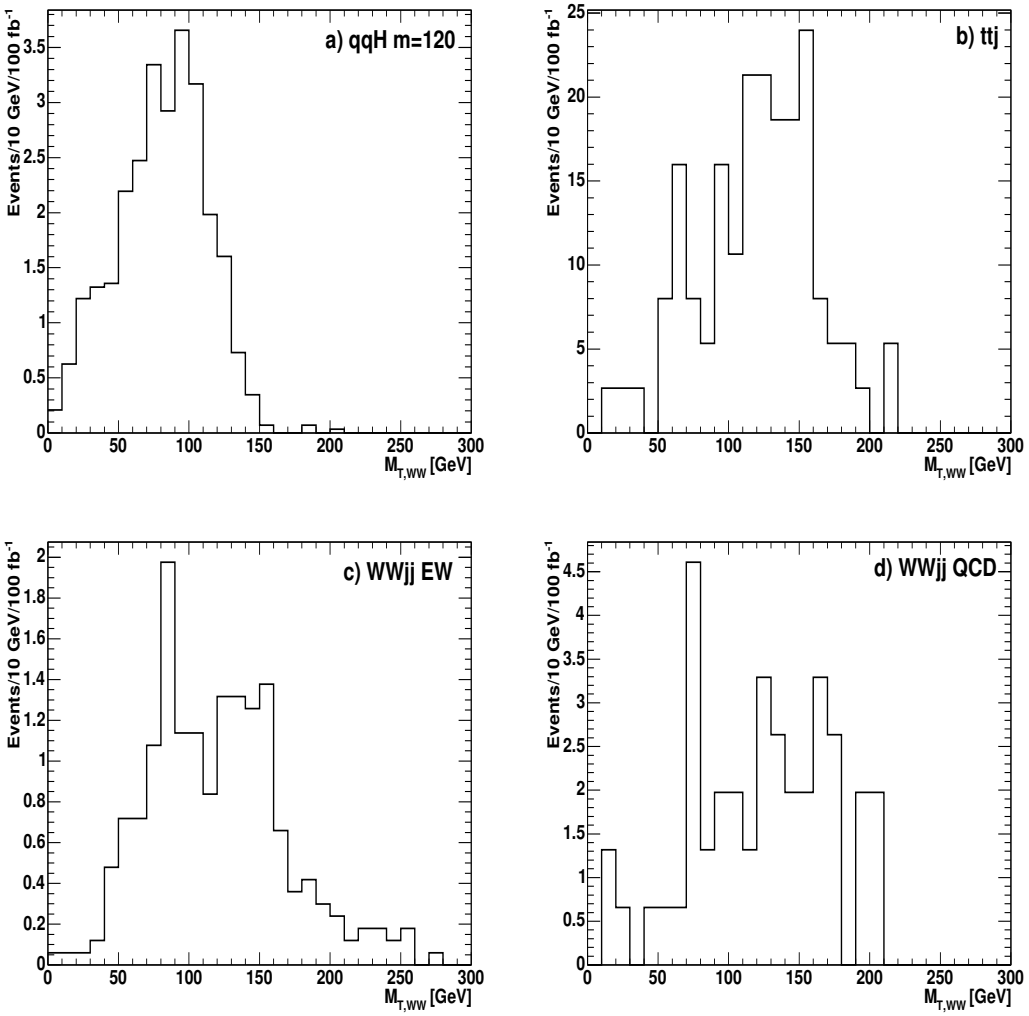

Figure 5.13: The transverse mass of the two W bosons, $M_{T,WW}$, for a) signal events, qqH, $m_H = 120$ GeV and backgrounds b) $t\bar{t}j$, c) EW W^+W^-jj and d) QCD W^+W^-jj.

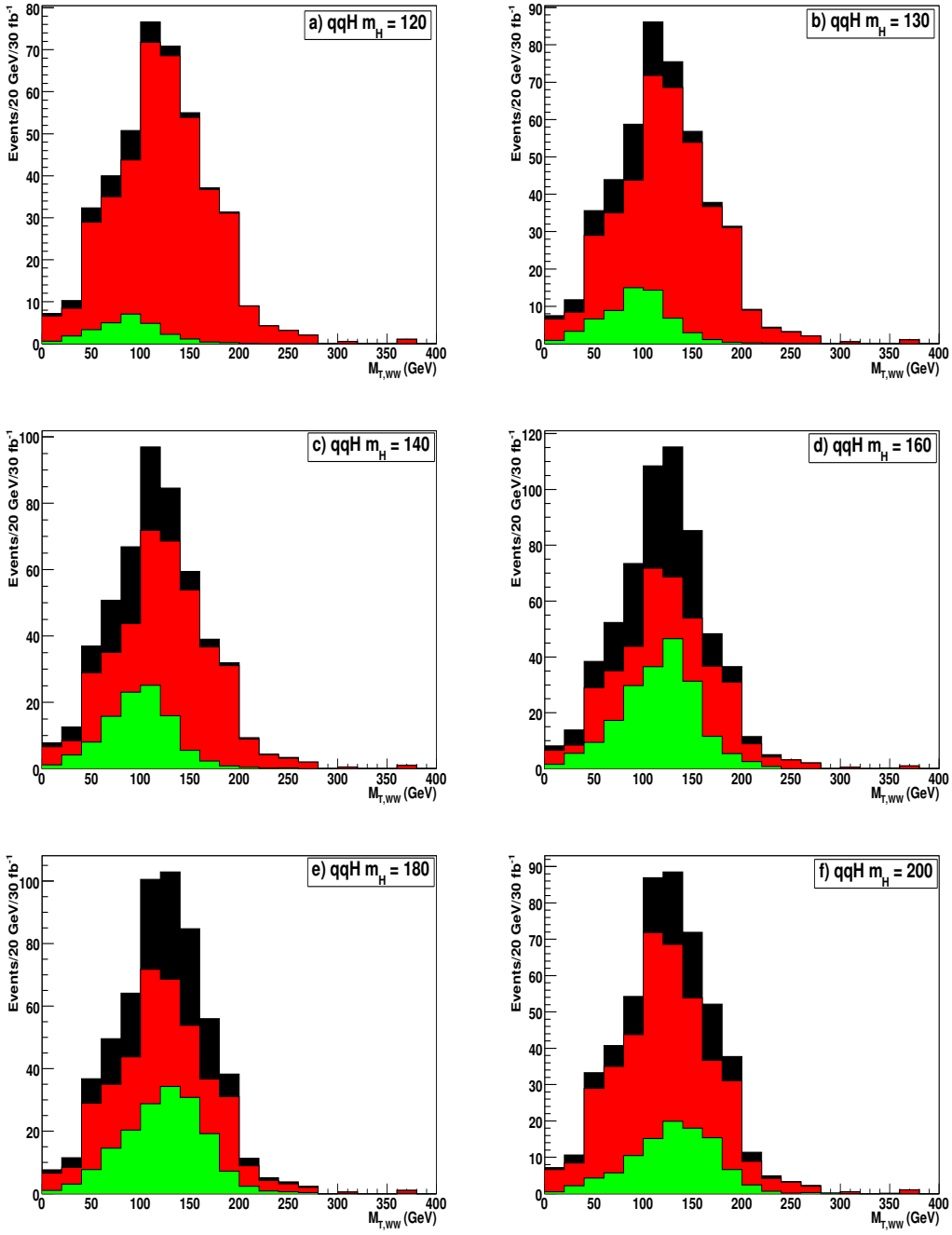

Figure 5.14: The transverse mass, $M_{T,WW}$, distributions for signal and background, with Higgs mass = 120, 130, 140, 160, 180 and 200 GeV respectively shown in a),b),c),d),e),f). The Lower plot (light grey) is the signal, the middle plot(dark grey) is the background, and the black histogram is the sum.

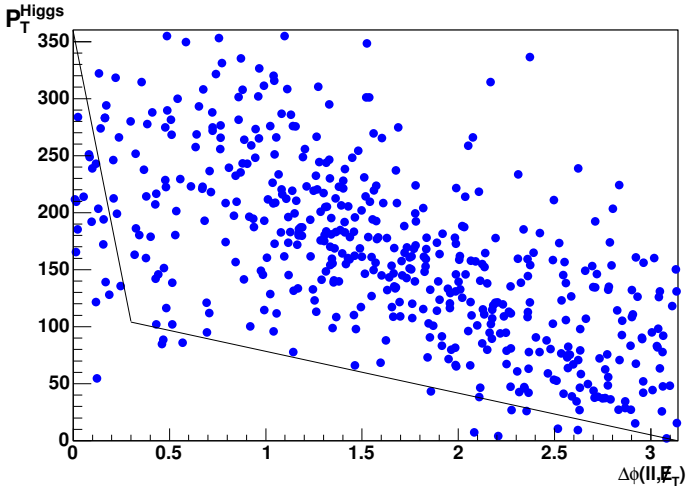

Figure 5.15: The azimuthal angle difference (in radians) between the dilepton momentum as a function of $\not{E}_T$ vs p_T^{Higgs} for qqH with $m_H = 120$ GeV. The lines in the figure correspond to the cuts: $57.29\Delta\phi(ll,\not{E}_T) + 1.5p_T^{Higgs} > 180$ and $12 \times 57.29\Delta\phi(ll,\not{E}_T) + p_T^{Higgs} > 360$.

5.5 Results

The total accepted signal cross sections range from about 0.8 fb up to 7.2 fb, depending on the Higgs mass. They are listed in Table 5.2. The contributions from the e^+e^- and $\mu^+\mu^-$ channel are very similar, and the $e^\pm\mu^\mp$ channels are twice as large due to branching ratios. The total efficiency is 3–6%, depending on m_H. The background cross sections are somewhat larger, and there are two background values corresponding to the "low-mass" and the "high-mass" cuts – see Table 5.2.

We computed the significance S_{cP} of an excess of events over the $t\bar{t}j$ and W^+W^-jj backgrounds, assuming an integrated luminosity of $\mathcal{L} = 10,\ 30$ and

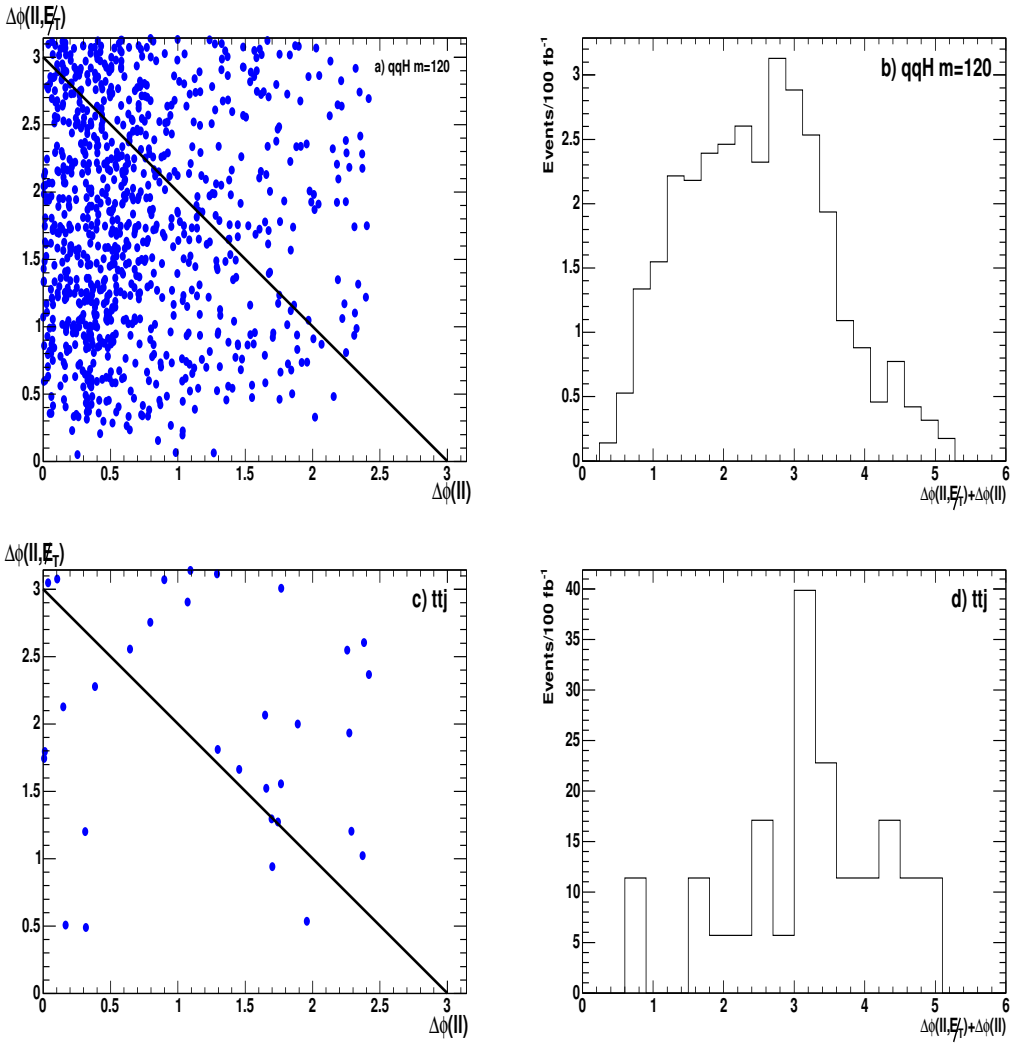

Figure 5.16: a) $\Delta\phi(ll, \not{E}_T)$ vs. $\Delta\phi_{ll}$ and b) the sum of $\Delta\phi_{ll}$ and $\Delta\phi(ll, \not{E}_T)$ for qqH $m_H = 120$ and for ttj bacground c) and d). The lines correspond to $\Delta\phi_{ll} + \Delta\phi(ll, \not{E}_T) = 3$ radians.

100 fb^{-1}. S_{cP} is the probability calculated assuming a Poisson distribution with N_B background events to observe equal or greater than a total number of signal and background events ($N_S + N_B$), converted to an equivalent number of sigmas for a Gaussian distribution [78]. The code to calculate the S_{cP} is taken from Ref. [79].

The background uncertainty is included in the calculation. This uncertainty comes from the statistical error in the background estimation and amounts to about 12% at 10 fb^{-1}, 7% at 30 fb^{-1} and 4% at 100 fb^{-1}. See Section 5.5.1 for a discussion of the background estimation.

The results are summarized in Table 5.3. Even for a Higgs mass as low as 130 GeV, a 5σ signal can be obtained with a reasonable amount of luminosity. For higher Higgs masses, a very strong signal would be expected, and prospects of a measurement of the cross section for $pp \rightarrow qqH$ become more promising. Fig. 5.17 shows the significance for an integrated luminosity of 30 fb^{-1} as a function of m_H, and Fig. 5.18 shows the minimum integrated luminosity needed for a 5σ signal also as a function of m_H. The individual cut efficiencies with respect to the starting cross section for 120 and 160 GeV Higgs bosons and the backgrounds are shown in Tables 5.4,5.5,5.6 for each channel.

We can loosen the analysis cuts to increase signal statistics. We changed the cut on the highest E_T jet to 40 GeV, and the separation between the tagging jets to η =3.8. The di-jet mass cut is changed to 400 GeV/c^2 and we also required

	accepted cross sections (fb)			
channel	e^+e^-	$e^\pm\mu^\mp$	$\mu^+\mu^-$	sum
"low" mass				
qqH, $m_H = 120$ GeV	0.183	0.400	0.253	0.836
qqH, $m_H = 130$ GeV	0.387	0.854	0.601	1.842
qqH, $m_H = 140$ GeV	0.617	1.341	0.955	2.913
$t\bar{t}j$	1.139	2.621	1.065	4.825
W^+W^-jj (EWK)	0.081	0.144	0.092	0.317
W^+W^-jj (QCD)	0.093	0.207	0.119	0.419
all backgrounds				5.561
"high" mass				
qqH, $m_H = 160$ GeV	1.587	3.497	2.102	7.186
qqH, $m_H = 180$ GeV	1.362	3.089	1.837	6.288
qqH, $m_H = 200$ GeV	0.815	1.703	1.087	3.605
$t\bar{t}j$	2.088	4.216	2.024	8.328
W^+W^-jj (EWK)	0.127	0.245	0.165	0.537
W^+W^-jj (QCD)	0.192	0.394	0.252	0.838
all backgrounds				9.703

Table 5.2: Summary of accepted cross sections, in fb. A series of assumed Higgs boson masses is shown, as well as the backgrounds for the "low-mass" and "high-mass" cuts.

Higgs mass	significance			$\mathcal{L}^{5\sigma}_{\text{min}}$
(GeV)	10 fb^{-1}	30 fb^{-1}	100 fb^{-1}	(fb^{-1})
120	0.72	1.35	2.60	340
130	1.77	3.04	5.85	72
140	2.68	4.79	8.33	33
160	4.54	7.00	13.0	12
180	3.95	6.22	11.6	15
200	2.31	4.03	6.99	45

Table 5.3: Significance of an excess as a function of Higgs mass, for three assumed integrated luminosities. The last column shows the minimum luminosity required for a 5σ excess.

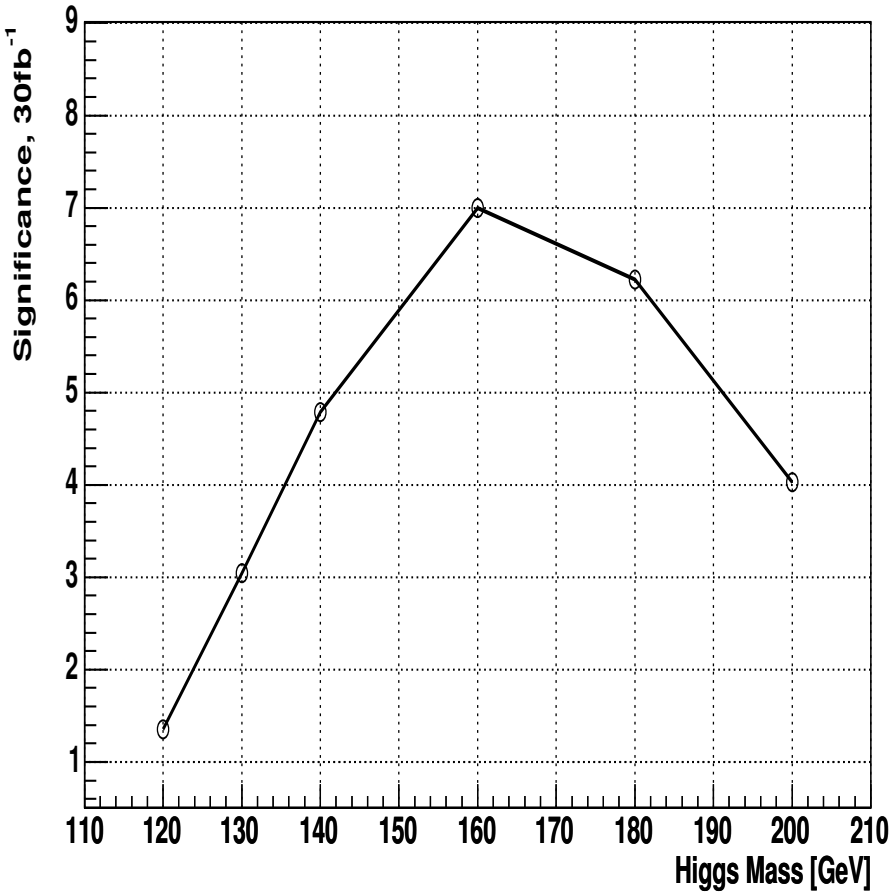

Figure 5.17: Significance of the Higgs signal as a function of Higgs mass for a 30 fb^{-1} integrated luminosity.

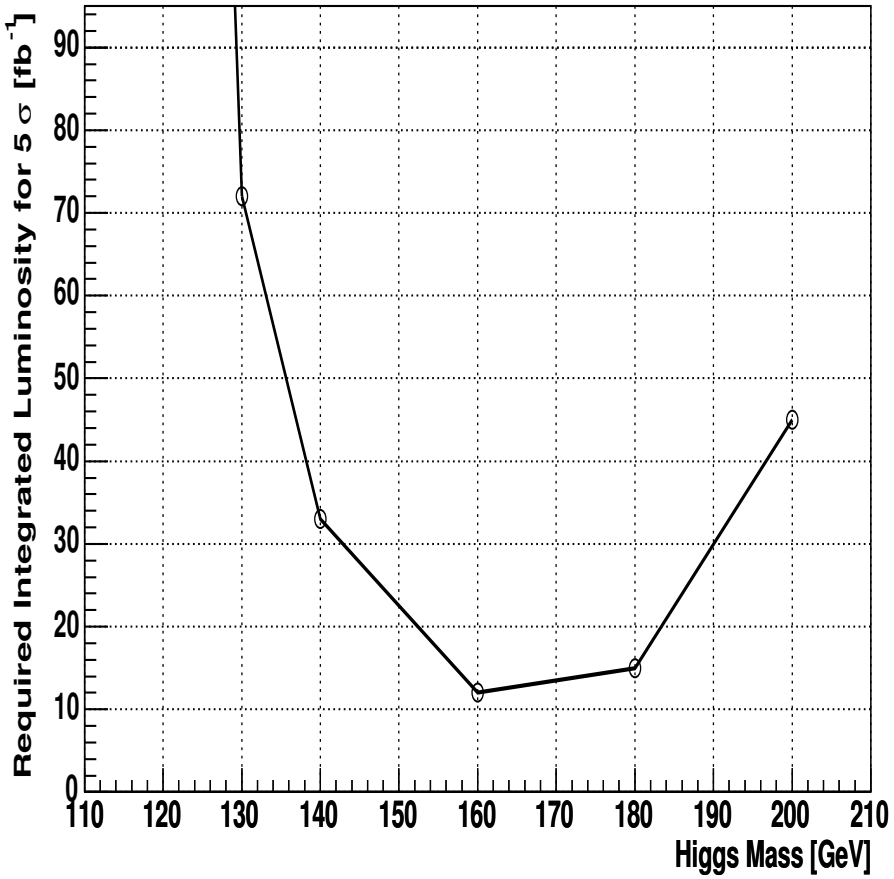

Figure 5.18: Minimum integrated luminosity (fb^{-1}) needed to obtain a 5σ excess over the $t\bar{t}j + W^+W^-jj$ background as a function of the Higgs mass.

Cut	H120	H160	ttj	WWjj^{ew}	WWjj^{qcd}
	5.261	26.97	8617.	10.74	514.3
$p_{T1} > 50$,$p_{T2} > 30$	3.742	18.70	6743.	8.838	296.4
$\Delta\eta > 4.2$	1.217	6.067	184.2	2.195	12.22
$\eta_1 \times \eta_2 < 0$	1.215	6.054	183.1	2.193	12.18
$M_{jj} > 600$	1.073	5.367	147.2	2.071	9.052
$\mathrm{P}_T - balance$ cut	0.653	3.353	54.89	1.021	3.298
Central Jet Veto	0.401	2.309	15.04	0.631	1.490
$\geq$2 good leptons w opp. charge	0.269	1.915	10.98	0.483	0.695
$E_T > 20, 10$ or $E_T > 26, 12$	0.250	1.838	10.59	0.475	0.675
$\lvert\Delta R(j,l)\rvert > 0.7$	0.250	1.830	10.33	0.471	0.662
Req. leptons between jets	0.235	1.712	4.990	0.417	0.430
$M_{ll} < 80$	0.235	1.683	2.386	0.144	0.205
$\Delta\phi_{ll} < 2.4$	0.220	1.587	2.088	0.127	0.192
$M_{T,WW} < 125$	0.183		1.139	0.081	0.093
$\Delta\phi(ll,\not{E}_T) + 1.5P_T(H) > 180$ &					
$12\Delta\phi(ll,\not{E}_T) + P_T(H) > 360$	0.161	1.501	0.936	0.069	0.073
$M_{ll} > 10 \& \not{E}_T > 30 (ee, \mu\mu)$	0.115	1.303	0.800	0.053	0.060
$\Delta\phi(ll,\not{E}_T) + \Delta\phi_{ll} < 172$	0.090	0.862	0.420	0.031	0.033
High Mass Cuts					
No $M_{T,WW}$ Cut			2.088	0.127	0.192
$\Delta\phi(ll,\not{E}_T) + 1.5P_T(H) > 180$ &					
$12\Delta\phi(ll,\not{E}_T) + p_T(H) > 360$			1.885	0.114	0.172
$M_{ll} > 10 \& \not{E}_T > 30 (ee, \mu\mu)$			1.736	0.098	0.152
$\Delta\phi(ll,\not{E}_T) + \Delta\phi_{ll} < 172$			0.651	0.052	0.046

Table 5.4: Accepted signal (for m_H=120,160 GeV) and major background cross sections in fb for the $H \to WW \to ee\nu\nu$ final state.

Cut	H120	H160	ttj	WWjj^{ew}	WWjj^{qcd}
	10.57	53.24	17230.	21.48	1029.
$p_{T1} > 50$,$p_{T2} > 30$	7.290	35.54	13320.	17.22	537.1
$\Delta\eta > 4.2$	2.458	12.56	358.5	4.533	24.39
$\eta_1 \times \eta_2 < 0$	2.454	12.55	355.5	4.526	24.25
$M_{jj} > 600$	2.149	11.08	282.0	4.299	18.28
$\mathrm{P}_T - balance$ cut	1.398	7.390	117.4	2.405	8.287
Central Jet Veto	0.879	5.128	32.70	1.502	4.123
$\geq$2 good leptons w opp. charge	0.670	4.388	25.07	1.186	2.102
$E_T > 20, 10$	0.544	4.079	23.47	1.131	1.975
$\lvert\Delta R(j,l)\rvert > 0.7$	0.539	4.052	21.71	1.100	1.881
Req. leptons between jets	0.506	3.748	10.60	0.920	1.068
$M_{ll} < 80$	0.505	3.685	5.014	0.301	0.447
$\Delta\phi_{ll} < 2.4$	0.480	3.497	4.216	0.245	0.394
$M_{T,WW} < 125$	0.400		2.621	0.144	0.207
$\Delta\phi(ll,\not\!\!E_T) + 1.5P_T(H) > 180$ &					
$12\Delta\phi(ll,\not\!\!E_T) + P_T(H) > 360$	0.329	3.105	1.880	0.109	0.153
$\not\!\!E_T > 30$ if $p_T(H) < 50$	0.323	3.084	1.823	0.105	0.153
$\Delta\phi(ll,\not\!\!E_T) + \Delta\phi_{ll} < 172$	0.239	2.003	0.798	0.066	0.08
High Mass Cuts					
No $M_{T,WW}$ Cut			4.216	0.245	0.394
$\Delta\phi(ll,\not\!\!E_T) + 1.5P_T(H) > 180$ &					
$12\Delta\phi(ll,\not\!\!E_T) + P_T(H) > 360$			3.418	0.202	0.334
$\not\!\!E_T > 30$ if $p_T(H) < 50$			3.361	0.199	0.334
$\Delta\phi(ll,\not\!\!E_T) + \Delta\phi_{ll} < 172$			1.709	0.107	0.173

Table 5.5: Accepted signal (for m_H=120,160 GeV) and major background cross sections in fb for the $H \to WW \to e\mu\nu\nu$ final state.

Cut	H120	H160	ttj	WWjj^{ew}	WWjj^{qcd}
	5.133	29.44	8617.	10.77	512.7
$p_{T1} > 50$,$p_{T2} > 30$	3.357	18.31	6621.	8.332	232.5
$\Delta\eta > 4.2$	1.271	7.391	178.0	2.365	12.11
$\eta_1 \times \eta_2 < 0$	1.268	7.375	176.7	2.360	12.06
$M_{jj} > 600$	1.109	6.522	139.7	2.251	8.988
$\mathrm{P}_T - balance$ cut	0.854	4.947	55.75	1.585	5.768
Central Jet Veto	0.562	3.523	19.55	1.007	3.139
$\geq$2 good leptons w opp. charge	0.430	2.891	16.11	0.772	1.472
$E_T > 20, 10$	0.327	2.605	14.30	0.716	1.324
$\lvert\Delta R(j,l)\rvert > 0.7$	0.319	2.537	11.59	0.680	1.186
Req. leptons between jets	0.290	2.298	5.461	0.556	0.548
$M_{ll} < 80$	0.290	2.226	2.371	0.190	0.271
$\Delta\phi_{ll} < 2.4$	0.273	2.102	2.024	0.165	0.252
$M_{T,WW} < 125$	0.253		1.065	0.092	0.119
$\Delta\phi(ll,\not{E}_T) + 1.5P_T(H) > 180$ &					
$12\Delta\phi(ll,\not{E}_T) + P_T(H) > 360$	0.200	1.908	0.826	0.075	0.095
$M_{ll} > 10 \& \not{E}_T > 30 (ee, \mu\mu)$	0.159	1.681	0.746	0.060	0.076
$\Delta\phi(ll,\not{E}_T) + \Delta\phi_{ll} < 172$	0.134	1.229	0.426	0.051	0.062
High Mass Cuts					
No $M_{T,WW}$ Cut			2.024	0.165	0.252
$\Delta\phi(ll,\not{E}_T) + 1.5P_T(H) > 180$ &					
$12\Delta\phi(ll,\not{E}_T) + P_T(H) > 360$			1.785	0.147	0.229
$\not{E}_T > 30$ if $p_T(H) < 50$			1.678	0.132	0.205
$\Delta\phi(ll,\not{E}_T) + \Delta\phi_{ll} < 172$			0.746	0.092	0.119

Table 5.6: Accepted signal (for m_H=120,160 GeV) and major background cross sections in fb for the $H \to WW \to \mu\mu\nu\nu$ final state.

the di-jet mass to be lower than 2.5 TeV/c^2. Moreover, we loosen the central jet veto condition by reducing $|\eta_0|$ cut to 1.5 from 2. The results for qqH 120 GeV case and ttj for the $e\mu$ channel is displayed in Table 5.7. However, $S/\sqrt{B}$ calculated with the loose cuts is 0.205 and it is 0.268 with our original analysis cuts and loosening the cuts only increases the accepted number of signal events by $\sim 20\%$. Thus, we do not expect much improvement by using looser cuts.

Cut	$qqH120$	ttj
	10.57	17234
$p_{T1} > 40$,$p_{T2} > 30$	7.837	13977
$\Delta\eta > 3.8$	3.272	626.8
$\eta_1 \times \eta_2 < 0$	3.231	609.1
$400 < M_{jj} < 2500$	2.922	545.0
$\mathrm{P}_T - balance$ cut	1.866	239.8
Central Jet Veto ($\|\eta_0\| < 1.5$)	1.283	95.48
At least 2 good leptons w opp. charge	0.957	76.34
$E_T > 20, 10$	0.764	71.90
$\|\Delta R(j,l)\| > 0.7$	0.757	67.11
Req. leptons between jets	0.677	27.86
$M_{ll} < 80$	0.677	14.07
$\Delta\phi_{ll} < 2.4$	0.640	12.25
$M_{T,WW} < 125$	0.520	6.039
$\Delta\phi(ll,\not{E}_T) + 1.5P_T(H) > 180$ & $12\Delta\phi(ll,\not{E}_T) + P_T(H) > 360$	0.416	4.444
$\not{E}_T > 30$ if $p_T(H) < 50$	0.408	4.387
$\Delta\phi(ll,\not{E}_T) + \Delta\phi_{ll} < 172$	0.286	1.937

Table 5.7: Accepted signal (for m_H=120 GeV and for ttj) cross-sections in fb for the $H \to WW \to e\mu\nu\nu$ with looser forward jet tagging, di-jet mass cut, and central jet veto. The production of Higgs is via vector boson fusion.

Concerning systematics, we have first considered the impact of the jet energy scale. The expected jet energy scale uncertainty in CMS is about 3%. For the $t\bar{t}j$

background the scale uncertainty after correction is about 5% for $E_T > 30\ GeV$. In this analysis, the two tag jets are required to have E_{T1} >50 GeV and E_{T2} >30 GeV and we reject additional jets in the central region if their $E_T > 20\ GeV$. For the jets with $E_T \sim 20\ GeV$, the cross section uncertainty after jet correction is about 10%. We re-computed all yields after scaling the raw jet energies up and down by 10%. In general, signal and background yields correlate, so the impact on the significance with a 10% jet energy scale uncertainty is less than $\sim 8 - 10\%$ at 30 fb^{-1} .

We also tested our results for the significances to errors in the $\not{E}_T$ scale. Increasing the $\not{E}_T$ scale by 10% decreases the significance by 9 – 11%. Decreasing the $\not{E}_T$ scale by 10% increases the significance by 0.3 – 3.4% depending on m_H. This is a systematic uncertainty on the signal cross section.

We also used the Pythia event generator for our signal as an alternative to MadGraph. For $m_H = 120$ GeV, the significance obtained with Pythia is higher by 30% for a luminosity of 100 fb^{-1}, while for $m_H = 160$ GeV, it is higher by 10 %.

We found that the production cross section depends on the choice of scale (renormalization scale×factorization scale) for the $t\bar{t}j$ background. The $t\bar{t}j$ cross section is 736.5 pb as reported in Table 1, with the definition of the scale Σm_T^2, where $m_T^2 = m_{top}^2 + p_T^2$ and the sum is over *final state light partons*. However, if we change the definition of the above sum to include *all the final state partons*

including the heavy quarks, then the cross section decreases to 530 pb. These two definitions of scale are the defaults in AlpGen 1.3.3 and 2.0.x respectively. We found that the choice of scale does not affect the kinematics of $t\bar{t}j$ at all. Moreover, the cross section and kinematics of the qqH process are not affected by the choice of scale. The significance with the new scale choice is $\sim$ 18% higher. Therefore, the uncertainties in the computed $t\bar{t}j$ background make it very important to measure the background directly in the experiment.

It should be pointed out that the statistical significance of our analysis is generally a factor of $\sim$ 2.6–3.2 lower than the significance reported in the study for the ATLAS detector [66]. There are several reasons for this difference. First of all, the $t\bar{t}j$ cross section used in Ref [66] is smaller than the cross section we use by about a factor of 0.7. Furthermore, the ATLAS study includes the gluon-gluon fusion channel for Higgs production which increases the signal by about 10%.

Another important difference between the two analyses concerns the central jet veto. Our signal simulation generates a larger number of central jets compared to the ATLAS study, which used the PYTHIA Monte Carlo event generator. When we compare the signal efficiency after all cuts using PYTHIA instead of MadGraph, we find a difference of $\sim 5 - 50\%$. Finally, the very definition of significance (S_{cP}) differs between the two studies. The ATLAS study used a definition which gives a value which is $\sim$ 9–14% higher for the same

number of signal and background events. If the number of background events is reduced, the apparent improvement in the significance increases more dramatically than for our measure of significance. Thus the uncertainty of $\sim$ 9–14% should be taken as a lower limit for this particular factor. Considering all of the above, the differences between our results and those reported in Ref. [66] can be understood. Nonetheless, these considerations show that there still are uncertainties in the modeling of this channel which should be investigated by both experiments.

5.5.1 Background Estimation from the Data

For the Higgs masses considered here, there is practically no signal with $M_{\ell\ell} > 110$ GeV – see Fig. 5.10. For the present discussion we define this as the *signal-free or control region*. Fig. 5.19 shows the $M_{\ell\ell}$ distribution computed with looser cuts (no central jet veto, no p_T-balancing cut, $|\Delta\eta| > 3.5$, $\eta_{\rm lo} + 0.3 < \eta_\ell < \eta_{\rm hi} - 0.3$) and the full analysis cuts. The number of events with $M_{\ell\ell} > 110$ GeV is designated by "a" for the distribution with looser cuts and by "c" for the full analysis cuts. The number of events for $M_{\ell\ell} < 80$ GeV is designated by "b" for the distribution with looser cuts and by "d" for the full analysis cuts. The region $80 < M_{\ell\ell} < 110$ GeV is excluded from the calculation in order to avoid any background coming from $Z \to \ell^+\ell^-$. Since $M_{\ell\ell} > 110$ GeV represents the signal-free region, we can use the numbers a, c and b to estimate the number

of background events in the region where we expect the signal (i.e., d). Using the simulations, we find that $c/a = 0.097$ and $d/b = 0.098$. The error on this estimation is dominated by the statistical uncertainty which is $\sqrt{c}/c \approx 7\%$. In order to obtain the background distribution in $M_{T,WW}$, we take the distribution obtained with the looser cuts and scale it by factor of 0.098. A comparison of the true and rescaled background distributions is given in Fig. 5.20 which indicates that this "data driven" method works quite well.

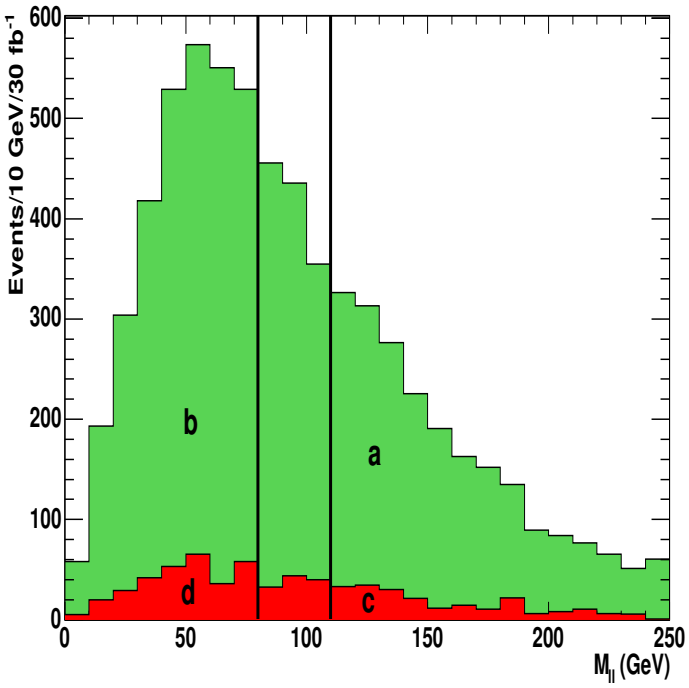

Figure 5.19: $M_{\ell\ell}$ distribution computed with looser cuts and full analysis cuts.

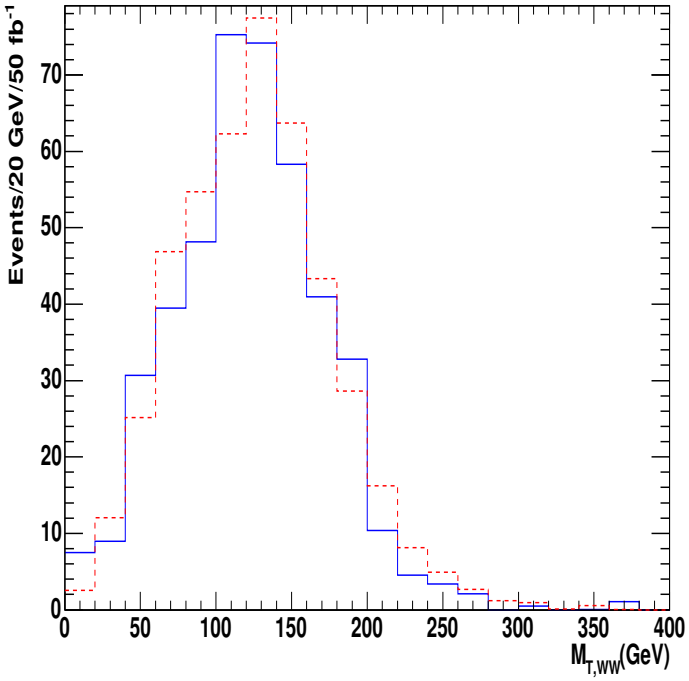

Figure 5.20: The transverse mass, $M_{T,WW}$ distribution for estimated(dashed) and real(solid) background.

5.5.2 Sensitivity to the Higgs Mass

The above significance estimates are for a pure "counting experiment" since the kinematic cuts makes the events appear in the region where there is the signal. We can, in addition, use the information contained in the distribution of $M_{T,WW}$ with regard to the Higgs mass. We infer the mass of the Higgs boson from the observed distribution in $M_{T,WW}$ by subtracting the data-driven estimate of the background $M_{T,WW}$ distribution from the distribution obtained with the full set of analysis cuts. The estimated and real $M_{T,WW}$ distributions for signal events are shown in Fig. 5.21 for several different Higgs boson masses. The inferred and the real mean values and shapes approximately agree.

In an effort to obtain a quantitative measure of m_H, we can use signal $M_{T,WW}$ distributions as templates to be compared to the observed distribution. The comparison is done using the Kolmogorov-Smirnov test, and the results are shown in Fig. 5.22. A value close to 1 indicates a good match between the shapes. Comparing the means and shapes of the observed and template distributions, we can differentiate between Higgs boson masses for the cases of 160, 180 and 200 GeV, and for low masses (120 – 140 GeV). To differentiate between the cases of 120, 130 and 140 GeV Higgs mass, we must reduce the $t\bar{t}j$ background more or we must have data corresponding to an integrated luminosity greater than 50 fb^{-1}.

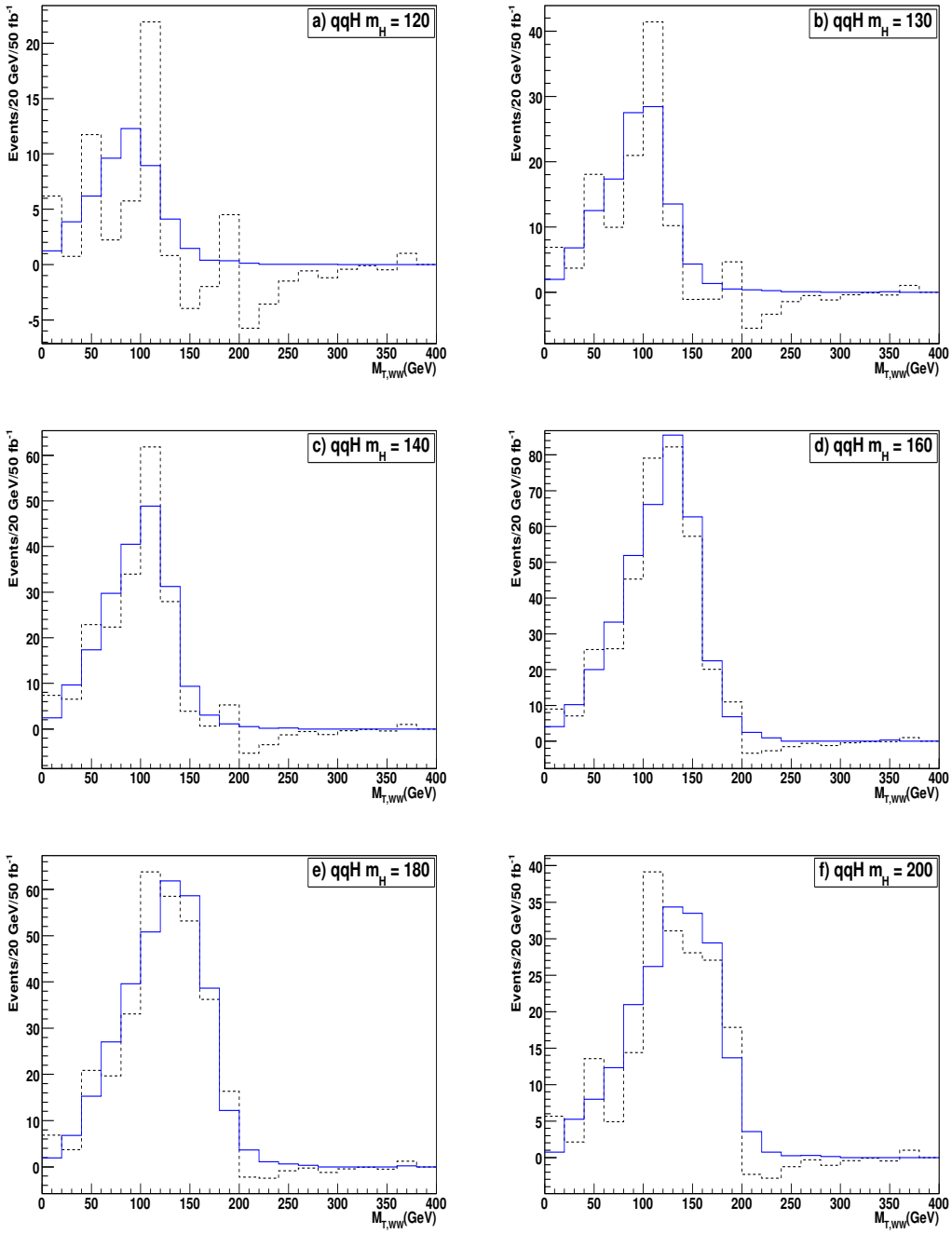

Figure 5.21: Estimated(dashed) and real(solid) $M_{T,WW}$ distributions for signal events, with Higgs mass of 120,130,140,160,180 and 200 GeV shown in a),b),c),d),e) and f) respectively.

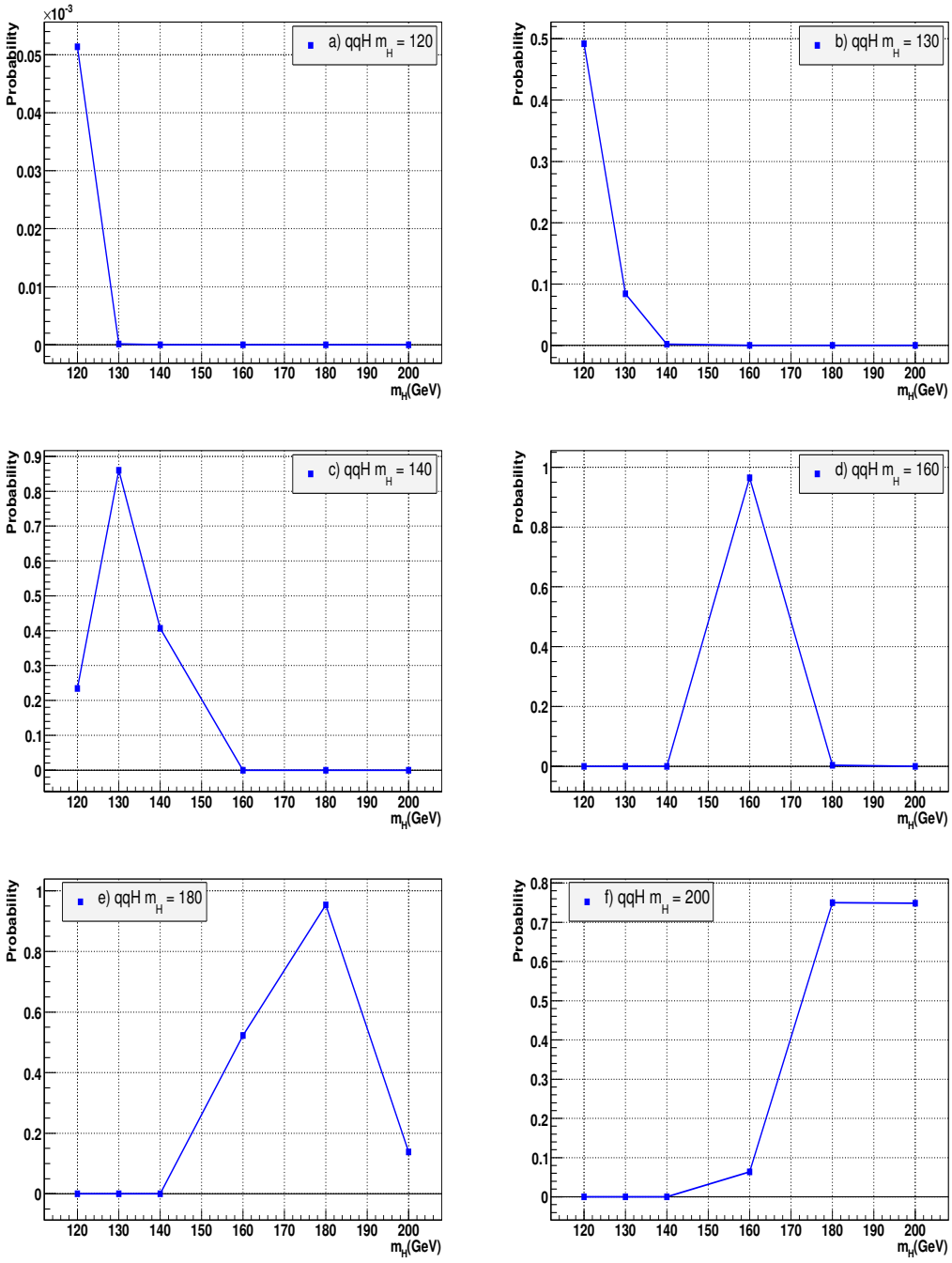

Figure 5.22: Kolmogorov test function for estimating the Higgs boson mass for Higgs masses of 120,130,140,160,180 and 200 GeV shown in a),b),c),d),e) and f) respectively.

CHAPTER 6

CONCLUSION

An analysis to isolate a discovery signal for a Standard Model Higgs boson produced by vector boson fusion which then decays into WW^* is presented. The final state in which both of the W bosons decay to electrons/muons is utilized. The study is based on a full simulation of the CMS detector. Furthermore, the main backgrounds, $t\bar{t}j$ and W^+W^-jj, are generated as accurately as is presently possible. The total accepted signal cross section is 0.8-7.2 fb and the corresponding signal efficiency is $\sim 3-6\%$ depending on the Higgs boson mass. The results are encouraging, and indicate that a signal with a statistical significance of over 5σ can be obtained with an integrated luminosity of $11-72$ fb^{-1} for Higgs boson masses in the range $130 < m_H < 200$ GeV/c^2. There are some uncertainties in the backgrounds, therefore a method to determine the background from data is developed. The analysis shows that the background can be measured to 7% accuracy directly from the data. This uncertainty is dominated by statistics for 30 fb^{-1}. CMS is not only capable of discovering the Higgs boson, but it also can measure some of its physical properties. In

this study, a method to measure the Higgs mass using the shape of the WW-transverse mass distributions is suggested.

A method to optimize the energy reconstruction in CMS using the Test Beam 2006 data in the energy range 4-300 GeV is presented. The corrected responses become 100% with at most 6% fluctuation and the stochastic part of the resolution parametrization is improved from 111% to 94%.

REFERENCES

[1] P.W. Higgs, Phys. Lett. **12**, 132 (1964).

[2] P.W. Higgs, Phys. Rev. Lett. **13**, 508 (1964).

[3] P.W. Higgs, Phys. Rev. **145**, 1156 (1966).

[4] F. Englert and R. BroutPhys. Rev. Lett. **13**, 321 (1964).

[5] "Shape of the 'Mexican hat' potential in two dimensions", http://www.fuw.edu.pl/ dobaczew/maub-42w/img123.png (25/06/2007).

[6] C. Quigg, arXiv:0704.2232v2 (2007).

[7] A. O. Barut, Phys. Rev. Lett. **42**, 1251 (1979).

[8] W.-M. Yao *et al.*, J. Phys. G **33**, 1 (2006).

[9] F. Englert and R. Brout, Phys. Rev. Lett. **13**, 321 (1964)

[10] G.S. Guralnik, C.R. Hagen and T.W. Kibble, Phys. Rev. Lett **13** 585 (1964).

[11] S.H. Ahn *et al.* Nucl. Instr. and Meth. A **469**, (2001) 323.

[12] A. Djouadi, J. Kalinowski and M. Spira, Comput. Phys. Comm. **108**, 56 (1998).

[13] F. Gianotti, Phys. Rept. **403**, 379 (2004).

[14] T. Han, S. Heinemeyer, F. Maltoni, G. Weiglein, and S. Willenbrock, arXiv:hep-ph/0607308 (2006).

[15] O. Brein, A. Djouadi and R. Harlander, arXiv:hep-ph/0307206 (2003).

[16] U. Aglietti, A. Belyaev, S. Berge, A. Blum, R. Bonciani, J. Cammin, M. Carena, S. Chivukula, H. Davoudiasl, S. Dawson, G. Degrassi, A. Dominguez, J. Donini, T. Dorigo, B.J. Field, T. Hahn, T. Han, S. Heinemeyer, G.-Y. Huang, I. Iashvilli, C.B. Jackson, T. Junk, S.-W. Lee, H.E. Logan, F. Maltoni, B. Mellado, S. Mrenna, P.M. Nadolsky, F.I. Olness, W. Quayle, L. Reina, E.H. Simmons, A. Vicini, D. Wackeroth, C.E.M. Wagner, G. Weiglein, G. Weiglein, S. Willenbrock, S.L. Wu, C.P. Yuan, TeV4LHC Higgs Working Group, arXiv:hep-ph/0612172 (2006).

[17] K. Peters, arXiv:0706.1278v1 [hep-ex] (2007).

[18] TEVNPH working group for CDF and D0 Collaborations, arXiv:hep-ex/0612044v1 (2006).

[19] T. Hambye and K. Riesselmann, arXiv:hep-ph/9610272v1 (1996)

[20] R.V. Harlander and W.B. Kilgore, Phys. Rev. Lett. **88**, 201801 (2002)

[21] C. Anastasiou and K. Melnikov, Nucl. Phys. B **646**, 220 (2002).

[22] A. Djouadi, arXiv:hep-ph/0503172 (2005).

[23] T. Han, G. Valencia and S. Willenbrock, Phys. Rev. Lett. **69**, 3274 (1992).

[24] M.L. Ciccolini, S. Dittmaier and M. Kramer, arXiv:hep-ph/0306234v2 (2003).

[25] S. Dawson, L.H. Orr, L. Reina, and D. Wackeroth, Phys. Rev. D **67**, 071503 (2003).

[26] S. Dawson and L. Reina, Phys. Rev. D**57**, 5851 (1998).

[27] W. Beenakker, S. Dittmaier, M. Kraemer, B. Plumper, M. Spira, and P.M. Zerwas, Nucl. Phys. B **653**, 151 (2003)

[28] J. Huston *et al.*, JHEP **0506**, 080 (2005).

[29] J. Pumplin *et al.*, JHEP **0207**, 012 (2002).

[30] A. Kotwal, "The First Run II Measurement of the W Boson Mass by CDF", http://theory.fnal.gov/jetp/talks/kotwal.pdf (05/01/2007)

[31] LEP electroweak working group, http://lepewwg.web.cern.ch/LEPEWWG (29/03/2007).

[32] B.W Lee, C. Quigg, H.B. Thacker, Phys. Rev. Lett. **38**, 883 (1977) and Phys. ReV. D **16**, 1519 (1977).

[33] Ellis, R.K., Stirling, W.J., Webber, B.R., "QCD and Collider Physics", Cambridge, Monographs on Part. Nucl. Phys. and Cosmo. (1996).

[34] "Search for the Higgs Boson in $H \to WW* \to ll'$ Decays with 950 pb^{-1}", http://www−d0.fnal.gov/Run2Physics/WWW/results/prelim/HIGGS/H16/H16.pdf (17/03/2006)

[35] W.-M. Yao et al., "The Review of Particle Physics", J. Phys. G **33**, 1 (2006).

[36] N. Varelas, "SM Higgs Searches at the Tevatron", FERMILAB-CONF-05-592-E, HEP-EPS Conference, Lisbon, July 21-27 (2005).

[37] S. Kraml, E. Accomando, A.G. Akeroyd, arXiv:hep-ph/0608079 (2006).

[38] D. Rainwater, arXiv:hep-ph/0702124v2 (2007).

[39] J. Tanaka, Nucl. Phys. B. (proc. suppl.) **144**, 341 (2005).

[40] O. Bruening, P. Collier, P. Lebrun, S. Myers, R. Ostojic, J. Poole, P. Proudlock, LHC Design Report, Technical Report, CERN-2004-003, CERN (2004).

[41] The CMS Collaboration, "The Magnet Project, Technical Design Report", CERN/LHCC 97-10, CMS TDR 1 (1997).

[42] The CMS Collaboration, "The Muon Project, Technical Design Report", CERN/LHCC 97-32, CMS TDR 3 (1997).

[43] M. De Giorgi, F. Gasparini, I. Lippi, R. Martinelli, G. Zumerle, P. Zotto, "Design and Simulations of the Trigger Electronics for the CMS Muon Barrel Chambers", CMS TN/95-01, CERN (1995).

[44] C. Albajar, M. G. Albrow, O.C. Alkofer, G. T. J. Arnison, A. Astbury, B. Aubert, *et al.* Nucl. Inst. and Meth. A 525 (2004) 465.

[45] I. Belotelov and N. Neumeister, "Performance of the CMS Offline Reconstruction Software", CMS AN 2005/010, CERN (2005).

[46] TOTEM: Letter of Intent, CERN-LHCC 97-49; Technical Proposal, CERN-LHCC 99-7; Technical Design Report, CERN-LHCC-2004-002.

[47] CMS collaboration, http://cmsinfo.cern.ch (28/07/2007).

[48] CMS outreach muon detectors overview, http://cmsinfo.cern.ch/outreach/CMSdetectorInfo/MuonDetectors/page1.html (20/06/2007)

[49] R. Wigmans, "Calorimetry: Energy Measurement in Particle Physics" , Oxford University Press Inc., New York (2000)

[50] J. Damgov and S. Kunori, private communication.

[51] CMS Collaboration, "ECAL Techincal Design Report", CERN/LHCC **97-033** (1997)

[52] CMS Collaboration, "The Hadron Calorimeter Technical Design Report", CERN/LHCC **97-031** (1997); CMS TDR Volume II, CERN/LHCC **06-021** (2006).

[53] G. Baiatian, A. Sirunyan, I. Emeliantchik, V. Massolov, N. Shurneiko, R. Stefanovich, J. Damgov, *et al.* "Design, Performance, and Calibration of CMS Forward Calorimeter Wedges", CMS NOTE 2006/044 (2006).

[54] N. Akchurin and R. Wigmans, Rev. Scien. Instr. **74**, No. 6 (2002)

[55] CMS Collaboration, "The Tracker Project Technical Design Report", CERN/LHCC **98-006** (1998) and CMS TDR 5, Addendum CERN/LHCC **20-016**

[56] S. Wagner, "CMS Tracking Basics", Talk given at USCMS Weekly Meeting, http://indico.cern.ch/getFile.py/access?contribId=1&resId=0&materialId=slides&confId=3410 (02/06/2006).

[57] "Level-1 Trigger Technical Design Report", CERN/LHCC 2000-038 (2000); http://cmsdoc.cern.ch/cms/TDR/TRIGGER-public/trigger.html (15/12/2000).

[58] "DAQ and High-Level Trigger Technical Design Report", CERN/LHCC 2002-026 (2002).

[59] The CMS Collaboration, "CMS Physics Technical Design Report (Vol II)", J. Phys. G: Nucl. Part. Phys. **34**, 995 (2007).

[60] The CMS Collaboration, "CMS Physics Technical Design Report (Vol I)", http://cmsdoc.cern.ch/cms/cpt/tdr/ptdr1_final_colour.pdf (02/02/2006).

[61] P. Adzic, R. Alemany-Fernandez, C. B. Almeida, *et al.* EPJ-C **13**, 23 (2006).

[62] LEP Higgs Working Group, Phys. Lett. **B565**, 61 (2003).

[63] Tevatron Electroweak Working Group, "Combination of CDF and DØ results on the top-quark mass", hep-ex/0507091 (2005).

[64] N. Kauer, T. Plehn, D. Rainwater, D. Zeppenfeld, Phys. Lett. **B503**, 113 (2001).

[65] N. Akchurin, D. Green, S. Kunori, R. Vidal, W. Wu, M.T. Zeyrek, CMS NOTE 2002/016 (2002).

[66] S. Asai, G. Azuelos, C. Buttar, V. Cavasinni, D. Costanzo, K. Cranmer, R. Harper, K. Jakobs, J. Kanzaki, M. Klute, R. Mazini, B. Mellado, W. Quayle, E. Richter Was, T. Takemoto, I. Vivarelli, S. L. Wu "Prospects for the search for a standard model Higgs boson in ATLAS using vector boson fusion", Eur. Phys. J. **C32S2**, 19 (2004).

[67] F. Maltoni and T. Stelzer, "MadEvent: automatic event generation with MadGraph", JHEP **0302**, 27 (2003).

[68] M.L. Mangano, M. Moretti, F. Piccinini, R. Pittau, A. Polosa, "ALPGEN, a generator for hard multiparton processes in hadronic collisions", JHEP **0307**, 001 (2003).

[69] Torbjorn Sjostrand, Leif Lonnblad, Stephen Mrenna, *PYTHIA 6.2: Physics and Manual*, arXiv:hep-ph/0108264 (2001).

[70] CMKIN Project Page, http://cmsdoc.cern.ch/cmsoo/projects/CMKIN (24/06/2007).

[71] http://cmsdoc.cern.ch/∼anikiten/cms–higgs/PTDR_SMxsect/SM_higgs_cross_sections.dat (20/06/2007).

[72] https://twiki.cern.ch/twiki/bin/view/CMS/OnSel_06_II_06 (20/06/2007).

[73] G. Davatz, M. Dittmar and A.-S. Giolo-Nicollerat, CMS AN-2005/026 (2005).

[74] E. Meschi, T. Monteiro, C. Seez CMS NOTE 2001/034 (2002).

[75] "CMS Data Acquisition and HLT TDR", CERN/LHCC 2002-26 (2002).

[76] W. Adam, B. Mangano, Th. Speer, T. Todorov CMS NOTE 2006/041 (2006).

[77] A.-S. Giolo-Nicollerat, "Electron reconstruction and electroweak processes as tools to achieve precision measurements at a hadron collider: from CDF to CMS", Ph.D. Thesis, CMS Thesis2005/010 (2005).

[78] I. Narsky, NIM **A450**, 444 (2000).

[79] "Significance", S_{cP}, S. Bityukov, http://cmsdoc.cern.ch/∼bityukov (07/06/2007).

[80] R. Wigmans, Nucl. Instr. and Meth. A **265**, 273 (1988).

[81] D.E. Groom, "What really goes on in a hadron calorimeter?", Proc. Seventh Inter. Conf. on Calorimetry in High Energy Physics, Tucson, Arizona, http://calor.pg.infn.it/calor1997/calorimg/friam/Groom.pdf (20/06/2007).

VITA

Efe Yazgan was born in Ankara on June 17, 1978. He received his B.S. and M.S. degrees in Physics from the Middle East Technical University in 2000 and 2002 respectively. He worked in the Physics Department of the Middle East Techical Univeristy from 2000 to 2007. He worked as a Guest Scientist at Fermi National Accelerator Laboratory, Batavia, Illinois, USA, from 2005 to 2007 and he will continue his research at CERN, Geneva as a Texas Tech University Research Associate. His main interests are experimental and phenomenological high energy physics and astrophysics. Below is his current publication list:

1. E. Yazgan *et al.*, "Search for a Standard Model Higgs Boson in CMS via Vector Boson Fusion in the $H \to WW \to l\nu l\nu$ Channel", CMS-AN Note 2006/091, CMS-NOTE 2007/011, hep-ex/0706.1898, Fermilab PUB-07-319-E.

2. G. Baiatian *et al.*, "Design, Performance and Calibration of the CMS Forward Calorimeter Wedges", CERN-CMS-NOTE-2006-044.

3. A. Ankay, S. Sahin, G. Karanfil and E. Yazgan, "Early Phases of Different Types of Isolated Neutron Star", International Journal of Modern Physics

D 14, 1075 (2005).

4. E. Tasci, E. Yazgan, O.B. Malcioglu and S. Erkoc, "Stability of Carbon Nanotori under Heat Treatment: Molecular-dynamics simulations", Fullerenes Nanotubes and Carbon Nanostructures, **13 (2)**, 147 (2005).

5. E. Yazgan and S. Erkoc, "Structural and Electronic Properties of (Cn Li)+ Cluster Ions", International Journal of Modern Physics C [Computational Physics and Physical Computation] 16, 271 (2005).

6. E. Yazgan, E. Tasci and S. Erkoc, "An algorithm to generate toroidal and helical cage structures using pentagons, hexagons and heptagons", International Journal of Modern Physics C, **15**, 267 (2004).

7. E. Yazgan, E. Tasci, O.B. Malcioglu and S. Erkoc, "Electronic properties of carbon nanotoroidal structures", Jour. Mol. Struc. (Theochem) **681**, 231 (2004).

8. O.H. Guseinov, O. Taskin, E. Yazgan, S. Tagieva, "Removal of the Difference between the Characteristic and the Real Age in the Magnetar Model from the Analysis of Spectral Properties of AXPs, SGRs and DRQNSs", International Journal of Modern Physics **D 12**, 1333 (2003)

9. O.H. Guseinov, E. Yazgan, S. Tagieva, S. Ozkan, "Pulsar Luminosity Function", Revisita Mexicana de Astronomia y Astrofisica, **39**, 1 (2003).

10. S.O. Tagieva, E. Yazgan and A. Ankay, "Do Young Neutron Stars which Show Themselves as AXPs and SGRs Accrete?", International Journal of Modern Physics D, **12**, 825 (2003).

11. O.H. Guseinov, E. Yazgan, S. Ozkan, A. Sezer, S.O and Tagieva, "Statistical Investigations of 1315 Radio Pulsars", Astronomical and Astrophysical Transactions **22**, 301 (2003).

12. O.H. Guseinov, E. Yazgan, A. Ankay, S.O. Tagieva, "On Period and Burst Histories of AXPs and SGRs and the Possible Evolution of these Objects on the P-Pdot Diagram", International Journal of Modern Physics D **12**, 1 (2003).

13. M.A. Alpar, A. Ankay, and E. Yazgan, "Pulsar Spin-down by a Fallback Disk and the P-Pdot Diagram", Astrophysical Journal Letters **557**, 61 (2001).

Chapters in Books:

1. E. Yazgan, O. Guseinov, A. Ankay, O. Taskin and S. Tagieva, "Analysis of Fall-Back Disk and Magnetar Models of Anomalous X-Ray Pulsars and Soft Gamma Repeaters" in Progress in Neutron Star Research NOVA Science, New York, ISBN:1-59454-351-8 (2005).

2. E. Yazgan, O. H. Guseinov, **et al.**, "Electron Distribution and Pulsar Distances in the Galaxy", in the book Pulsars:New Research, NOVA Science, New York, ISBN:1-59454-567-7 (2006).

Translation:

1. Y.U. Yazgan and E. Yazgan, "Can Science Explain Everything? Anything?" by S. Weinberg, Bilim ve Teknik (March 2005).

In preparation:

1. Optimization of energy reconstruction in CMS using Test Beam 2006 Data, CMS Hcal Collaboration

2. Supernova Remnants and Neutron Stars, eds. E. Yazgan, O. Guseinov, A. Ankay, NOVA Science, New York (at press).